

12-2016

Optical sub-diffraction limited focusing for confined heating and lithography

Luis M. Traverso
Purdue University

Follow this and additional works at: https://docs.lib.purdue.edu/open_access_dissertations

 Part of the [Mechanical Engineering Commons](#), and the [Nanoscience and Nanotechnology Commons](#)

Recommended Citation

Traverso, Luis M., "Optical sub-diffraction limited focusing for confined heating and lithography" (2016). *Open Access Dissertations*. 1019.
https://docs.lib.purdue.edu/open_access_dissertations/1019

This document has been made available through Purdue e-Pubs, a service of the Purdue University Libraries. Please contact epubs@purdue.edu for additional information.

**PURDUE UNIVERSITY
GRADUATE SCHOOL
Thesis/Dissertation Acceptance**

This is to certify that the thesis/dissertation prepared

By Luis M. Traverso

Entitled
Optical Sub-Diffraction Limited Focusing for Confined Heating and Lithography

For the degree of Doctor of Philosophy



Is approved by the final examining committee:

Xianfan Xu

Chair

Yi Xuan

Jong H. Choi



Liang Pan



Minghao Qi

To the best of my knowledge and as understood by the student in the Thesis/Dissertation Agreement, Publication Delay, and Certification Disclaimer (Graduate School Form 32), this thesis/dissertation adheres to the provisions of Purdue University's "Policy of Integrity in Research" and the use of copyright material.

Approved by Major Professor(s): Xianfan Xu

Approved by: Jay P. Gore

Head of the Departmental Graduate Program

10/10/2016

Date

OPTICAL SUB-DIFFRACTION LIMITED FOCUSING FOR CONFINED HEATING
AND LITHOGRAPHY

A Dissertation

Submitted to the Faculty

of

Purdue University

by

Luis M. Traverso

In Partial Fulfillment of the

Requirements for the Degree

of

Doctor of Philosophy

December 2016

Purdue University

West Lafayette, Indiana

*To Miguelángel, Natalia, and Alexis
For the joy that they bring to the family.*

TABLE OF CONTENT

	Page
LIST OF TABLES	v
LIST OF FIGURES	vi
ABSTRACT	ix
CHAPTER 1. INTRODUCTION	1
1.1 Optical Energy for Pattern Generation and Transfer	1
1.2 The Diffraction Limit of Light.....	2
1.3 Plasmonic Devices for Confinement of Light.....	3
1.4 Nanoscale Apertures	4
1.5 Study of Nanoscale Apertures for Practical Purposes	8
1.6 Fabrication of Fresnel Zone Plates for Confinement of Light	12
1.7 Thesis Outline	16
CHAPTER 2. LIGHT CONFINEMENT USING APERTURE ANTENNA	18
2.1 Applications of Near-Field Aperture Antennas	18
2.2 Fabrication of Bowtie Apertures.....	19
2.2.1 Focused Ion Beam Milling.....	21
2.2.2 Sacrificial Layer	23
2.2.3 E-beam Lithography.....	30
2.2.4 Transfer of Reverse Aperture Thin Membrane	37
2.3 Interferometric Spatial Phase Imaging for Gap Control	46
2.4 Parallel Nanolithography Using a Large Array of Bowtie Apertures.....	50
2.5 Summary	57
CHAPTER 3. ZONE PLATES FOR FABRICATION OF SILICON NANOWIRES ...	58
3.1 Definition of Zone Plate.....	58
3.2 Experimental Setup for Nanowire Fabrication	59
3.3 Designing a Zone Plate	62
3.4 Fabricating a Zone Plate	63
3.5 Thermal Decomposition of Silane	66
3.6 Thermal Simulation of Heated Substrate Using ZP for Nanowire Growth	67
3.7 Fabrication of Nanowires Using ZPs	70
3.8 Summary	72

	Page
CHAPTER 4. THERMAL CALCULATIONS FOR NEAR FIELD FOCUSING	73
4.1 Electromagnetic Model	73
4.2 Thermal Models	76
4.2.1 Construction of Thermal Models	76
4.2.2 Results and Analysis	81
4.3 Summary	86
CHAPTER 5. SUB-DIFFRACTION LIGHT FOCUSING USING A CROSS SECTIONAL RIDGE WAVEGUIDE NANOSCALE APERTURE	87
5.1 Layer-by-Layer Fabrication of Ridge Apertures	87
5.2 Electromagnetic Simulations	94
5.3 NSOM Characterization	97
5.4 Summary	101
CHAPTER 6. CONCLUSIONS AND RECOMMENDATIONS	102
6.1 Conclusions	102
6.2 Recommendations	102
6.2.1 Improving Thin Membrane Transfer	103
6.2.2 Thin Membrane Island	105
6.2.3 Improving the Sacrificial Layer Method	107
6.2.4 Two-photon Absorption Lithography	107
LIST OF REFERENCES	109
VITA	114

LIST OF TABLES

Table	Page
Table 2-1: Process for preparing the island substrate for thin membrane transfer.	39
Table 2-2: Process for preparing thin membrane wafer for transfer.	42
Table 2-3: Approaching and attaching the membrane.	44
Table 2-4: Steps of mask fabrication process.	51
Table 4-1: Optical properties used in the electromagnetic model.	74
Table 4-2: Thermal properties for materials used in the thermal models.	78
Table 4-3: Energy conservation calculations for verification of the thermal models.	86
Table 5-1: Process flow for the layer-by-layer fabrication of ridge apertures.	89
Table 5-2: Process flow for the characterization of the layer-by-layer ridge aperture. ...	90

LIST OF FIGURES

Figure	Page
Figure 1.1: Examples of nano-scale apertures in the literature.....	6
Figure 1.2: Electric intensity fields for perfect conductor ridge aperture models.	8
Figure 1.3: Designs for gap control of apertures.	10
Figure 1.4: Direct Metal Milling vs Through-the-Membrane Milling fabrication.	11
Figure 1.5: ZP used as an optical tweezers for beads in water.	13
Figure 1.6: Process flow to fabricate immersion ZP for array lithography.	14
Figure 1.7: Array of ZPs used for nanolithography.	15
Figure 2.1: Schematic & SEM images of real bowtie apertures with rounded edges.	20
Figure 2.2: Ideal sharp VS real curved edge bowtie aperture.	21
Figure 2.3: Schematic showing the use of a sacrificial layer.	23
Figure 2.4: Using 140 nm of PECVD silicon nitride as sacrificial layer.	25
Figure 2.5: Using 270 nm of PECVD silicon nitride as sacrificial layer.	26
Figure 2.6: Array of bowties using 200 nm of gold sacrificial layer.	27
Figure 2.7: Bowties using sacrificial layer of 120 nm of Cr on top of Au layer.	28
Figure 2.8: Bowties using sacrificial layer of Si on top of Cr layer.	29
Figure 2.9: HSQ aperture array exposed with $750 \mu\text{C}/\text{cm}^2$ dose on the region outside the aperture.	31
Figure 2.10: HSQ aperture array exposed with $650 \mu\text{C}/\text{cm}^2$ dose on the region outside the aperture.	32
Figure 2.11: Bowtie patterning using HSQ XR-1542 photo resist and no prebake to minimize thermally induced cross-linking.	33
Figure 2.12: Bowtie antennas after lift-off of gold metal on PMMA.	34

Figure	Page
Figure 2.13: Apertures exposing PMMA on the region outside the aperture.	35
Figure 2.14: Bowtie aperture made after exposing HSQ inside the bowtie area and then making a gold lift-off with BOE.	36
Figure 2.15: Dose test milling bowtie apertures on Au through a silicon nitride membrane.	38
Figure 2.16: Attaching a membrane using platinum deposition.	45
Figure 2.17: Gratings used for ISPI gap measurement.	47
Figure 2.18: ISPI gratings in a lithography mask.	48
Figure 2.19: Simulations and measurements of ISPI phase and frequency as function of the gap.	50
Figure 2.20: Diagram of the bowtie aperture lithography station.	55
Figure 2.21: Using ISPI for gap control and results of nano-scale lithography.	56
Figure 3.1: Setup up for ZP assisted silicon nanowire growth.	61
Figure 3.2: Optical path of zones inside a ZP.	62
Figure 3.3: Images of fabricated ZPs.	66
Figure 3.4: Heat transfer simulation of nanowire growth substrate under the influence of ZP generated focused hot spots.	69
Figure 3.5: Time history of the maximum temperature node at the surface of the substrate.	70
Figure 3.6: Effect of power and polarization in the formation of nanowires.	71
Figure 4.1: Stack of materials used for the electromagnetic simulation and outline of the dimensions of a bowtie.	75
Figure 4.2: View of the large reservoirs for an aperture and recording medium models and zoom in of the bowtie aperture and recording medium regions.	78
Figure 4.3: Models of bowtie aperture and recording medium showing walls of symmetry used to diminish the number of elements and nodes in the calculations.	79
Figure 4.4: Heat generation profile presented in W/m^3 on a logarithmic scale for a) the bowtie aperture and b) the recording medium.	81

Figure	Page
Figure 4.5: Temperature vs. time solutions for a silver aperture with and without the influence of the of the HAMR recording medium.	82
Figure 4.6: Temperature vs. time solutions for a gold aperture with and without the influence of the of the HAMR recording medium.	83
Figure 4.7: Temperature vs. time solutions for a recording medium maximum temperature using silver and gold apertures.	83
Figure 4.8: Heat generation and resulting temperature profile for aperture and recording medium.	85
Figure 5.1: Schematic of the final ridge aperture.	89
Figure 5.2: SEM images of the ridge aperture structure during intermediate steps.	93
Figure 5.3: EM simulation model and field distribution for the ridge aperture.	95
Figure 5.4: Field distribution of an aperture with 3 different penetration depths.	96
Figure 5.5: Field distribution of an aperture with 3 different widths.	97
Figure 5.6: Far-field image of apertures and schematic of s-NSOM.	98
Figure 5.7: Experimental characterization of the apertures without localized spots.	99
Figure 5.8: Experimental characterization of the apertures with localized spot.	100
Figure 6.1: Using an HSQ adhesion layer as a variation for thin membrane transfer. ..	105
Figure 6.2: Fabricating an island on a thin membrane wafer.	106

ABSTRACT

Traverso, Luis M. Ph.D., Purdue University, December 2016. Optical Sub-Diffraction Limited Focusing for Confined Heating and Lithography. Major Professor: Xianfan Xu, School of Mechanical Engineering.

Electronics and nanotechnology is constantly demanding a decrease in size of fabricated nanoscale features. This decrease in size has become much more difficult recently due to the limited resolution of optical systems that are fundamental to many nanofabrication methods. A lot of effort has been made to fabricate devices smaller than the diffraction limit of light. Creating devices that are capable of confining fields by means of interference patterns of propagating wave modes and surface plasmon, has proven successful to confine light into smaller spot sizes.

Zone plate diffraction lenses generate spots with dimensions very close to the diffraction limit. We report the fabrication of zone plates to be used in laser direct writing of silicon nanowires. We show experimentally and with numerical models that a silicon substrate subjected to a focused spot is capable of reaching the necessary temperature for the synthesis of silicon nanowires with widths of 60 nm, which is considerably smaller than the diffraction limit of the processing laser.

Nanoscale ridge apertures are devices with a great potential to confine light energy. Such apertures have been experimentally proven to create very small lithography features. We believe that these apertures can be further modified in order to achieve a practical smaller confinement in the near field region. In this thesis we discuss several attempts to design and fabricate apertures with sharp edges and implement them in a previously reported parallel lithography setup. In an attempt to use apertures for parallel fabrication of patterns, we developed a system to control the position of the near-field region with

respect to a lithography substrate. To do this we use a method of interferometric-spatial-phase-imaging (ISPI). With the implementation of this method we were able to produce an array of 32X32 lines with confined widths as small as 22 nm. Nanoscale ridge apertures were also studied to be used as near field transducers for heat-assisted magnetic recording. They have the capability of transmitting and confining enough energy to increase the temperature of a recording medium without reaching detrimental temperatures themselves. Numerical methods are presented to prove theoretically that a well-designed aperture performs well as a near field transducer. The size of the spot region focused by the aperture could allow us to record data with higher area density than current conventional methods.

CHAPTER 1. INTRODUCTION

Pattern generation and transfer lie at the core of nanotechnology fabrication and data recording. Numerous fabrication methods have been designed in nanotechnology in order to keep decreasing the size of the patterns to be generated and transferred. Decreasing the size is very important because it allows creating more compact technology, faster and more powerful integrated circuits, and denser memory devices. Decreasing pattern size is relevant not only when fabricating new devices but also when recording data into a medium. Optical energy has been one of the most widely used tools to generate patterns because of its ability to change material properties in relatively small volumes. For this reason it has always been of interest to focus light into smaller spots. This thesis is mainly about finding methods for fabricating devices that can efficiently achieve light confinement and thus can be used in further pattern generation processes involving heating and lithography.

1.1 Optical Energy for Pattern Generation and Transfer

Pattern generation or transfer can be seen as the writing of geometrical patterns into a layer. Light can be used in different ways such as exposing a photosensitive material or by heating a material that can absorb it. Patterns can be generated or transferred by selectively exposing parts of a material to a light source. Their generation can be achieved by scanning a focused beam or selectively flashing light regions over a material using a computer aided design or a mathematical transformation of it as a guide. Alternatively, an already generated pattern can be transferred by using it as a mask positioned between a light source and a photosensitive material. The main drawback for optically based pattern generation and transfer is that it is diffraction limited and hence is impossible to propagate spot sizes smaller than a fraction of the wavelength.

1.2 The Diffraction Limit of Light

It is very well known that due to its wave behavior, light is subjected to the diffraction limit. When considering a small propagating field we have to take into consideration that there are constructive and destructive interference that do not allow for the spot to be resolved in the far field. The diffraction limit of light can be mathematically described as:

$$\Delta x \geq \kappa \frac{\lambda}{NA} \quad (1.1)$$

Where Δx is the smallest spot size that can propagate into the far field, κ describes the optical system, λ is the wavelength of the incident light and NA is the numerical aperture of the lens and optical system.

This does not mean that electromagnetic fields or their effect on matter can't be confined in smaller distances than Δx . Even when light cannot propagate in such small spots, it can still interact with features that are smaller than the diffraction limit. When light interacts with these features, they respond by creating "near field" variations around them that have similar dimensions. An enhancement or a suppression of the incident field can occur in the near field by means of interference of evanescent waves or resonance of plasmon polaritons. We can consider an enhanced near field around a nanoscale feature to be a confinement of a field, which under the right circumstances can easily be smaller than the diffraction limit.

Since light can be manipulated to chemically modify matter in specific patterns, another way of confinement can be mentioned when considering the volume of a chemical altering interaction with the material. We shouldn't only think how small an electromagnetic field volume could be but also how small is the volume of the material that we intend to alter. For several processes involving light material interaction there might be a certain parameter threshold for which there is not a permanent alteration of the material. We can say that the confinement for a certain process lies within the volume in which the field surpasses such threshold. Several thresholds can be mentioned. The solubility of a given photoresist zone submerged in a certain developer depends on an

energy threshold. The delivered energy depends on the intensity of an incident electric field and the time of the field exposure upon the material. By controlling both the intensity and time of exposure we can control the volume that will be developed. For a nonlinear process like two photon absorption lithography, the intensity threshold is very significant. If the intensity is not high enough there won't be two-photon absorption, even when you allow enough time to deliver as much energy as possible. A process like the silicon nanowire growth using zone plates (described in more detailed in chapter 3), has a threshold of temperature necessary for silane decomposition to happen. By controlling the intensity and other parameters that influence the temperature rise of a gas, we can control the volume of the created nanowire. Related to all of these mentioned thresholds there is a volume of material interaction that can be further confined by changing certain parameters related to the delivered power, the time of energy delivery and the capability of the material to absorb this energy for a given process. This is important because the diffraction limit is not a limit anymore. Even for propagating small spots that are very close to the diffraction limit, we can create certain effects within smaller dimensions. Further in this thesis we will discuss the previously mentioned use of zone plates with which we can create far field propagation of spots with sizes close to the diffraction limit and then be used to fabricate sub-diffraction features due to a confined material interaction.

1.3 Plasmonic Devices for Confinement of Light

Recently, the use of the surface plasmon polaritons (SPPs) is one of the most studied ways of overcoming the diffraction limit (Maier, 2007, Hayasi and Okamoto, 2012). The collective oscillations of electrons at the boundary of a metal and a dielectric called surface plasmons can be generated with an incident wave on such a boundary. While oscillating at the same frequencies as the incident wave, plasmonic waves can have much shorter wavelengths. This provides a great means to concentrate electromagnetic energy to dimensions that are much smaller than the diffraction limit of light. Plasmonic devices are nanoscale structures with dimension comparable to the wavelength of the plasmonic oscillations. There have been studies on plasmonic devices for light focusing

with different types of geometries including 1 -dimensional boundaries between 2 dimensional metal-dielectric crystals (Mason et al., 2014), nanoparticles, slits, rods, wedges, rings, V-shaped grooves (Zhang and Zhang, 2012), and nano-diabolo (Kim et al., 2015), among others. Light focusing plasmonic devices have been widely used for many different applications including near-field scanning optical microscopy NSOM (Wang et al., 2015, Bharadwaj et al., 2009), photovoltaics, light emission (Bharadwaj et al., 2009), and nano-lithography (Xie et al., 2011).

One of the most promising applications for plasmonic devices that has been investigated recently is the development of plasmonic near field transducers (NFT) (Zhou et al., 2014) for Heat Assisted Magnetic Recording (HAMR)(Kryder et al., 2008). Because of the inherent magnetic instability of small volumes when the bit size of a recording media reduces (Sharrock, 1990), conventional magnetic recording has reached the limit of miniaturization of about $1\text{TB}/\text{in}^2$. For HAMR, media with higher stability is used, and an NFT creates a very localized intense electromagnetic field that heats up the medium and thus decreases its coercivity. Among previously reported NFTs, there were structures with different shapes including lollipops (Challener et al., 2009), E-shape structures (Stipe et al., 2010), bowtie apertures (Zhou et al., 2016), and nano beaks (Matsumoto et al., 2008). A special family of nanoscale confinement devices is the antennas and apertures, which we review in the next section.

1.4 Nanoscale Apertures

Nanoscale apertures can be considered as antennas that can couple energy between an incident far field into a localized near field and vice versa. Apertures usually are placed in thin films that without their presence would be optically opaque. It is very interesting to observe that even when these apertures are smaller than the diffraction limit, there are certain designs in which they can achieve outstanding transmission. Using a classical electromagnetic framework by means of the Maxwell equations, it has been calculated that the power transmission for a single circular aperture decays as the 4th power of its diameter decreases (Bethe, 1944, Leviatan, 1986). Because of this effect of

the diffraction limit, the problem of field confinement for a single aperture goes hand in hand with the problem of maximizing transmitted power through an aperture.

There are several different explanations for the mechanism of transmission. An array of holes shown in Figure 1.1 can show an exceptional transmission, which is claimed to happen due to the resonant excitation of surface plasmons (Ghaemi et al., 1998). Later it was observed experimentally that similar behavior could happen in films that do not support plasmon propagation (Lezec and Thio, 2004). In their paper they proposed that the enhanced transmission is due to a composite diffracted evanescent wave. Even when these experiments give us an insight of the enhancement and transmission of the field, there is no measurement of the near field of the apertures so their confinement properties are not very clear. In order to discuss their potential focusing capability, it is better to look at studies of single apertures.

Triple tapered apertures like the one shown in Figure 1.1(b) have shown to increase throughput over 10^3 times (Yatsui et al., 1998). This enhancement is attributed to a reduction of a propagation loss and an effective excitation of an HE_{11} mode.

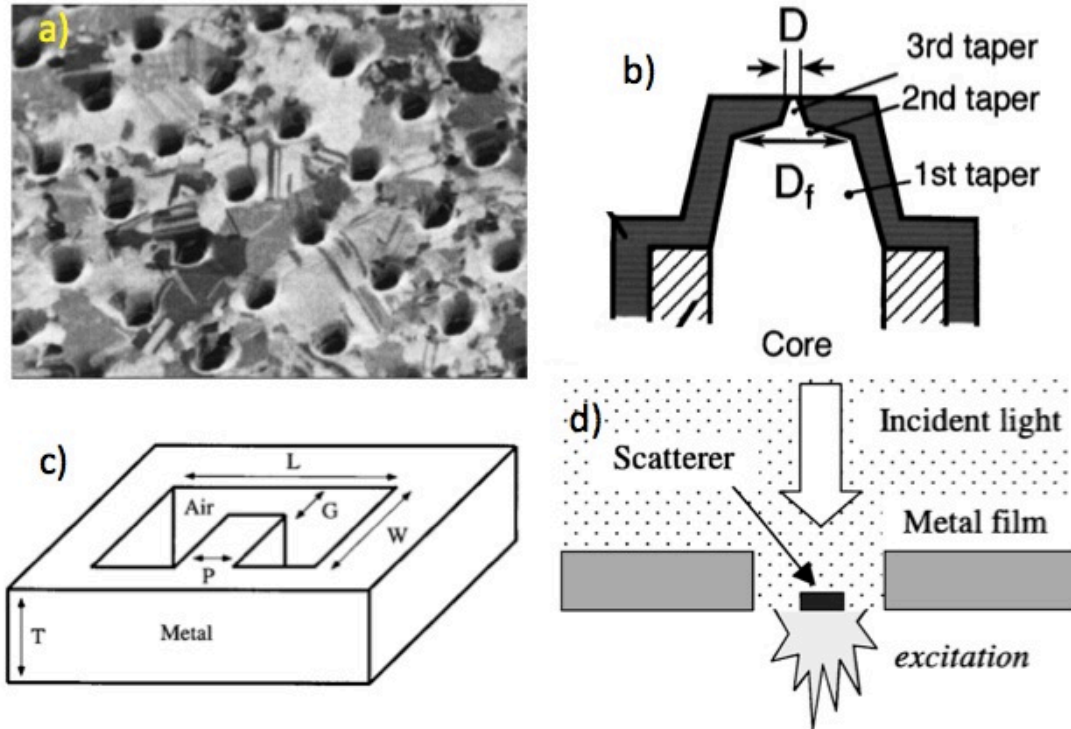


Figure 1.1: Examples of nano-scale apertures in the literature. a) Array of holes that showed resonant excitation (Reprinted with permission from [Ghaemi et al., 1998] © (1998) APS). b) Triple tapered aperture (Reprinted from [Yatsui et al., 1998] with the permission of AIP publishing). c) Model for the perfect conductor C aperture studied by Seagate Technology (Reprinted from [Sendur et al., 2004] with the permission of AIP publishing). d) Square aperture with the minute scatterer presented by Tanaka et al., (2001).

It has been shown by using numerical Finite Difference Time Domain (FDTD) simulation, that a C aperture has a power throughput 1000 times more than a square aperture with 100 nm side that would produce the same spot size (Shi & Hesselink, 2002). Finding this throughput requires identifying the best propagation mode, which is TE_{10} mode and optimizing to find a resonant thickness. This study is made under the assumption that the aperture metal is a perfect conductor, which does not allow for surface plasma resonance behavior. Another C aperture shown in Figure 1.1(c) has been studied at Seagate Technology (Şendur et al., 2004). Şendur et al. calculated that the power dissipation in the recording medium is greatly enhanced when choosing waveguide dimensions, materials, and incident wavelength that will allow a certain excitation of surface plasmon resonance. A scatterer element like the one shown in

Figure 1.1(d) has been calculated (Tanaka et al., 2001) to increase the surface plasmon excitation. This scatterer element is a volume of 80 nm X 80 nm with a thickness of 30 nm, which lies inside of a 200 nm X 200 nm aperture of 100 nm thickness. The calculations were made with the aperture positioned in top of a recorded medium and without the recorded medium. The presence of a recorded medium allowed (for a certain polarization) a coupling that would increase the transmitted energy and would decrease the size of the spot. It was also presented in this study that there was more transmitted energy for silver scatterer, which had the highest relationship of $|\epsilon'|\epsilon''$ where ϵ' and ϵ'' are the real and complex coefficients of the complex dielectric constant $\epsilon = \epsilon' + i\epsilon''$. An aperture with an I shape was modeled by solving the volume integral equation using Lippman-Schwinger equation of quantum physics (Tanaka & Tanaka, 2003). They also use a complex permittivity and establish that surface plasmon polaritons propagate through the sidewalls of the aperture creating a maximum intensity that is 4 times the intensity of the incident field. A thorough study on H ridge aperture and a comparison study of H, C, and bowtie aperture was made by Jin & Xu (2004). For the H aperture it is discussed that even for a perfect conductor the transmission efficiency of the case in which the incident light is polarized across the ridge is 2,800 times the efficiency when the light is polarized parallel to the walls that confine the gap. For all of these perfect conductor models a waveguide behavior reveals that there is a cutoff frequency for which, when the wavelength of the incident light is longer than the cutoff it will only propagate a faint evanescent wave but when is slightly shorter than the cutoff there will be a TE_{10} mode that concentrates light inside the gap. When the incident wavelength of the light is much shorter than the cut-off, there might be a 2nd propagating mode TE_{20} that will generate 2 spots on the open areas of the H aperture. This is unwanted because these two spots will decrease the resolution of the aperture focusing. Propagation modes and maximum intensities for these cases are shown in Figure 1.2. Polarization of all shown models is constant across the ridge. It is established in this paper that when using a real metal with complex permittivity there is an excitation around edges of the metal that decreases the localization of the spot, which is unwanted.

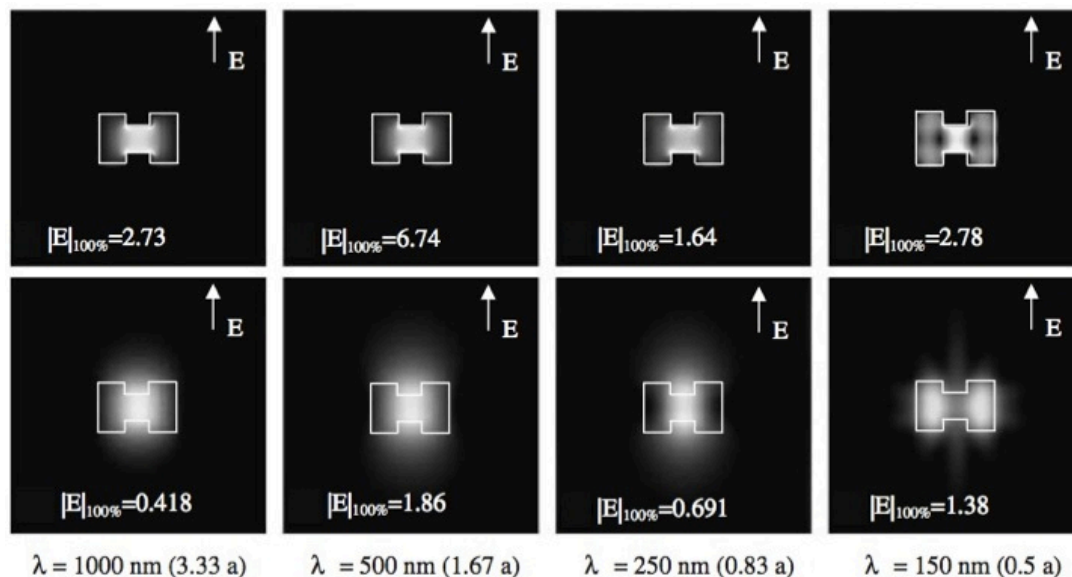


Figure 1.2: Electric intensity fields for perfect conductor ridge aperture models. The 1st row shows the field at the middle of a film and 2nd shows it at 50 nm behind the aperture. Each column represents a different wavelength. Each maximum field number is normalized to an incident field of 1 (Jin and Xu, 2004).

1.5 Study of Nanoscale Apertures for Practical Purposes

Confinement of optical energy has already been demonstrated to be useful for practical purposes. The fabrication of an efficient ridge aperture suited for these purposes has posed a set of problems common to all of the previous researchers that have taken upon this task. Control of the aperture geometry defines a control of the dimensions of the confined spot. Sharpness of the structure could define confinement together with enhancement. Control of the gap between the aperture and the substrate is important because most of the useful confined energy is within the near field. Here we review past attempts of fabricating aperture devices useful for different applications.

Plasmonic devices have been proven experimentally to have a lot of potentials for nanolithography (Xie et al., 2011). A bowtie aperture array was milled using Focused Ion Beam (FIB) on top of a set of islands that would be approached to a substrate coated with photo resist (Uppuluri et al., 2010). To obtain a consistent gap through out the array of apertures, Uppuluri designed an interferometer device that would control the parallelism between two surfaces. Even though good parallelism could be obtained, there

was not a direct measurement of the gap between the island surface and the photo resist. The approach between the two surfaces would be made in a “blind” manner until an image showing interference fringes would indicate that there was indeed contact. Bowtie apertures using FIB have been fabricated on top of flexible holders (Kim et al., 2009). These holders (Figure 1.3(a)) are meant to mechanically press an aperture against a coated substrate and create a uniform and constant gap during a scanning process. They cut a half ball lens into a conical shape in order to create a Solid Immersion Lens (SIL) with a 3 μ m diameter contact area region and then they polished it using low energy FIB to have a root-mean-square roughness of approximately 1 nm. At the tip of the cone they coated a layer of 120 nm of Al on top of which they milled bowtie apertures with FIB. They coated a good quality PECVD oxide layer of 300 nm that was milled down to 10 nm using FIB. In order to reduce friction they coated a Self Assembled monolayer of 1H, 1H, 2H, 2H-perfluorooctyltrichlorosilane which makes the difference between having 10 nm scratches or not. The whole SIL-aperture arrangement was mounted in a sheet metal spring that was positioned below an objective lens. For this experiment they focused on to the apertures a 405 nm wavelength laser into a spot of approximately 340 nm. Patterning speed was as high as 10 mm/s for which they obtained lines of 50 nm Full Width Half Maximum. In order to control the gap between a plasmonic aperture and a coated photo resist substrate, Srituravanich et al., (2008) designed an aerodynamic air bearing system for a flying head above a rotating substrate.

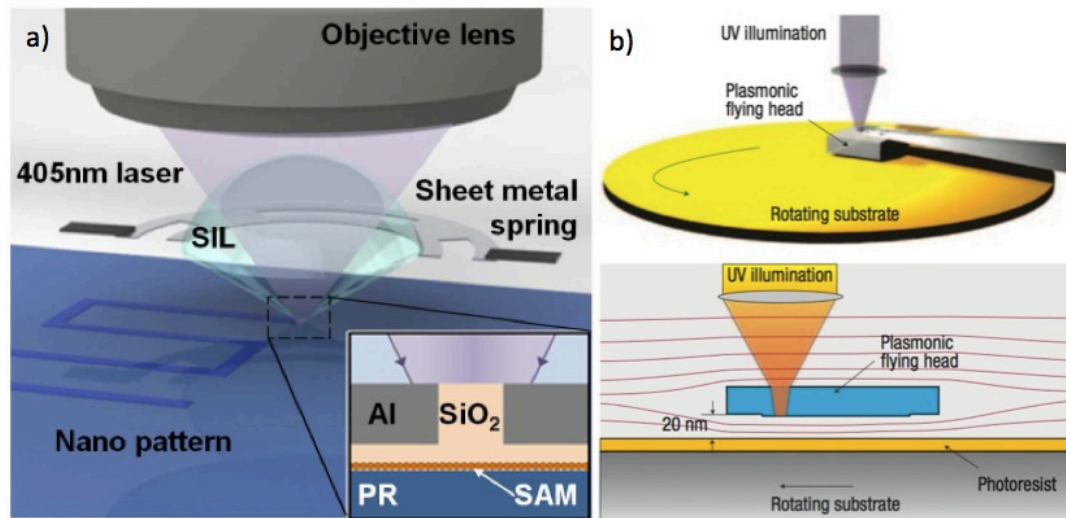


Figure 1.3: Designs for gap control of apertures. a) Device with flexible mount (Kim et al., 2009) and b) flying plasmonic head in with plasmonic apertures. Reprinted by permission from Macmillan Publishers Ltd: [Letters] (Srituravanich et al., 2008) © 2008.

The rotating substrate like the one shown on Figure 1.3(b) would create an airflow which would generate a lift force on the head that according to simulations would maintain a height of ~ 20 nm for a range of speeds of 4 to 12 m/s. There would be an array of 4X4 plasmonic lenses consisting each of an aperture surrounded by rings. At a linear speed of 10 m/s they were able to obtain an 80 nm line width. Later a different plasmonic lens in the flying head (Pan et al., 2010) was designed for the same system for which they were able to obtain lines of 50 nm at the same speed.

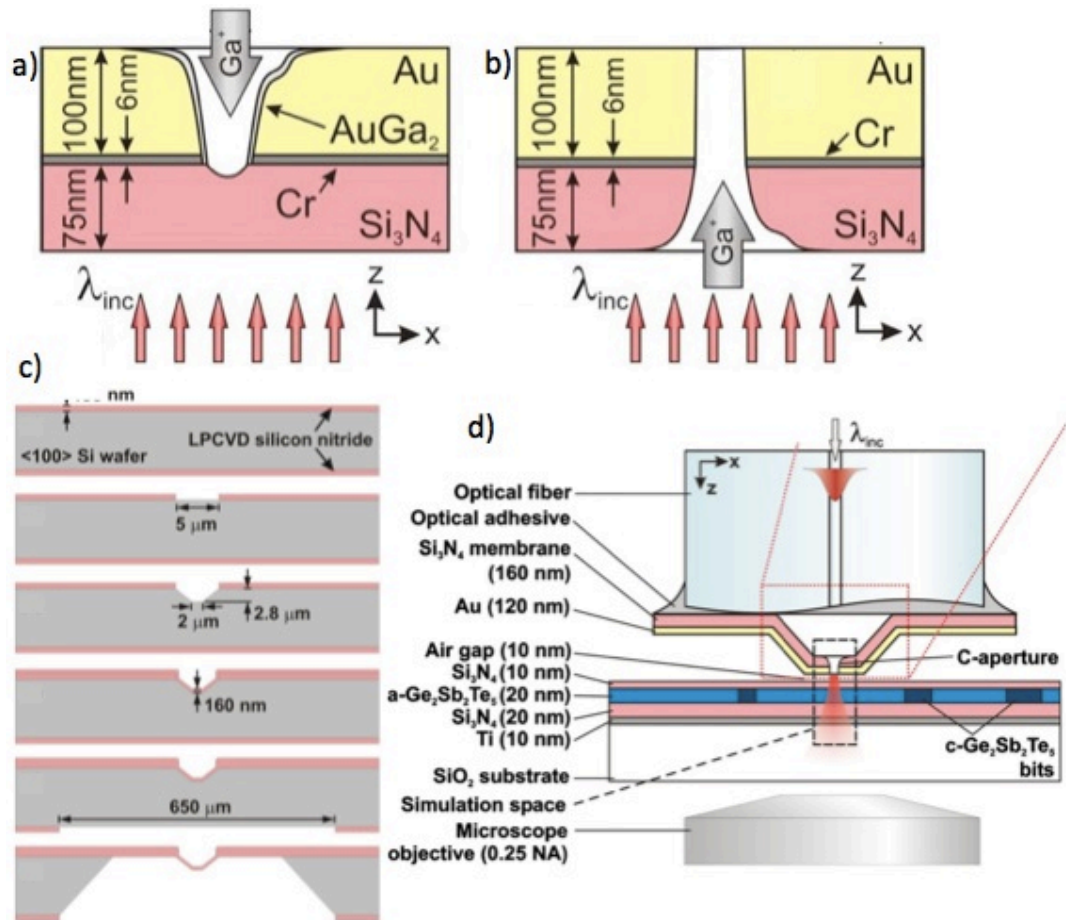


Figure 1.4: a) Direct Metal Milling (DMM) vs b) Through-the-Membrane Milling (TMM) fabrication (Leen et al., 2008). c) Fabrication procedure for the aperture island for the d) optical data C aperture NSOM; Reprinted from [Leen et al., 2010] with the permission of AIP Publishing.

All the previously mentioned apertures have been made with FIB milling. This method so far has provided the most flexible way of fabricating apertures with relatively well control gaps of the ridges. A problem with this method is that when we try to increase the resolution of the milling, there is an inherent round in edges of the aperture. This can lead to an effective ridge gap that is larger than the one intended. Sharper edges could provide better control of the gap and thus the confinement and enhancement of the output near field.

Reversing the milling direction through a membrane can result in a sharper edge as demonstrated by (Leen et al., 2008) and shown on Figure 1.4 (a) and (b). They mill a C type aperture through a 75 nm LPCVD silicon nitride membrane masking a 100 nm

gold layer. They call this kind of milling through-the-membrane milling (TMM) as opposed to direct metal milling (DMM). They reported that the spot size is 2.2 times smaller for the TMM than for the DMM and also 63 times more intense. The same group later reported the use of this idea for a setup shown in Figure 1.4 (d) for optical data heating storage with bits of $\lambda/20$ which could yield a density of 223 Gbit/in² (Leen et al., 2010).

All of these nanoscale apertures presented are capable of sub-diffraction limit focusing and thus field confinement. In this thesis we consider also the confinement of the material interaction volume for devices like zone plates that propagate field spots close to the limit but are not capable of sub-diffraction limit focusing. Next section we review the technology of zone plates and consider them for sub-diffraction confinement of the material interaction volume.

1.6 Fabrication of Fresnel Zone Plates for Confinement of Light

Fresnel Zone Plates (ZPs) can be seen as lens that has an effective high numerical aperture. They consist of a determined amount of diffractive focusing rings named zones and are capable of reducing the spot size when compared to regular lenses. Via Fresnel diffraction they are able to create a very tight confinement in their focal spot. By changing the grating period of their rings is possible change their focal distance. Since they are based on propagation optics, the dimensions of their focal spots are subjected to the diffraction limit.

The fabrication of ZPs is relatively easy compared to nanoscale ridge aperture whose smaller dimensions can be in the order of tens of nanometers. They have been fabricated in many different ways and for different reasons. A gold ZP lens was lifted-off after e-beam patterning and used as an optical tweezers for beads in water (Schonbrun et al., 2008). Figure 1.5 (a) shows a bead with diameter of 2 micron being trapped by the focal point of a ZP, which can also be seen in the picture.

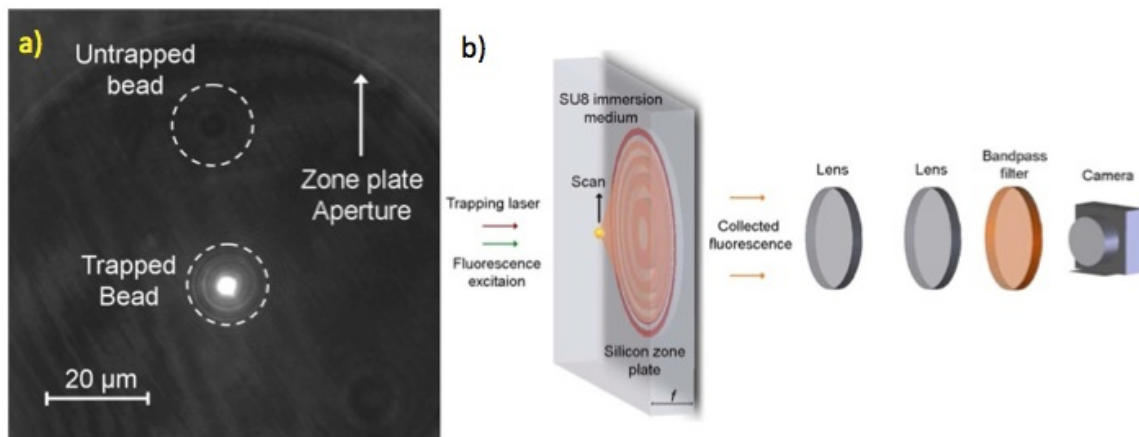


Figure 1.5: a) ZP used as an optical tweezers for beads in water on the left; Reprinted from [Schonbrun et al., 2008] with the permission of AIP Publishing. b) Scheme for using shot focal length ZP for scanning microscopy (Schonbrun et al., 2009).

A lens was etched (later by the same group) in silicon after an e-beam lithography patterning, immersed in a coating of SU8 medium (as shown in Figure 1.5(b)) and then used as short length lens that was capable of scanning fluorescent particles of 500 nanometers with a precision of ± 38 nm (Schonbrun et al., 2009).

An advantage of ZPs is that they occupy a relatively small area, which makes it possible to place an array of them in a vicinity. An array of zone plate was fabricated in order to be used for lithography (Chao et al., 2005). As shown in Figure 1.6 on the left side, these ZPs were etched in silicon dioxide using nickel and silicon nitride as an etch mask. The nickel mask was patterned using a lifted off PMMA patterned with e-beam lithography. In order to use them for array lithography they had to be isolated by coating the whole surface with chrome and then performing a process named Fulton-Dolan process (Fulton & Dolan, 1983), in which the electrical isolation of features due to the zones allows them to etch selectively the chrome deposited inside the ZP. This isolation is very useful also to avoid background light. There were modulated beams incident on each of the ZP to aid the array lithography process. The fabricated zone plates had a numerical aperture of $NA = 0.85$, which after immersion in water increase to $NA = 1.14$. For an incident wavelength of 400 nm they were able to obtain lines with periods of 115 nm half period. Later the same array was fabricated using patterning with the nano-imprint lithography process shown in the right of Figure 1.6 (Galus et al., 2006).

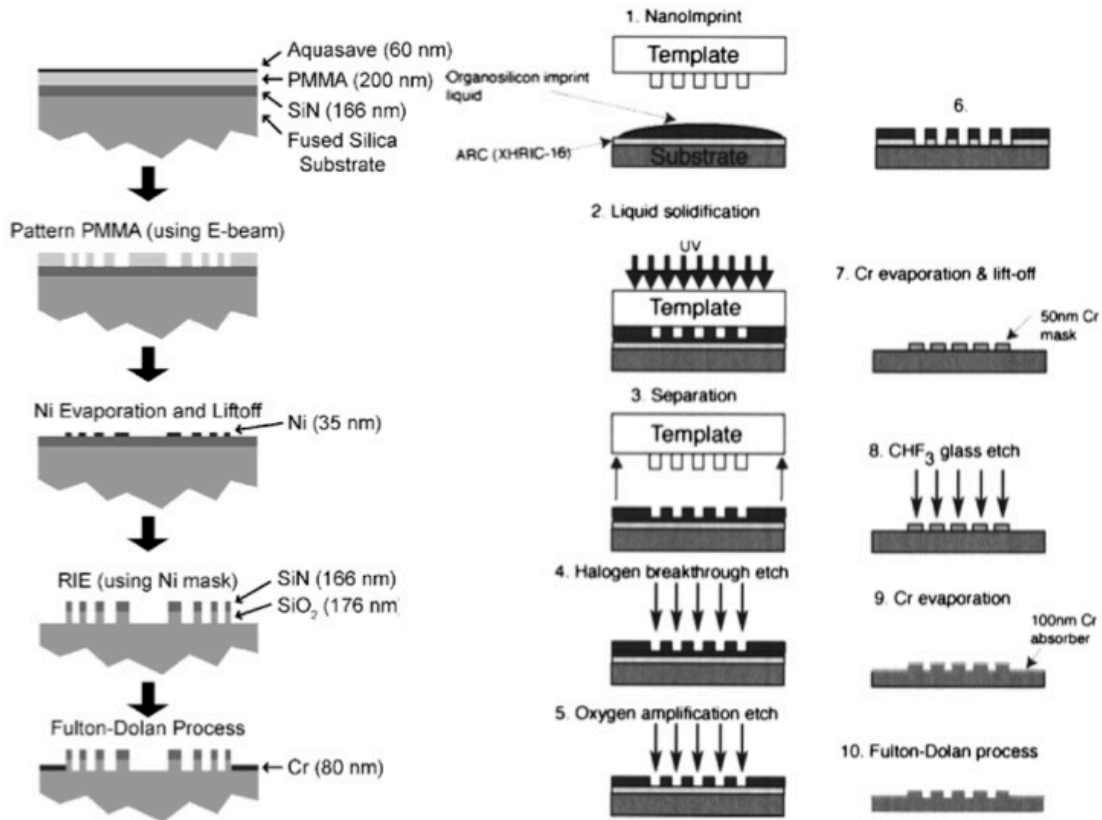


Figure 1.6: Process flow to fabricate immersion ZP for array lithography on the left; Reprinted with permission from [Chao et al., 2005] © [2005] American Vacuum Society. The fabrication of a similar ZP for array made with photo curable nano-imprint lithography on the right; Reprinted with permission from [Galus et al., 2006] © [2006] American Vacuum Society.

The array lithography setup similar to the aperture array has a very clear advantage for parallel processing. If independent beam were to be shined to each focusing device, the combinations for large patterns could increase dramatically. Figure 1.7 (a) shows a diagram of a parallel processing lithography using ZPs presented by Chao (2005). After several reports on this same system, the research group presented the ZP array lithography as a low cost complement or competitor for e-beam lithography (Smith et al., 2006). Figure 1.7(b) shows results for lithography that have dimensions very close to the diffraction limit, which shows excellent confinement. There is one additional advantage of having such a small spot. A confinement that is smaller than the diffraction limit can be achieved. We can use spots to create lithographic or heating effects in materials that are actually much smaller than the diffraction limit. Figure 1.7 (b) shows a

theoretical simulation in which lithography achieves periodic structures of 20 nm lines by means of nonlinear recording. By taking advantage on nonlinear effects such as 2 photon absorption, the size of the lithography results could decrease significantly much lower to the diffraction limit.

We discuss a similar idea in a future chapter. In order to achieve this extra confinement we need to make sure that their efficiencies are high enough to create an intense field in the focal spot.

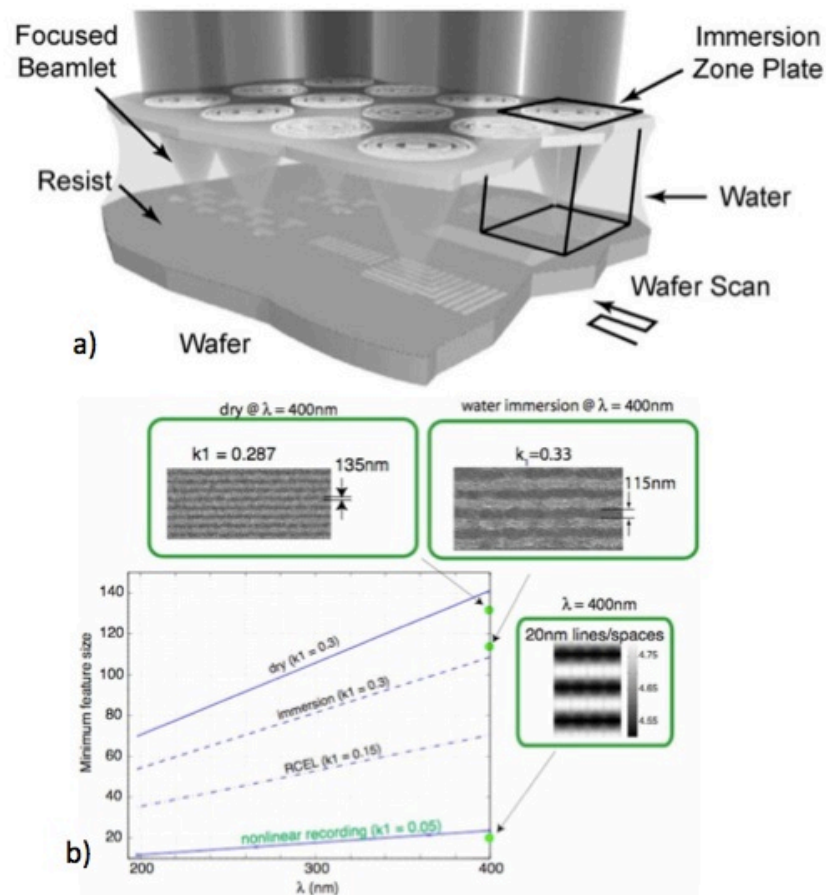


Figure 1.7: a) Array of ZPs used for nanolithography Reprinted with permission from [Chao et al., 2005] © [2005] American Vacuum Society. b) Result and simulations for lithography using ZP array; Reprinted from (Smith et al., 2006) with permission from Elsevier.

1.7 Thesis Outline

This work presents a practical experimental frame for design, fabrication, and testing of sub diffraction focusing devices that also includes a heat transfer analysis to study how doable is to use some of the discussed devices.

Chapter 2 presents work related to near field confinement using optical antenna. It presents a discussion on some applications as well as several attempts to improve the quality of the near field spot generated by the aperture. It goes into more details in Interferometric Spatial Phase Imaging (ISPI) used to control the position of a substrate with respect of the near field of the aperture. Then it discusses how this ISPI together with an interference alignment method has been used to obtain gap control for array aperture lithography.

Chapter 3 presents work related to the fabrication of Zone Plates using the e-beam resist hydrogen silsesquioxane (HSQ). A study of the thickness control to improve efficiency of the lens is presented together with a study on how to improve the adhesion of the HSQ coated on top of a transparent conducting layer of indium tin oxide. A numerical simulation for the thermal profile of a focused beam in a substrate gives us information of how likely these ZPs are used for silicon nanowire thermal growth.

Chapter 4 presents an attempt to create a relationship between electromagnetic fields and thermal profile for bowtie ridge aperture. Results of numerical models for electromagnetic distribution are taken and converted into volumetric heat generation input for thermal models in Ansys. Then the temperature rise of a heated substrate is compared to establish an efficiency of a near field transducer for Heated Assisted Magnetic Recording.

Chapter 5 discusses the development of a new type of ridge aperture based on a layer-by-layer planar lithography. The aperture fabrication flow leading to a final product is presented. A finite element method numerical model is constructed and solved to obtain the electric field distribution of several apertures with different dimensions. Results are compared with experimental measurements made with scattering near field optical microscope at the exit of an aperture.

Chapter 6 concludes the thesis and shows recommendations for future work related to the projects worked on the previous chapters. These recommendations are for improving the methods for thin membrane transfer and sacrificial layer aperture sharpening. Also suggestions regarding the use of 2-photon absorption are presented.

CHAPTER 2. LIGHT CONFINEMENT USING APERTURE ANTENNA

Optical antennas are structures with the potential to focus an incident EM field into spots smaller than a fraction of the wavelength of the field. They are capable of confining the light and enhance the intensity of the incoming field (Jin & Xu, 2006). The effect of waveguides, evanescent waves or surface plasmons permits the propagation of an EM field from the entrance, through the aperture, to a spot at the exit of the apertures. The presence of localized surface plasmons can enhance this field. Antennas can be stand-alone metal features or apertures within a metal surface. Several different shapes of antennas have been studied in the past. Some of the most discussed simple shapes have been H shape (Jin & Xu, 2004), C shapes (Leen et al., 2008), and simple hole arrays (Ghaemi et al., 1998). The work presented in this document is mainly relevant to Bowtie shape aperture antennas.

2.1 Applications of Near-Field Aperture Antennas

The confined small spot generated by an aperture can be used for many applications. This spot light can be absorbed by a material and converted into heat or change its chemical properties. The use of apertures has already been considered greatly for applications involving recording, lithography or heating.

In the last few years Heat Assisted Magnetic Recording (HAMR) has been considered to increase the data density recording in magnetic materials (Kryder et al., 2008). The magnetic recorded medium is a collection of magnetically isolated grains. To obtain a higher recording density, these magnetic elements need to be smaller. As they become smaller they become magnetically unstable. HAMR pose a solution to this problem by allowing us to use a more stable media for which its coercivity can be change by changing its temperature. A localized small spot heating allows us to control the

recording of small magnetic elements. When the temperature of a grain is raised, it is easier to induce a change of its magnetization state. The threshold at which this occurs is called the Curie temperature. In HAMR a localized spot will heat the magnetic element above the Curie temperature and a large magnetic dipole will switch its magnetization state. Using a material with high coercivity at ambient temperature would ensure that there is no magnetization of unintended grains.

Aperture optical antennas have since long been proposed to confine optical energy on such localized spots on lossy metallic recording medium (Challener et al., 2006). They have studied coupling efficiency, spot size, and spot shape. Spot shape has been pointed to also be important to obtain correspondence with grain recording bits since they are not necessarily circular. Near field confinement using bowtie apertures for HAMR application have been studied by adding the whole media stack of recording substrate into EM models (Zhou et al., 2016). It was found earlier (Zhou et al., 2011), that the ratio of spot size could be controlled by changing the sizes of the bow tie aperture gap region. This allows us to design particular apertures for different magnetic elements.

A localized spot of an aperture antenna can be used for optical lithography to produce patterns of subwavelength size. Different spot sizes have been compared for different types of aperture in the same lithography step (Wang et al., 2006). Antennas have also been positioned in NSOM tips in order to create scanned lithography lines of 60 nm using 2 photon absorption (Murphy-DuBay et al., 2008). Parallel lithography has been done using an array of apertures exposed with a single laser source to create many patterned lines (Uppuluri et al., 2010).

2.2 Fabrication of Bowtie Apertures

The fabrication of a bowtie aperture can be done using several approaches. The distance of the gap and the edge radius around the exit side of the aperture are of critical importance to improve its performance. It has been shown that the size of the gap is directly related to the size of the light spot (Murphy-DuBay et al., 2008). Focused Ion Beam (FIB) milling is one of the most used tools to fabricate apertures because it does

not require many steps. A problem with FIB is that it can produce apertures with corners that do not have straight edge due to the resolution limit of the Gaussian-profiled beam. Because of this, the effective gap is larger and hence the size of the focused spot.

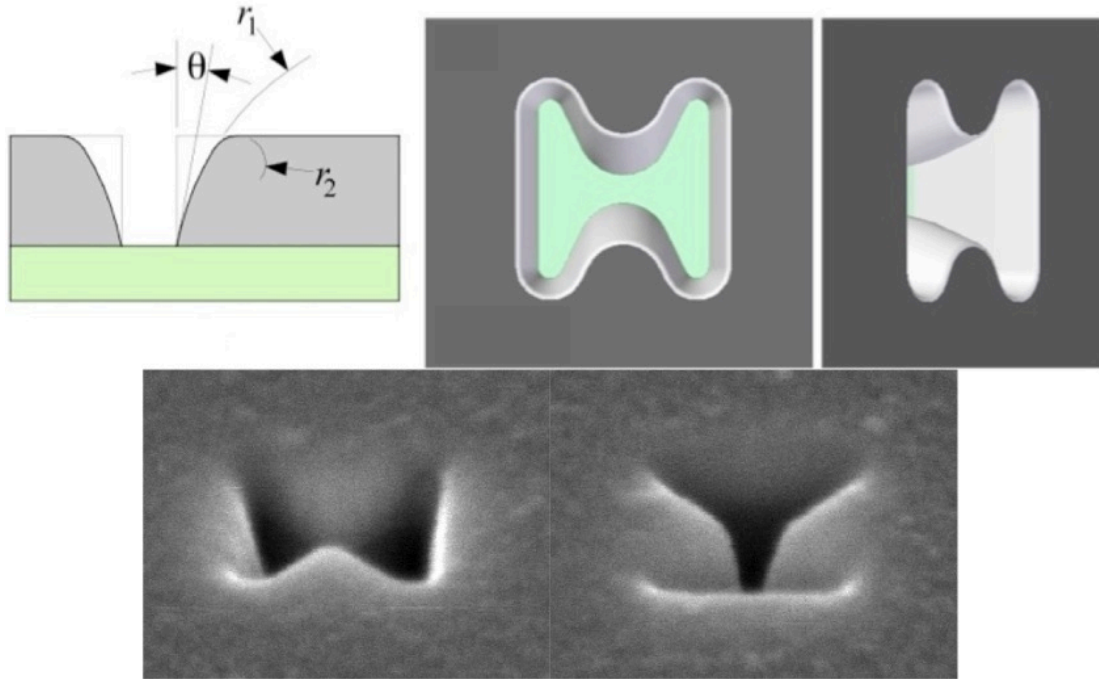


Figure 2.1: Schematic of a real bowtie showing the increase in gap distance on top (Kinzel, 2010). SEM images of a real bowtie on top different rotations viewed at a stage tilt angle of 52° .

Figure 2.1 shows schematics and SEM images of the bowtie apertures that show the round edges that are caused by the conventional FIB milling process. The pattern used to define the bowties was called from an external file called a stream file. More detail about stream files is presented in section 2.2.1. The beam current used to mill the shown aperture was of 10 pA. Similar bowties were fabricated for experiments made for parallel nanolithography (Uppuluri, 2010). The schematics shown at the top of Figure 2.1 were used for EM models of these apertures (Kinzel, 2010). It has been proven using EM simulations that straight edges and sharp features can improve the near field enhancement of an aperture (Kinzel, 2010). Figure 2.2 shows how the electric field for a real tapered aperture compares to an ideal aperture with straight edges. For an aperture with straight edges, the field is more intense and localized. Having an effective larger

gap can affect the resolution of a lithography pattern by widening its smallest dimension by almost twice and in some cases even creating two separate spots. Strategies to improve the geometry of the bowtie have been tried, including using FIB and electron beam lithography. In this section we discuss these strategies.

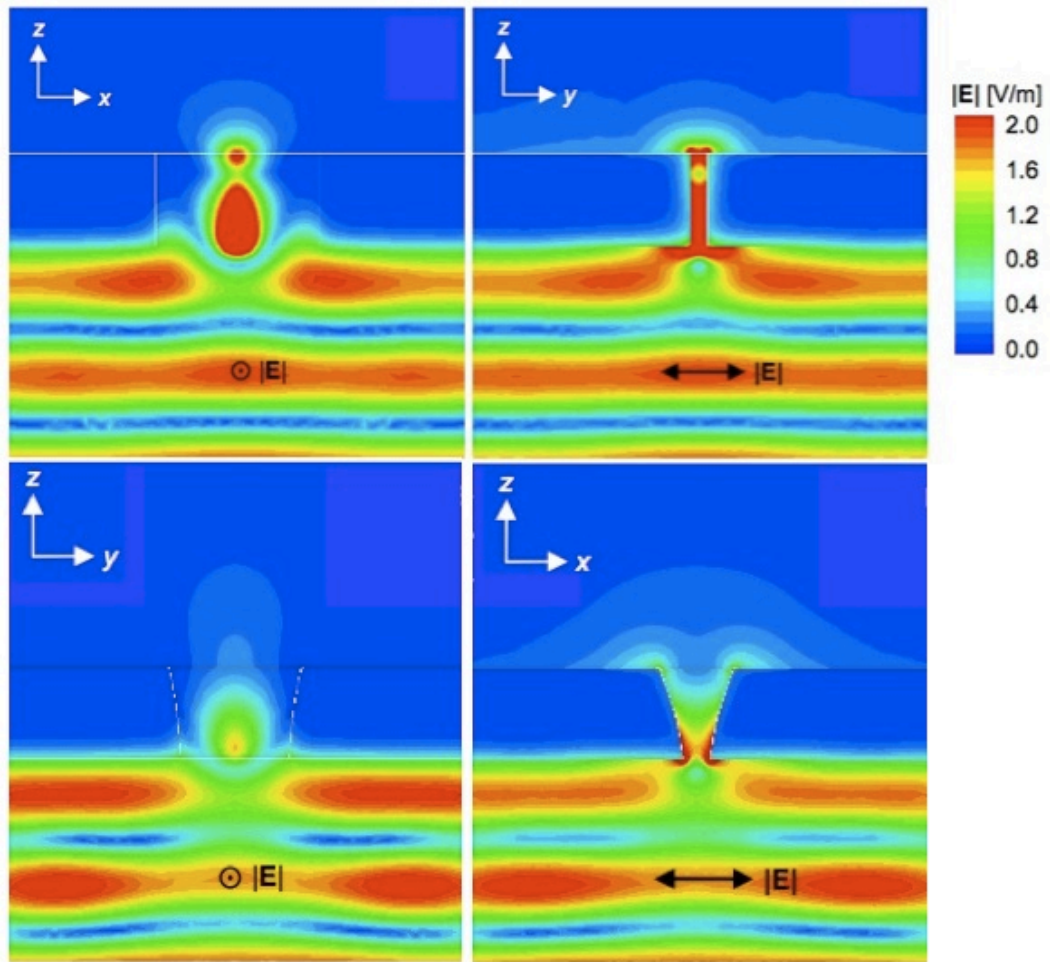


Figure 2.2: Ideal sharp VS real curved edge bowtie aperture (Kinzel, 2010).

2.2.1 Focused Ion Beam Milling

Focus Ion beam (FIB) is a great nanofabrication tool for the creation of bowtie aperture. Using FIB for ridge apertures requires only few steps like depositing a metal film and then milling it. Gallium ions bombard the surface and transfer their momentum, which can result in an ion implantation or in the displacement of atoms to the outside of the substrate.

A good sharp image is important to fabricate a good bowtie aperture with FIB. A specific focusing area in the sample can be delimited. A sharp image is indicative of a well-focused beam and will yield a sharp milling. A large particle is a great place to obtain a good initial image. Several apertures can be milled close to the focused particle. Both focus and stigmatism should be corrected to obtain a sharp image. Milling and image sharpening can be repeated until good apertures are created. A problem that occurs during this iteration is that taking snap shots to access the sharpness of the milling can be detrimental to the top layer. Care should be taken and important or extensive areas of the sample should be avoided for beam focusing.

The FIB milling tool can be programmed to create a large array of apertures, which can be used for applications like parallel lithography. The programming is created with a proprietary language called AutoScript™ that automates functions in FEI® workstations. An array code consists of repeating the milling of a pattern in different positions by either moving the stage of the sample or deflecting the beam to different coordinates. Moving the stage is beneficial because large distances can be covered but the precise position of each aperture can't be well controlled due to a large hysteresis. Deflecting the beam can be very precise and produce very regular arrays but the beam can't be deflected more than 50 μm from the center. The largest square array that we can fit inside a 100 μm circle is one with approximately 70 μm side. An array larger than this would require the use of the stage motion. To delimit the geometry of the pattern within the code we have two options. We can either use a series of vectorial basic polygon definitions (circle, box, line, and 4 point polygon) or use a stream file. A stream file is a text file with a list of coordinates on which the beam will stand stationary for a certain specified dwelling times. A stream file can be generated from an image in bitmap format, which is convenient because of the variety of possible geometries that can be designed. The drawback is that processing so many coordinates can slow down the automatization. Using a vectorial command to define the pattern geometry does not require calling an external file and runs much faster, especially if the pattern consists of a simple combination of simple polygons. Creating a large array of 1000 bowties would require a lot of file processing. To fabricate an array of 32 X 32 apertures in an area of

70 μm X 70 μm we used vectorial commands to define the geometry of the apertures and beam deflection commands to fabricate apertures in each position of the array (Wen et al., 2015).

2.2.2 Sacrificial Layer

We have made attempts using sacrificial layers together with FIB milling to improve the sharpness of the bowtie. A sacrificial layer is one that is coated on top of the aperture metal layer before the aperture is created and then removed after the bowtie is milled. As shown in Figure 2.3 most of the unwanted curvature should be inside the sacrificial layer.

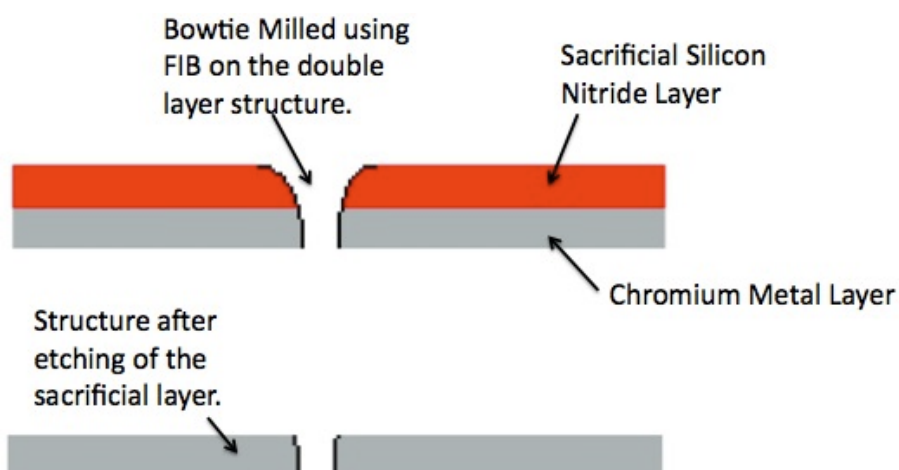


Figure 2.3: Schematic showing the use of a sacrificial layer to eliminate rounded edges of the aperture caused by FIB milling.

Figure 2.4 shows an attempt to use a 140 nm sacrificial layer of silicon nitride deposited using plasma enhanced chemical vapor deposition (PECVD). For this fabrication the FIB current used was of 10 pA. Milling times shown in Figure 2.4(a) influence the depth of the mill. The standard time used by our group for milling bowties at 10 pA without sacrificial layer is around 1 second. To mill through the sacrificial layer we need to mill for longer times. Milling times ranged from 3 s to 36 s. Buffered oxide etch (BOE) was used as shown in the Figure 2.4 (c)-(f) without seeing considerable change in the etch residue around the bowties. The sample was etched for 1 minute, imaged with SEM, etched for an additional 14 minutes, and then imaged again. It can be

seen that some bowties have some unwanted etch resistant deposition around them. This debris around the apertures could not be etched away selectively. The etch rate of the silicon nitride is very fast and it seems that 1 minute is enough to etch the complete layer. The sharpest result was obtained with the lowest milling time of 3 seconds. We could observe that the presence of the sacrificial layer did not extend the milling time significantly. We also studied the effect of the thickness of the sacrificial layer on the gap and the straightness of the edge. On different samples we used a thicker sacrificial layer and fabricated apertures using the same milling times as shown before.

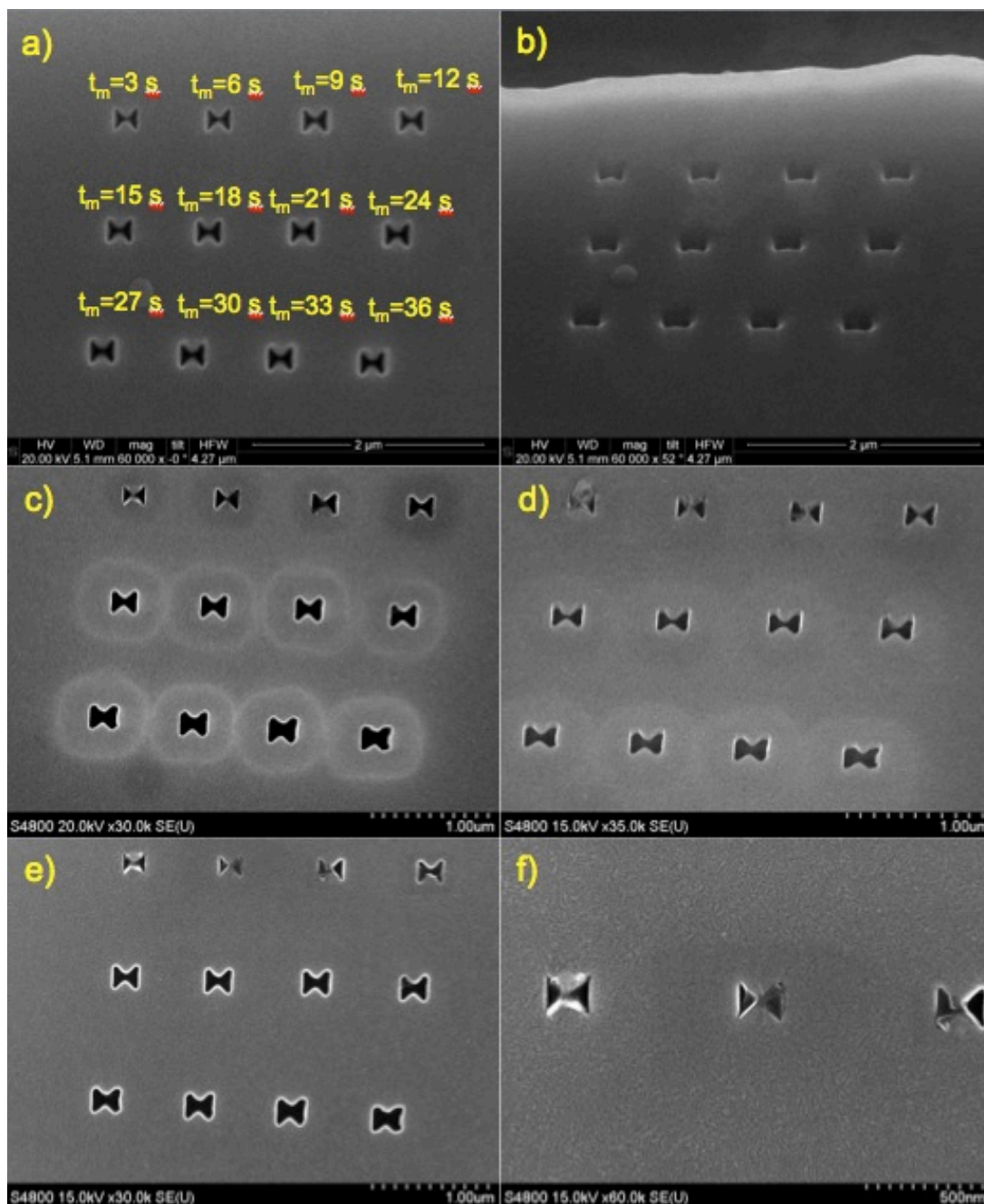


Figure 2.4: Using 140 nm of PECVD silicon nitride as sacrificial layer. Milling time for bowties ranges from 3 s to 36 s. Inserts a) and b) are the top and tilted respectively SEM images immediately after milling the silicon nitride layer. Inserts c) and d) respectively are top and tilted view after 1 minute of buffered oxide etching (BOE). Inserts e) and f) are 30 KX and 60 KX top views respectively of the same array after 15 minutes on BOE.

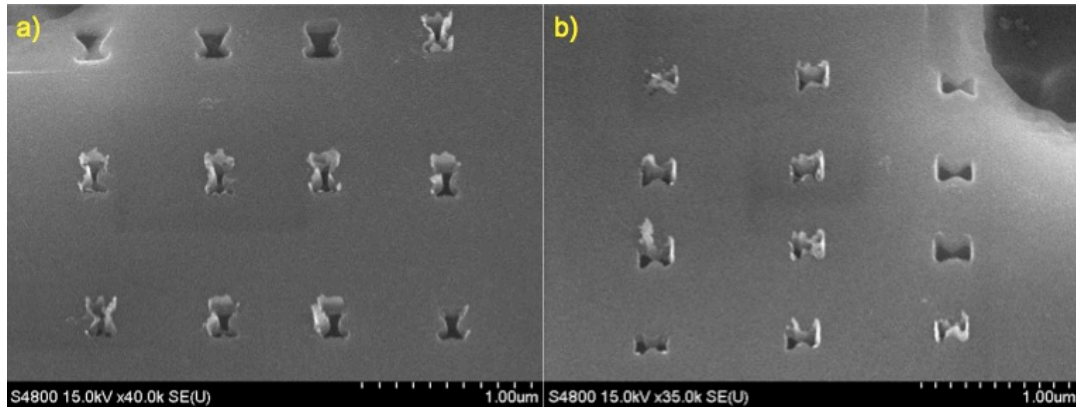


Figure 2.5: Using 270 nm of PECVD silicon nitride as sacrificial layer. Insert a) is tilted 33 degrees and b) is an image of the same region tilted and rotated 90 degrees.

Figure 2.5 shows a set of apertures milled using 270 nm of silicon nitride as sacrificial layer after of the substrate was etched with BOE for 15 minutes. These are the same conditions as the same process as inserts e) and f) of Figure 2.4 except that with a thicker nitride layer. The outcome is similar to the one presented in Figure 2.4. A bowtie aperture with straight edges seems to be the product. Similarly a lot of unknown material around the apertures makes them useless for near field applications. Another problem with this method is that the poor conductivity of the silicon nitride prevents a good focus and thus the creation of small gaps. This problem led us to try using metals as sacrificial layer.

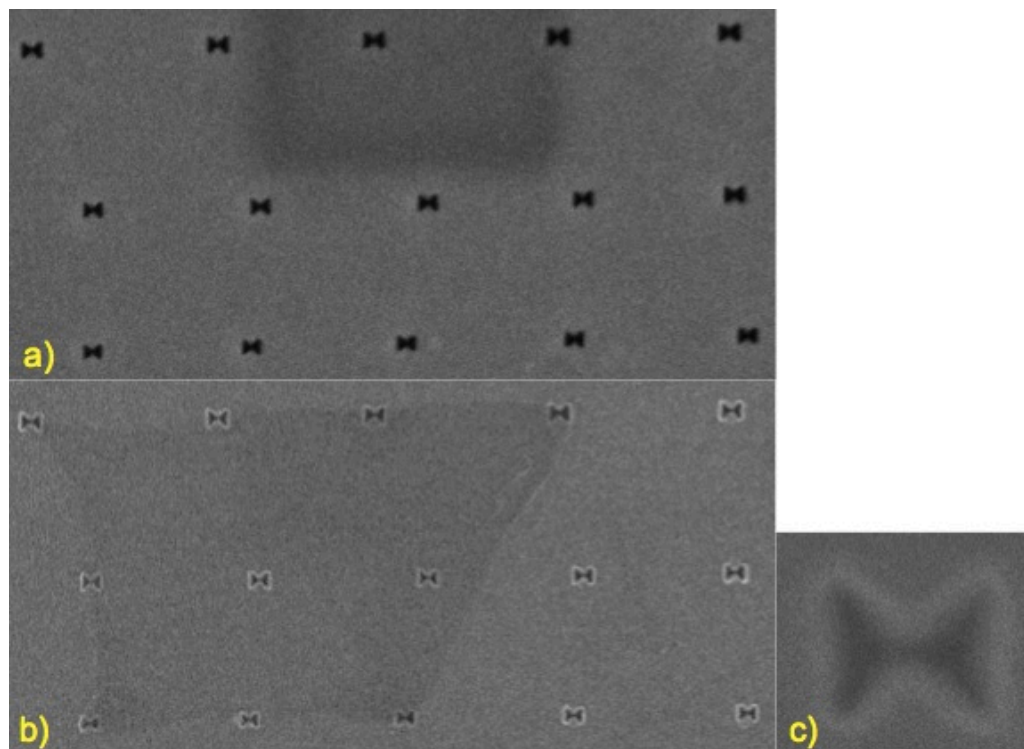


Figure 2.6: Array of bowties using 200 nm of gold sacrificial layer. Insert a) shows the array right after FIB milling, b) same region after using gold etchant, and c) is a zoom in view of b).

Figure 2.6 shows the results after the same procedure was made using a 200 nm of sacrificial Au layer. The sacrificial layer was etched using a commercial Au etchant that would not affect the Cr. As shown in the image it can be seen that gold does not serve very well as a sacrificial layer. Inserts b) and c) show a curvature around the bowtie. This is probably because gold is a much softer material and has a higher yield to ion bombardment. We can also see the presence of a thin layer on a section of the area that was exposed to the ion beam. We suspect that the etching rate of the sacrificial layer in this region can be impacted by the implantation of Ga ions.

Considering that chrome has a lower yield than gold and that gold did not work well as a sacrificial layer, we decided to invert the layers. A layer of 120 nm of Cr was coated on top of gold. Figure 2.7 shows the results after etching the Cr with a commercially Cr etchant. It seems that the edges of the aperture are straighter but there is a lot of unwanted material that was not etched. The current used was of 10 pA and the

milling times are shown in the figure. The bottom insert shows particular bowties that had a layer of an unwanted material surrounding the aperture.

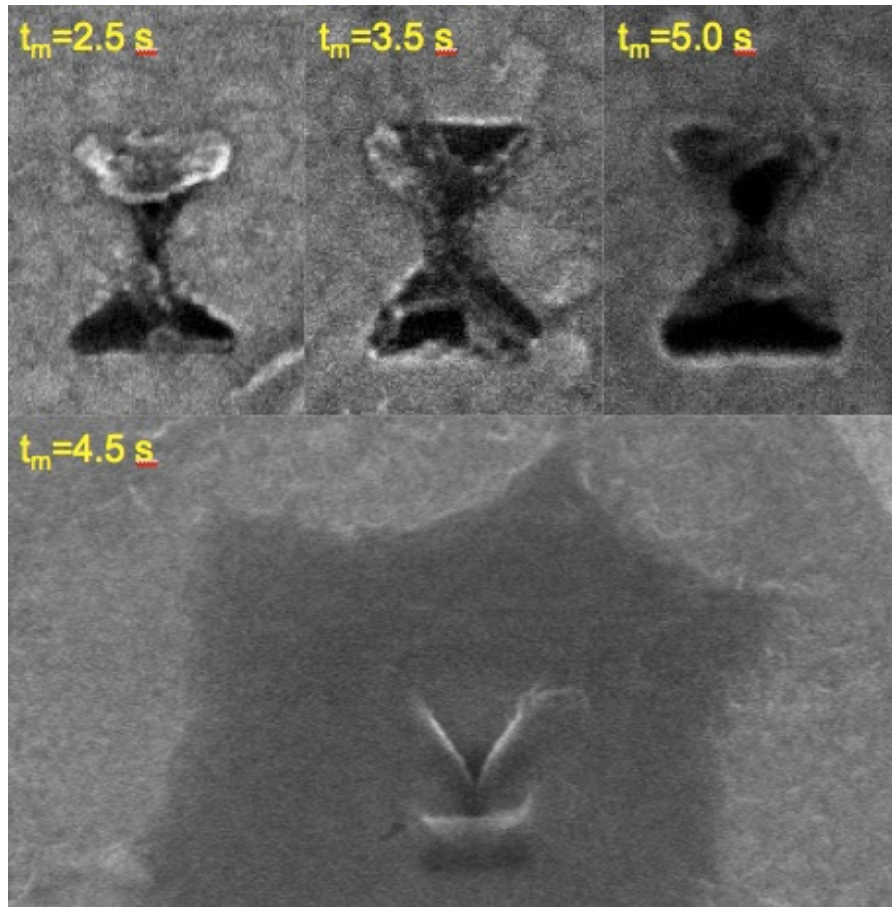


Figure 2.7: Bowtie apertures using sacrificial layer of 120 nm of Cr on top of Au layer. For the insert showing a milling time of 4.5 seconds there is an unwanted layer around the aperture that could not be etched away.

Figure 2.8 shows an attempt using 100 nm of silicon as a sacrificial layer. For this fabrication the FIB current used was of 1 pA. Milling times ranged from 0.5 s to 5.0 s. A solution of potassium hydroxide (KOH) was heated to 120°C and used to etch the sacrificial layer by submerging the sample for 10 seconds after the milling was done. This was supposed to etch all the silicon away. Instead there seemed to be a zone that was resistant to etch.

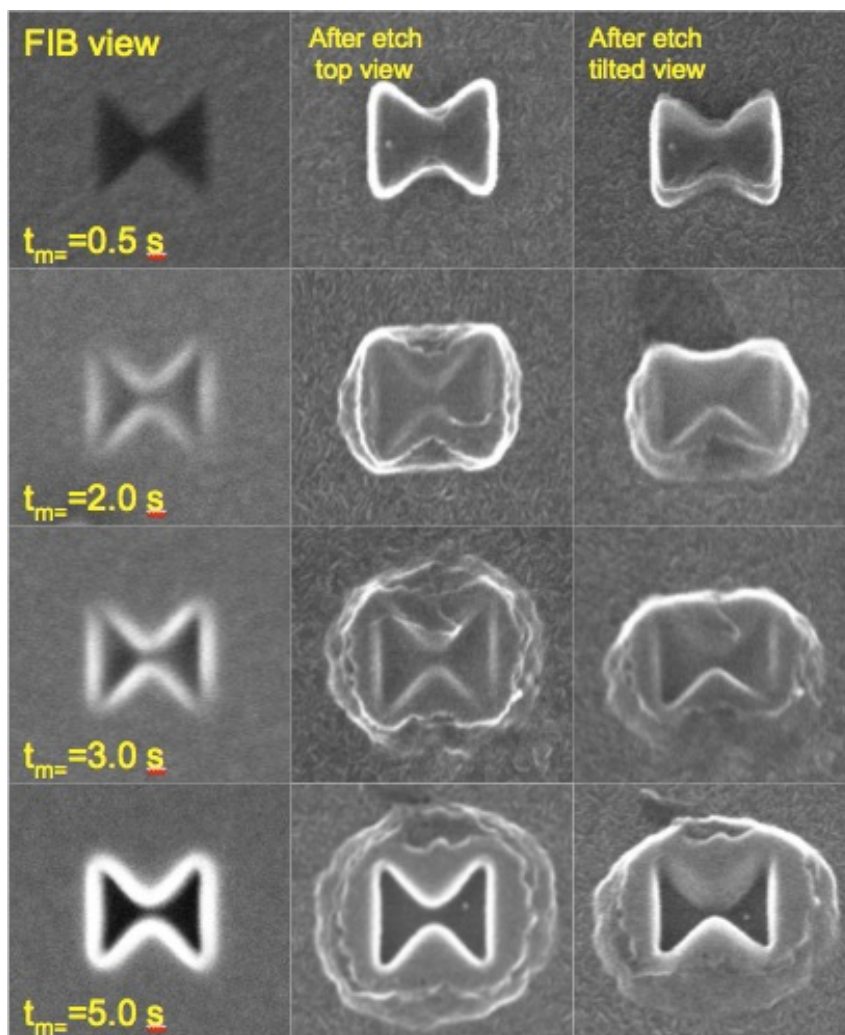


Figure 2.8: Milling of a bowtie in a silicon chrome layer arrangement and images after removal of Si sacrificial layer. 1st column is the SEM image of the milled silicon layer, 2nd column is a top view after the silicon was removed, and 3rd column is the tilted view of the 2nd column.

After trying many different types of sacrificial layers we were unable to obtain clean apertures without residue material that could not be etched. One explanation for this problem is that gallium ion implantation changed the etch rate around the bowtie. Another explanation for this problem could be the redeposition of aperture material in the surfaces next to the milled bowtie. It was observed in some cases that when the milling time was longer there was more resistance to etching around the apertures. This can be an indication that longer times of exposure lead to more ion implantation. It is very important to obtain clean areas around the apertures that allow for an uninterrupted

approach between the apertures and other substrates. The sacrificial layer method needs to be improved. It has been demonstrated here that if the method is improved, it would produce straight and sharp apertures that could be used for better light confinement.

2.2.3 E-beam Lithography

We also tried e-beam lithography to pattern the aperture bowties into a substrate. Different process flows using positive and negative resist are reported here. One option when using a positive resist like PMMA would require exposing and developing the area of the aperture. The positive photoresist should be thin in order to offer good resolution. The unexposed area could serve as a mask to etch a metal layer. We did not try this approach because PMMA is a soft material for which a thin layer would etch away quickly. Another option when using PMMA would require exposing the area surrounding the aperture. A layer of metal can be coated after developing and a lift-off process would produce an aperture.

If a negative resist like Hydrogen silsesquioxane (HSQ) is used then the aperture geometry could be patterned into the resist. After developing away the area surrounding the aperture, a metal layer could be deposited and a lift-off process would produce an aperture. For the negative HSQ resist, we could alternatively pattern the area surrounding the aperture in order to create an HSQ aperture to etch through. A problem with the option is that exposing around the bowtie will take considerably much longer time because is a far larger area. Lift-off process using PMMA and HSQ were tried. The etching of Cr layer was not tried due to the difficulties of obtaining a good gap control during the exposure and developing of HSQ.

The first attempt to make bowtie apertures with e-beam lithography was done using HSQ resist. HSQ Fox 15 resist was coated on top of a Cr layer at 4000 RPM for 45 sec. A soft bake was made for 3 minutes at 120°C. The pattern was exposed around the area of the apertures with a current of 750 pA. The actual outcome of the geometry is difficult to predict because of lithography bias and proximity effects. As it should be done usually we tried several cases to help us predict a better outcome. We draw an array

of bowties, each constructed by placing two triangles together. Figure 2.9 shows an arrangement in which these triangles were placed at different distances away from each other and also at different distances merging into each other. The same arrangement for gap separation was used for 4 different cases: one bowtie with dimension of 170 X 170 nm, one with 170 X 170 nm with a gap designed within the triangle, one with 200 X 200 nm, and one with 200 X 200 with the same gap. Exposing a large area around a small-intended aperture creates the risk of over exposing. After exposure, the sample is submerged in tetramethylammonium hydroxide (TMAH) 25% base solution in water and developed for 45 seconds. Figure 2.9 shows the minimal dose for which we experienced overdose, which was of $750 \mu\text{C}/\text{cm}^2$. The bright spots in the image are exposed chrome. The other spots are apertures that were not properly developed. Figure 2.10 shows the results after developing for a sample exposed to a dose of $650 \mu\text{C}/\text{cm}^2$, which is just below the overexposing threshold. The definition of the aperture geometry does not yield the expected ridge apertures.

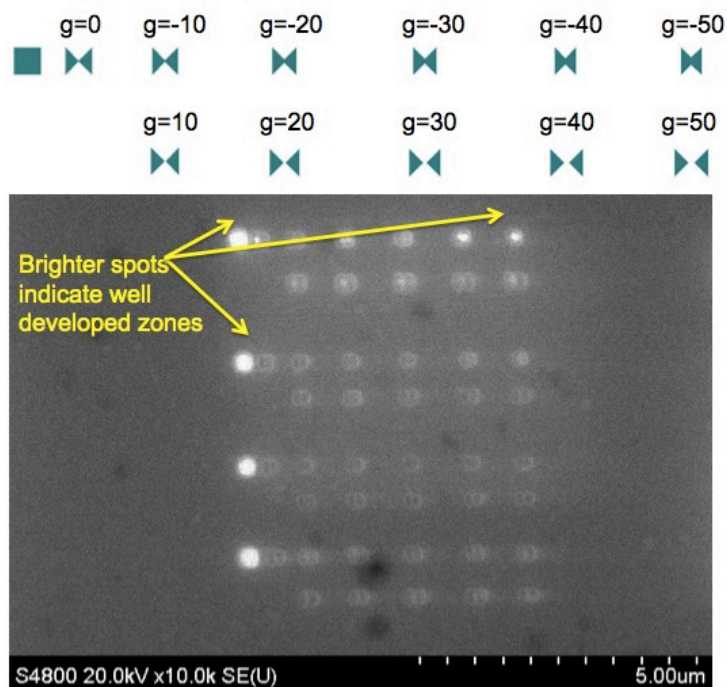


Figure 2.9: HSQ (200 nm thick) aperture array exposed with $750 \mu\text{C}/\text{cm}^2$ dose on the region outside the aperture. The top diagram shows how for each section the gaps between the triangles are changed for dose and proximity effect test.

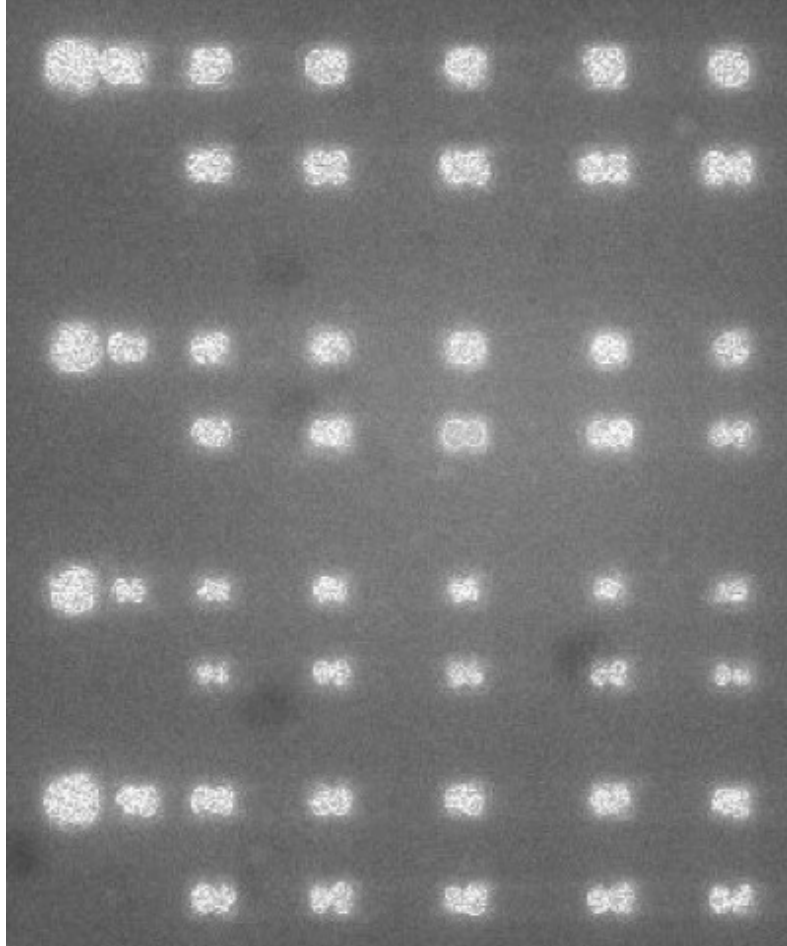


Figure 2.10: HSQ (200 nm thick) aperture array exposed with $650 \mu\text{C}/\text{cm}^2$ dose on the region outside the aperture.

In order to improve the resolution of HSQ e-beam lithography, it has been suggested in the literature that no pre-bake should be done to avoid thermally induced cross-linking (Duan et al., 2011). In order to test this we coated 100 nm of a more diluted HSQ photo resist (HSQ XR-1541-004) at a speed of 4000 RPM. Without prebaking we exposed the substrate to doses starting from $500 \mu\text{C}/\text{cm}^2$. Figure 2.11 shows the results after developing a pattern exposed to a dose of $900 \mu\text{C}/\text{cm}^2$. This is a higher dose than the case showing over developing in Figure 2.9. It is worth to note that there was no over developing here. Figure 2.11 shows no overdeveloping. These bowties have much better shape than the previous cases but no control of the bowtie gap was achieved.

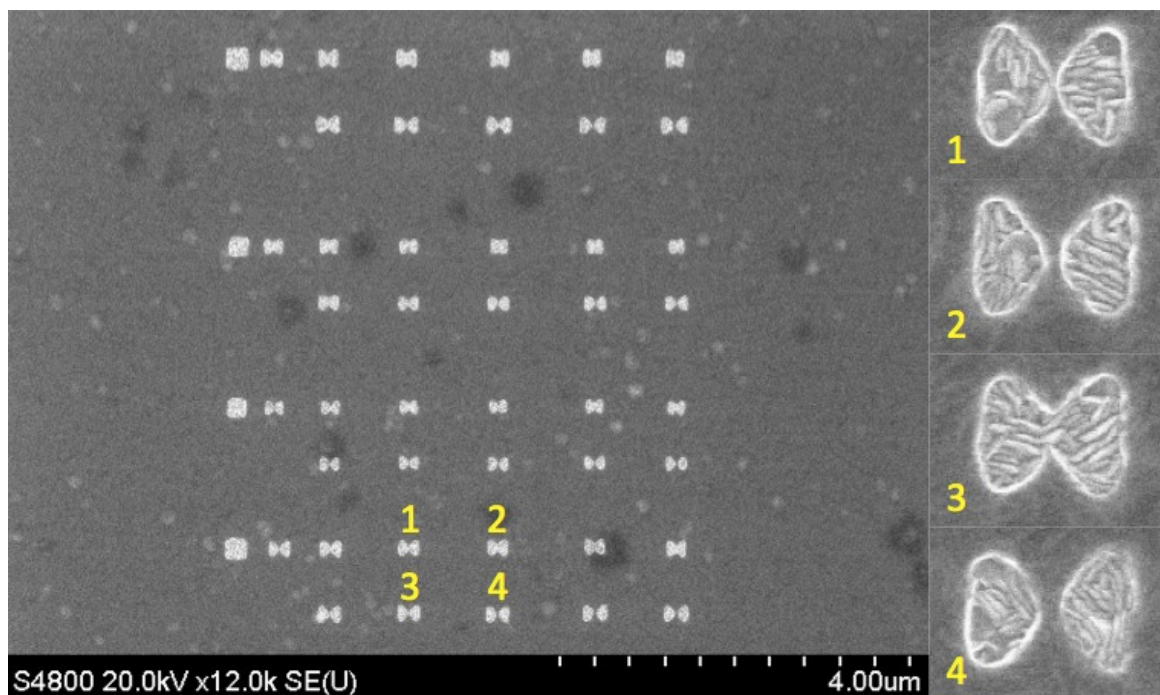


Figure 2.11: Bowtie patterning using HSQ XR-1541 photo resist and no prebake to minimize thermally induced cross-linking.

We attempted to make bowtie antennas by lifting-off gold deposited on exposed and developed PMMA. On top of a commercially available quartz substrate coated with indium tin oxide (ITO) we coated PMMA at 2500 RPM for 45 seconds yielding a thickness of 200 nm. The PMMA was exposed with the same array shown for the previous method with doses ranging from 600-1350 $\mu\text{C}/\text{cm}^2$. Development was made with 1:3 MIBK to IPA solution developer for 50 seconds. We deposited a layer of 60 nm of gold using an e-beam evaporation tool and then lifted-off soaking the sample in acetone for 5 minutes and agitating for 10s with ultrasonic vibrations. Figure 2.12 shows the result of this fabrication exposing with a dose of 1350 $\mu\text{C}/\text{cm}^2$. For a bowtie with designed sizes of 200 nm X 200 nm we obtained a 300 nm X 300 nm antenna with a gap of 21.8 nm. For the ones with designed size of 170 nm X 170 nm we obtained 257 nm with gap size of 38.6 nm. This is a large bias that prevents us from achieving good gap size control when using a 200 nm thick PMMA photoresist.

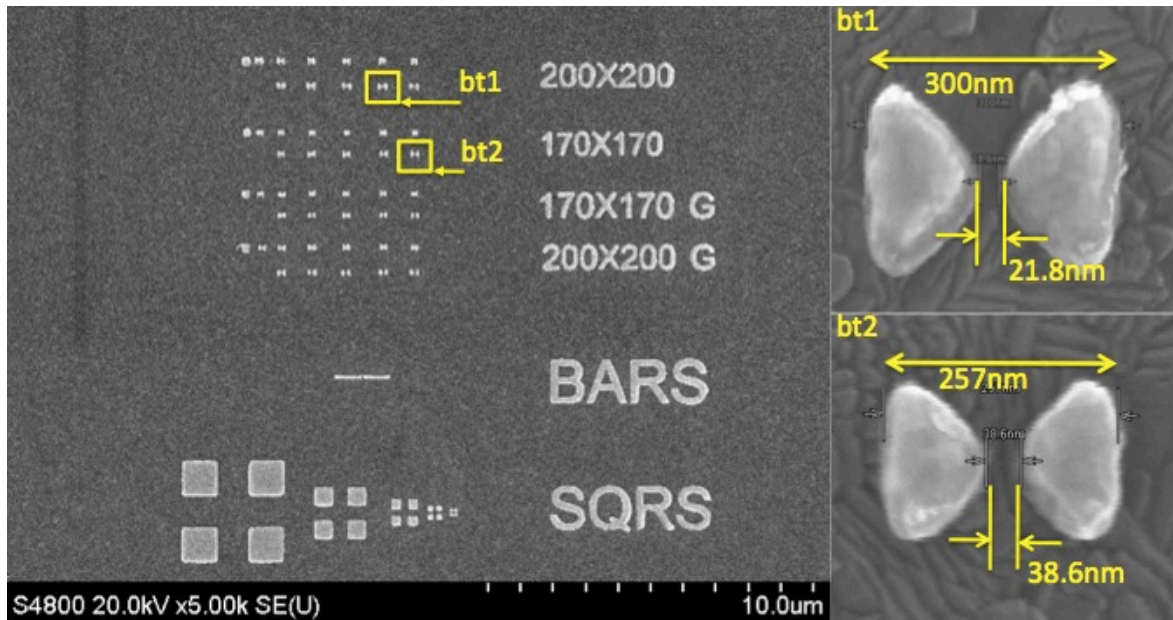


Figure 2.12: Bowtie antennas after lift-off of gold metal on PMMA. The dose used to fabricate the patterns in this image was $1350 \mu\text{C}/\text{cm}^2$.

Using PMMA as photo resist we also created apertures in a different way. We exposed the area around the bowtie to ultimately lift-off gold. The PMMA was coated on top of an ITO coated substrate with a thickness of 200 nm using the same recipe as in the previous method. The pattern was exposed using doses ranging from $400 \mu\text{C}/\text{cm}^2$ to $850 \mu\text{C}/\text{cm}^2$. Due to the proximity effect there can be too much over exposure when exposing very large areas around the bowties. We had to do expose an area as small as $5 \mu\text{m} \times 7 \mu\text{m}$ around the apertures to minimize over exposure and obtain apertures. Figure 2.13 shows the result after a lift-off. The size of apertures shown in b) and c) are of 193 nm and 201 nm which is close to the expected dimension of 200 nm. The problem with this method is that it yields very large gaps and very poor gap control.

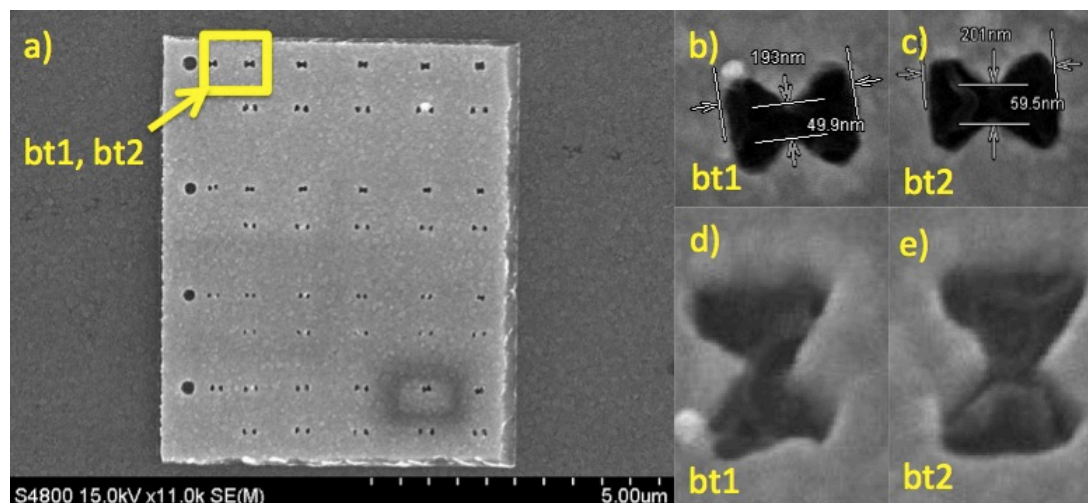


Figure 2.13: Apertures exposing PMMA on the region outside the aperture. (dose of $550 \mu\text{C}/\text{cm}^2$). Inset a) shows the total area exposed showing the 2 bowties for which zooms are shown in b), c) (top view), and d), and e) (tilted rotated views).

We also attempted creating apertures with a lift-off process of a gold layer coated on top of a pattern developed in HSQ resist. Figure 2.14 shows the result after exposing and developing the bowtie area as well as the results after the lift-off. Initially, HSQ was coated at 4500 RPM reaching this angular speed in 0.2 sec and then baked at 130°C for 3 minutes. A test was performed starting with at dose of $600 \mu\text{C}/\text{cm}^2$ and increasing the dose 50 times by a factor of 1.1. Gap separations between the triangles that form the bowties were constrained to 0 nm, 10 nm, 20 nm, and 30 nm. A layer of 70 nm of gold was deposited and lifted-off by submerging the sample for a duration of 3 minutes in a buffered oxide etch (BOE) solution. We agitated with ultrasonic vibrations for the 3 minutes duration. The use of ultrasonic is very important to reduce the amount of debris left on the sample.

Figure 2.14(a) shows a designed 170 nm X 170 nm bowtie made with a dose of $4400 \mu\text{C}/\text{cm}^2$ and a gap triangle separation of 20 nm. For this aperture the result size was of 204 nm before lift-off and 210 nm after lift-off and the gap was of 23.8 nm before lift-off and 41.7 nm after lift-off. Figure 2.14(b) shows a designed 250 nm X 250 nm bowtie made with a dose of $2756 \mu\text{C}/\text{cm}^2$ and an intended triangle separation of 0 nm. For this aperture the result size was of 214 nm before lift-off and 240 nm after lift-off and the gap was of 23.8 nm before lift-off and 45.6 nm after lift-off. Figure 2.14(c) shows a designed

200 nm X 200 nm bowtie made with a dose of $4440 \mu\text{C}/\text{cm}^2$ and an intended triangle separation of 20 nm. For this aperture the result size was of 220 nm before lift-off and 246 nm after lift-off and the gap was of 11.9 nm before lift-off and 41.7 nm after lift-off. Figure 2.14(d) shows a designed 300 nm X 300 nm bowtie made with a dose of $2506 \mu\text{C}/\text{cm}^2$ and an intended triangle separation of 0 nm. For this aperture the result size was of 258 nm before lift-off and 281 nm after lift-off and the gap was of 27.8 nm before lift-off and 41.6 nm after lift-off.

Most of the apertures studied show that gap dimensions are more consistent before lift-off. It also seems like this method is more consistent than the others reported. The gap dimensions increases by twice consistently after the lift-off. There was no specific relationship between the dose and the quality of the bowtie. The images shown in Figure 2.14 show the best results but generally all of the results were not clean and consistent. We suspect that a better gap control can be obtained by using a thinner HSQ layer. After having studied or considered all of the possible methods involving e-beam lithography we were not able to obtain sharper ridge aperture.

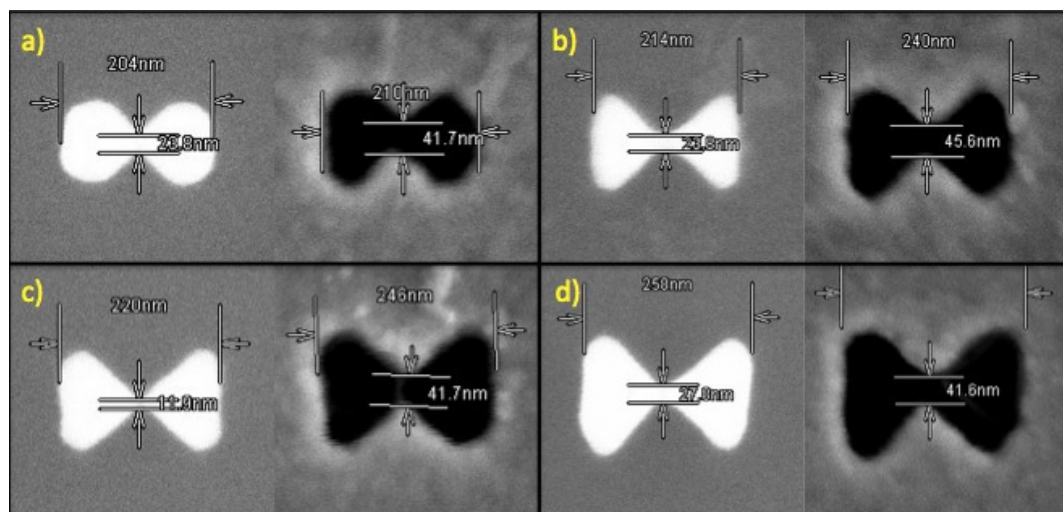


Figure 2.14: Bowtie aperture made after exposing HSQ inside the bowtie area and then making a gold lift-off with BOE. (a) Design of 170 nm X 170 nm bowtie with triangle gap separation of 20 nm. (b) Design of 250 nm X 250 nm bowtie with triangle gap separation of 0 nm. (c) Design of 200 nm X 200 nm bowtie with triangle gap separation of 20 nm. (d) Design of 300 nm X 300 nm bowtie with triangle gap separation of 0 nm.

2.2.4 Transfer of Reverse Aperture Thin Membrane

Milling a ridge apertures in a thin film and inverting the film allows us to have access to a sharp region of the ridge that could potentially give us a more confined near field. Chen et al. (2015) created a suspended membrane on which they deposited a metal layer. A bowtie aperture was milled on one side of the membrane using FIB. The result was an aperture that had an inverted sharp taper at the exit. Using numerical simulations and s-NSOM measurements, they proved that they could produce optical spots with lateral sizes below 20 nm. Leen et al. (2010) did similar work. They milled a C aperture in a suspended membrane and proved that reverse milling could be useful for optical data storage.

Our group was interested in making a design for a parallel lithography setup using reverse milled apertures on thin films. We suspected that combining the parallel lithography setup presented in section 2.4 together with the reverse film we would obtain massive lithography pattern with resolutions below our best reported (Wen et al., 2015). The main setup is mostly exactly the same as the one reported in 2.4. The only difference is the metal coated that surrounds the island where the apertures are located. Instead of milling the bowtie apertures on top of the island, we intended to mill the apertures in a thin membrane and try to transfer the membrane on top of the island.

Before performing the thin transfer procedure we tested reverse milling on a membrane to make bowtie apertures. Similar to regular milling of aperture bowties, the inverse bowtie requires a dose test that depends on the thickness of the metal layer. Figure 2.15 shows a milling dose test that corresponds to a thickness of 50 nm of silicon nitride and 90 nm of gold. The milling was done through the nitride side and the images shown are through the gold side. The doses are shown as depth of milled silicon, which is a parameter specified in the software. The 1st, 2nd, and 3rd, column show a top, tilted (52°), and tilted-rotated (52°-90°) views respectively. We can clearly see a taper that could favor the confinement of light.

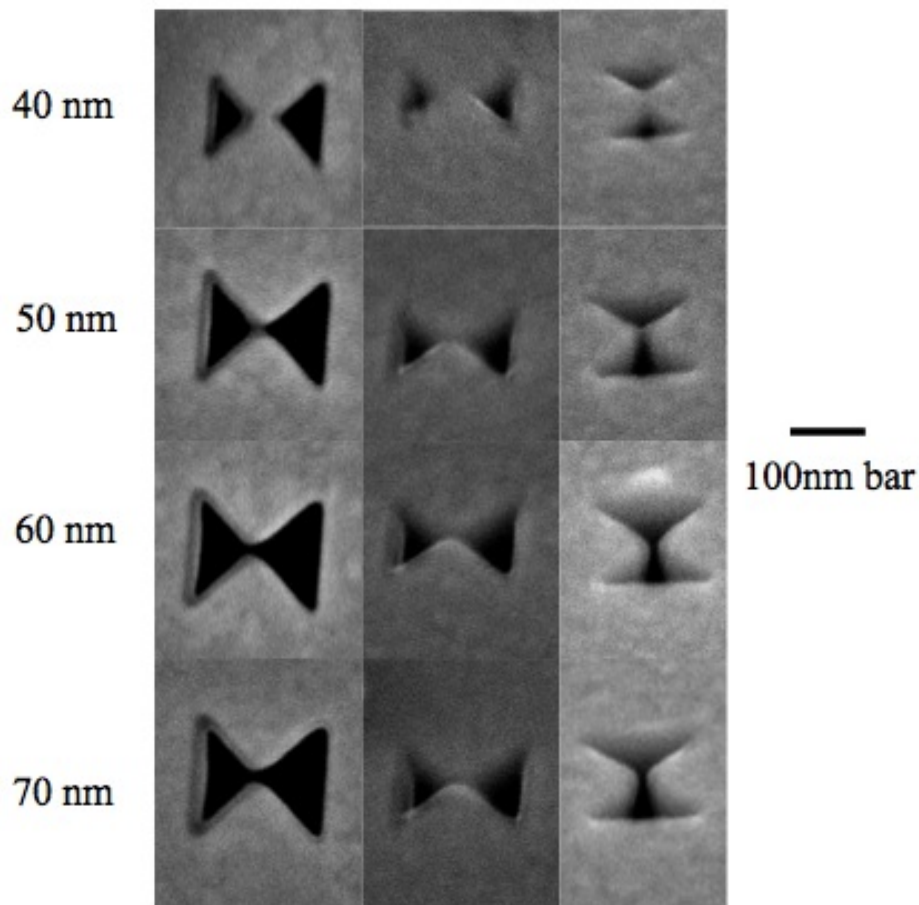


Figure 2.15: Dose test milling bowtie apertures on Au through a silicon nitride membrane. Thickness shows are based on silicon milling.

The transfer of an inverted aperture to the top of an island requires the preparation of the substrate with the island as well as the wafer with the thin membrane. To prepare the substrate with the island we first need to do the steps that require submerging the substrate into solvent or developing chemicals. The transfer of the thin membrane is the last part of the fabrication. Table 2-1 shows the process flow of fabricating the island substrate and making it ready for aperture transfer. The island for this experiment is created using the same procedure used to build the island for our conventional parallel lithography. Section 2.4 describes in more detail this process. Steps 1 and 2 of Table 2-1 correspond to the same step 1 and 2 presented in Table 2-3. In the process presented here we leave the island-etching mask attached to the substrate as opposed to our conventional method. We wanted to uncover the island immediately before the transfer process to

protect the top from contamination during intermediate steps. After creating the island we coated the metal that would serve to stop the background light around the substrate. We created a mask made of gel strips to lift-off the coated metal. We manually cut two strips of adhesive gel and placed them on top of the substrate as shown in step 3 of Table 2-1. It is best if the windows are placed in such a way allowing the centers of the ISPI gratings to be 5 mm apart. At this point we coated the metal and manually lifted-off the coated gel strips. During lifting-off the metal, we uncovered the windows that will have the ISPI grating as shown in step 4 of Table 2-1. To fabricate the ISPI grating we coated fox 15 HSQ at 2000 RPM reaching this speed in 3 seconds and then spun for a duration of 45 seconds. The HSQ was soft-baked at 120°C for 3 minutes. Section 2.3 contains the details as to how this ISPI grating works and how is fabricated using e-beam lithography. Once the island substrate was finished we attached it to the assembly used for the thin membrane transfer. The island substrate was attached together with 2 other quartz substrates to a standard glass slide using baked photoresist AZ1518 as a glue. A drop of photoresist was placed in between the substrates and the glass slide. Then, the entire arrangement (shown in step 6 of Table 2-1) was baked in a hot plate at a temperature of 125°C for 10 minutes.


Table 2-1: Process for preparing the island substrate for thin membrane transfer.

#	NAME	DESCRIPTION	SCHEMATIC
1	Patterning island mask	After cleaning prebaking and coating adhesion promoter, coat PR AZ1518 at 2500 RPM for 45 seconds, soft bake at 100°C for 5 minutes. Expose for 17 seconds at 10 W/cm ² . Develop in AZ developer for 9 seconds and then hard bake at 120 for 5 minutes.	

Table 2-1: Continued.

#	NAME	DESCRIPTION	SCHEMATIC
2	Island etch and thin conductive layer coating	BOE etch for 114 minutes to obtain a 10 μm height island. Without removing the island mask coat a thin layer of 3 nm of Cr.	
3	Covering the windows with soft gel layer.	Cut two strips of gel and place them where the ISPI windows will be. The center of the ISPI window patterns should be 5mm apart.	
4	Coat Au and lift-off by stripping gel.	Coat Au using e-beam evaporation tool and remove the gel strips to uncover the windows where the ISPI patterns will be fabricated.	
5	ISPI phase grating	Coat of Fox 15 HSQ at 2000 RPM reaching that speed in 3 seconds. Exposed with a dose of 1100 $\mu\text{C}/\text{cm}^2$. Developed in TMAH for 45 seconds. Island mask will dissolve in TMAH.	

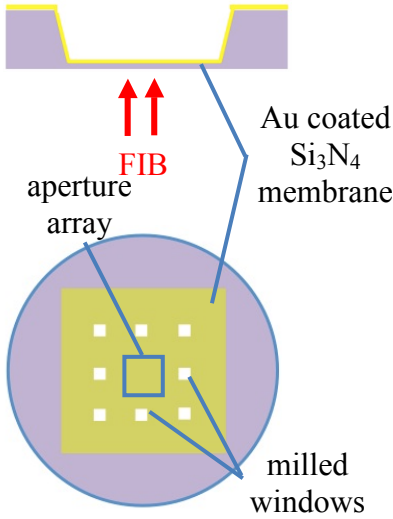
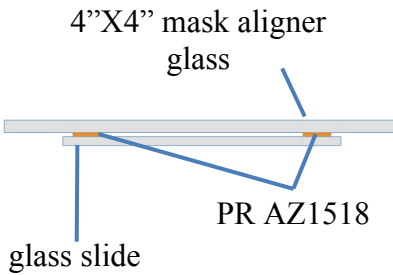
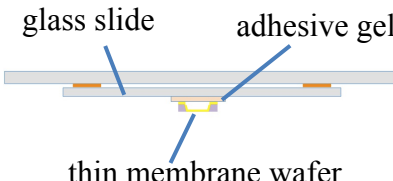
Table 2-1: Continued.

#	NAME	DESCRIPTION	SCHEMATIC
6	Island substrate assembly	Attach the island substrate to a standard 75 mm X 25 mm X 1 mm (3 " X 1 " X 1 mm) glass slide. At the same time stick 2 reusable quartz substrates to the sides of the island substrate. Attach by placing drops of PR AZ1518 between the glass and the quartz and bake at 125°C for 10 minutes.	

Besides preparing the island we need to prepare the thin wafer and then make it part of a different assembly. The 3 mm diameter wafer is a commercially available membrane from TED Pella. The membrane is made of silicon nitride, which is suspended in a window of 500 μm X 500 μm with a thickness of 50 nm. The schematic of step 1 in Table 2-2 summarizes the milling fabrication done to the thin membrane wafer. It shows the top and side view of the wafer. We started by coating 5 nm of titanium followed by 90 nm of gold on the back side. Windows with dimensions of 25 μm X 25 μm were milled to allow for better alignment by increasing the visibility of the island during the thin membrane transfer. The aperture array is fabricated in the middle of all the milled windows. The transfer process is made in a mask aligner that allows us to position the aperture array on top of the island. In order to use the mask aligner we need to attach the thin membrane wafer to a mask aligner glass. We attached first a standard 3 " X 1 " glass slide to a 4 " X 4 " mask aligner glass using PR AZ1518 as a glue. Two small drops were trapped between the two glasses and baked in a hot plate at 125 °C for 10 minutes. The thin membrane wafer was attached to the mentioned glass slide by using adhesive gel. The adhesive gel was cut with a razor blade to a dimension slightly larger than the wafer so the wafer would completely lie inside the gel. This adhesive gel gave the thin membrane wafer the flexibility to move around and to conform to the alignment of the island substrate. As it was seen in other methods, if the thin membrane wafer is rigidly attached to its assembly and the wafer is not parallel to the island substrate, the approach might not be possible. We need to take into consideration

that the island is only 10 μm tall with sides of around 120 μm , while the wafer is 3 mm wide. A small misalignment between the wafer and the island substrate is enough to prevent the thin membrane from ever contacting the island. Instead, the edges of the thin wafer would contact first and small silicon pieces would yield to the pressure created by the approach. This would release a lot of broken particles to the area and the whole process would need to be redone.

Table 2-2: Process for preparing thin membrane wafer for transfer.

#	NAME	DESCRIPTION	SCHEMATIC
1	Gold coating and aperture FIB milling.	Coat the thin membrane wafer with e-beam evaporated 5 nm Ti and 90 nm Au on the tapered window side. Mill the apertures from the silicon nitride side. Mill windows with sides 25 μm X 25 μm for visibility while transferring the membrane.	 <p>The schematic for step 1 consists of two parts. The top part is a cross-sectional view of a tapered window in a substrate. A thin yellow layer, labeled 'Au coated Si₃N₄ membrane', is deposited on the inner surface of the tapered window. Two red arrows labeled 'FIB' point upwards towards the membrane, indicating the location of the aperture array. The bottom part is a top-down view of a square substrate with a 3x3 grid of small white squares, labeled 'milled windows'. A blue square highlights the central window, which is shown in a larger, magnified view.</p>
2	Attaching glass slide to mask aligner glass	Attach a standard 75mmX25mmX1mm (3"X1"X1mm) glass slide to the mask aligner glass using PRAZ1518. Attach by placing drops of PR AZ1518 between the glasses and bake at 125°C for 10 minutes.	 <p>The schematic for step 2 shows a cross-section of a 4"X4" mask aligner glass (top layer) and a glass slide (bottom layer) attached together. The adhesive is labeled 'PR AZ1518'.</p>
3	Attaching thin membrane wafer to glass slide	Cut a layer of gel membrane and attach the thin membrane wafer to the glass slide attached in step 2.	 <p>The schematic for step 3 shows a cross-section of the glass slide (top layer) and the thin membrane wafer (bottom layer) attached together. The adhesive is labeled 'adhesive gel'.</p>

Once the mask aligner assembly was ready we proceeded to prepare for final alignment and approach of the thin membrane to the island substrate. Two different adhesives were actively used during the approach. One was a commercial cyanoacrylate adhesive (Krazy glue©) used to coat the top of the island where the membrane will land after approach. It was used because it could be coated thinner than other adhesives, which helped us avoid unwanted deposition of residue on top of the aperture film. The other adhesive used was a commercial UV curable Norland optical adhesive (NOA81 Thorlabs). It was dropped on top of the two quartz substrates that were contacting the glass slide to which the thin membrane wafer was attached. We used this adhesive to make an approach and alignment with special freedom and once the aperture array is in position on top of the island we can cure the adhesive. Both assemblies remained in place after curing the adhesive. Table 2-3 shows the approach and release steps of the thin membrane transfer process. It starts with applying the adhesives discussed previously and mounting the assemblies into the mask aligner. The 4" X 4" glass was placed into the mask aligner by activating the vacuum suction. During alignment, the milled windows shown the schematic of step 1 in Table 2-2 were used to look through the gold membrane and see the island. Approach was made and noticed when the thin membrane would deform and conform to the shape of the island. If there is a hard particle close to the island, the thin membrane will brake during approach, so we need to make sure that there are no particles in this region. After the approach we exposed both assemblies to the UV light of the mask aligner (dose of 10 mW/cm^2 for 15 minutes). The curable adhesive got hardened and both assemblies got attached. The whole assembly was taken out of the mask aligner by deactivating the vacuum suction. We let the super glue dry overnight to make sure that good adhesion between the thin membrane and the island was achieved. Acetone was dropped carefully on the edges of the glass slide that was attached to the mask glass aligner to release the rest of the assembly. Then acetone was dropped carefully on the edges of the quartz substrates that were attached to the glass slide. During release we needed to make sure that the island and the thin membrane did not come into contact with acetone since cyanoacrylate is very soluble in it. This means that we needed to find a more permanent way of attaching the membrane because the

island substrate is periodically cleaned between lithography experiments with solvents. Steps 4 to 6 of Table 2-3 shows a procedure that we developed to ensure the permanent attachment of the thin membrane to the top of the island. We started by milling channels around the island (step 4 of Table 2-3). It is important to ensure that all of the gold's thickness is milled. We followed by a platinum deposition around the island that will isolate and attach the membrane to the substrate. Finally with a regular acetone cleaning we got rid of all the membrane that surrounds the attachment.

Table 2-3: Approaching and attaching the membrane.

#	NAME	SCHEMATIC
1	Place adhesive and assemblies in place.	
2	Align, approach, cure, and allow adhesive to dry.	
3	Detach thin membrane wafer and island.	

Table 2-3: Continued.

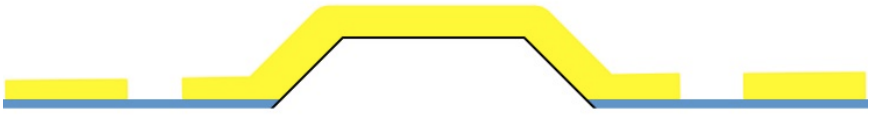


#	NAME	SCHEMATIC
4	Mill for membrane attachment	
5	Deposit platinum for membrane attachment	
6	Clean with acetone for membrane attachment	

Figure 2.16 shows the island after stitching a part of the membrane (left) and then the same island after being cleaned with acetone (right). We can see the parts of the membrane that remained and the parts that were washed away.

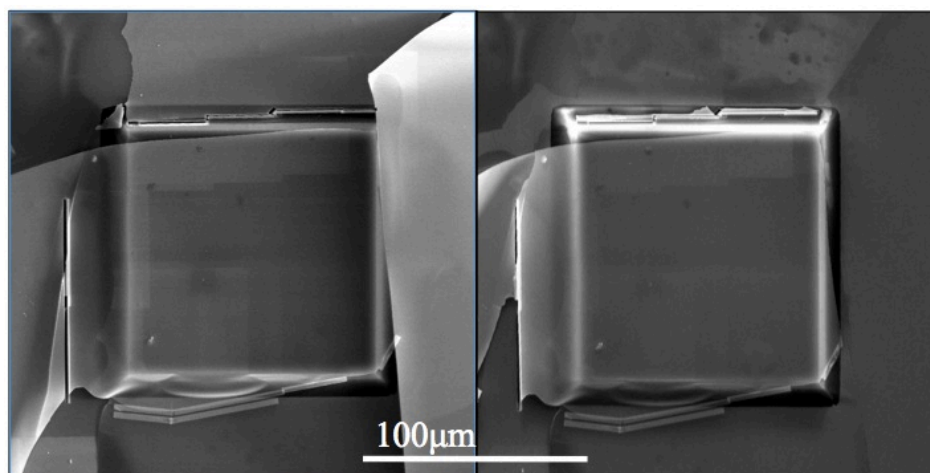


Figure 2.16: Attaching a membrane using platinum deposition. Left shows after Pt deposition and right shows after washing away using acetone.

Even though a lot of these steps were proven to work properly, we could not finish the entire procedure and obtain a transfer with an array of apertures that could be

used for parallel lithography. This procedure contained a lot of steps, which increases the chances of having many particles. In order to optimize this process we would need to find ways of maintaining all of the components clean at all times. There were many other similar methods that were unsuccessful as well. This section presented the method with more chances to obtain a repeatable process for thin membrane transfer.

2.3 Interferometric Spatial Phase Imaging for Gap Control

Near field lithography requires the precise control of the position between a mask and a substrate. The confinement in the near field region around the bowtie aperture diverges quickly and is only useful up to around tens of nanometers away from the surface. To help have better control of this position and to understand better this near field phenomenon we use an Interferometric Spatial Phase Imaging (ISPI) technology.

ISPI is based on a set of gratings that can create different fringe patterns that depend on the gap between 2 surfaces (Moon et al., 1999). This tool has the potential of getting gap measurements with a resolution of under 1 nm. It can be used for mask and substrate alignment and gap control. A laser shines on a grating structure, diffracts towards a 2nd surface which reflects back to the grating and refracts a pattern back to the camera. The camera is position very close to the laser source and does not have to be perpendicular to both surfaces. This allows for a measurement control that does not get in the way of a processing source such as a laser or a lamp. In our setup, the laser and the camera are both mounted in the same holder at $\pm 2^\circ$ away from the Littrow angle of approximately 20° . There are different types of gratings that are useful for different ranges and resolutions. There is a coarse ISPI grating that has a resolution of approximately $1\ \mu\text{m}$ and works on gaps of about $30\ \mu\text{m}$ to $100\ \mu\text{m}$. The top half of Figure 2.17 shows the grating, the beam path diffraction diagram and the camera image for the coarse gap setup. The period of the grating is of $1\ \mu\text{m}$, which is the necessary period required to send the 1st order of refraction back to the camera for both back-diffracted and diffracted-reflected beam.

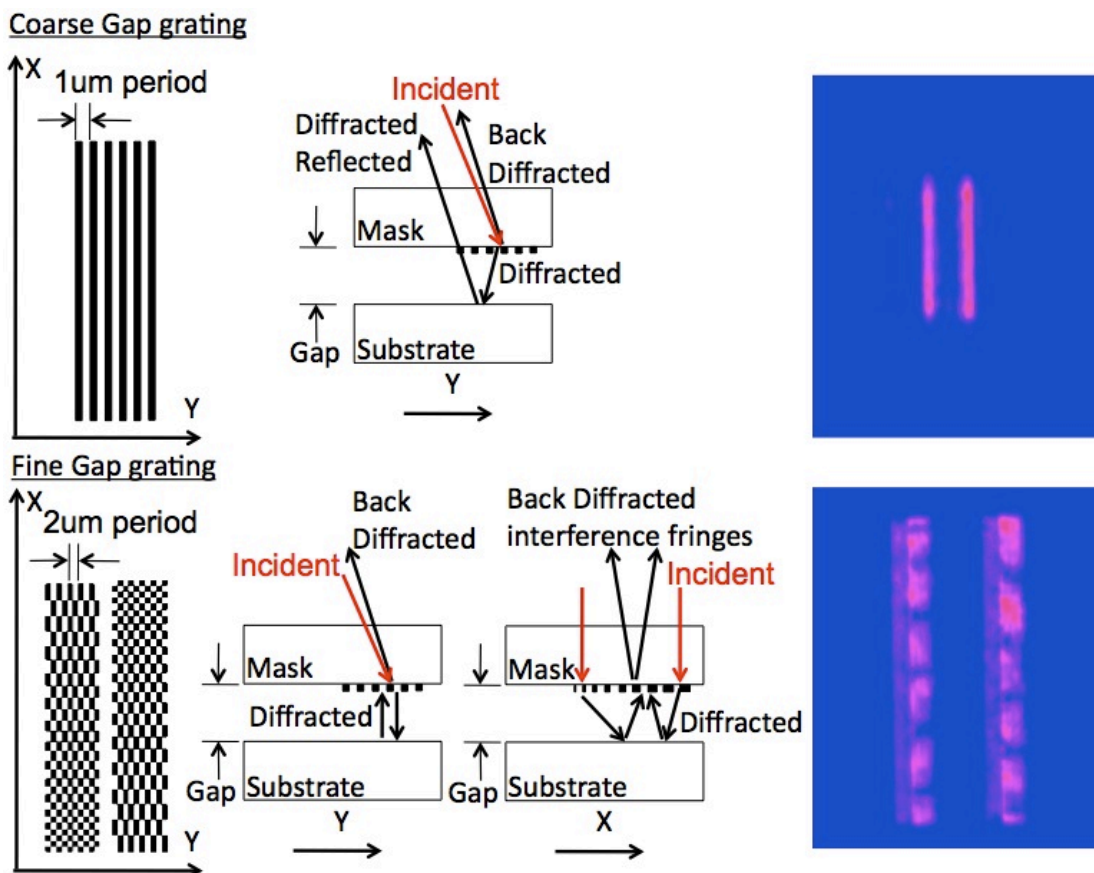


Figure 2.17: Gratings used for ISPI gap measurement. Beam diagrams show how the incident light travels from the laser to the grating, gets diffracted, gets reflected and then refracted back to the camera. The right side shows how both patterns look on the camera.

There is also a fine ISPI grating shown on the lower half of Figure 2.17 that can be designed for different ranges and different resolutions. The period of the checkered grating in the Y direction is of 2 micron. The 1st order diffraction in the YZ plane corresponding to this period goes straight down to the substrate and reflects back up to the same grating. The reflection of the substrate hits the same grating again, is it diffracted again towards the camera. The interference fringes formed at the plane of the camera have different periodicity and phases depending on the distance between the substrate and the mask. An example of this fine ISPI periodical pattern at the camera is shown in the lower right side of Figure 2.17. The special frequency tells us the gap between the surfaces in a greater range but with a poor resolution. When the gap is larger, there are more fringes in the interference image and the frequency calculation

yields a higher number. For fine ISPI there are two sets of fringes formed in the camera. The relative phase of these fringes also changes when the gap changes. This phase gives us a much finer gap measurement resolution. The phase is a number between a 0 and 2π that corresponds to a gap of 120 nm. With the phase information of the fringes we are able to obtain a resolution of less than 1 nm in the gap measurement but it does not contain information about the absolute gap. All different types of measurement are used together to approach both surfaces and then make finer adjustments when we get closer to the near field. The general purpose of using fine ISPI is to try to achieve slight contact between surfaces and from there establish the desired gap between surfaces.

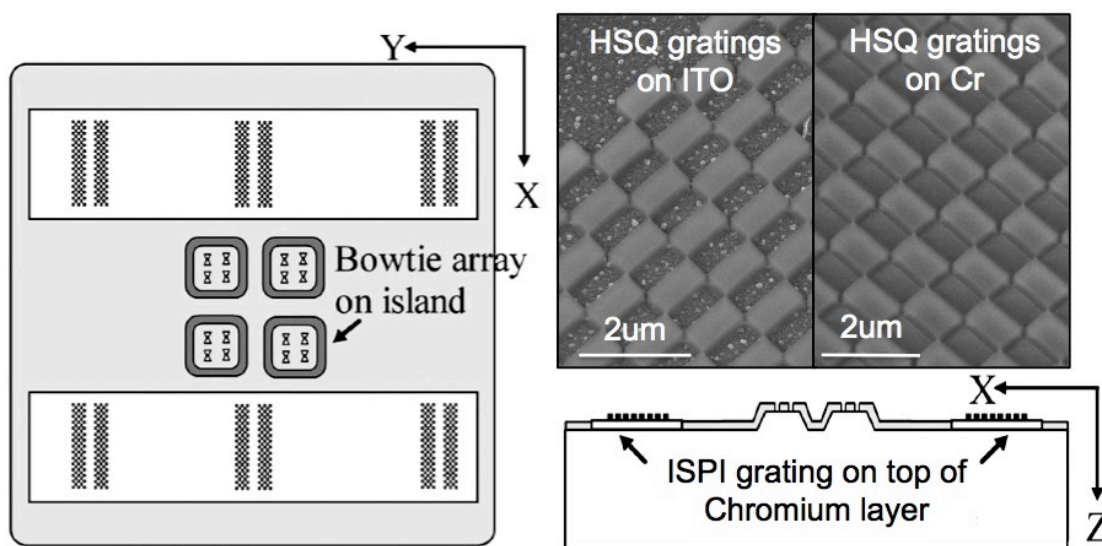


Figure 2.18: ISPI gratings in a lithography mask. The top right shows the difference in surface roughness between creating the phase gratings on top of indium tin oxide and chrome.

Gratings were made with negative resist HSQ. Our HSQ gratings are considered binary phase gratings. It is important that the thickness of the binary phase grating yields a phase difference of half the wavelength. The thickness for a medium with an index of refraction very close to the index of silicon dioxide ($n=1.5$) must be the wavelength of the laser ($t = \lambda = 633$ nm). This is obtained coating the mask at 2000 RPM reaching this speed at 3 seconds and spinning for 45 seconds. The substrate is baked at 120°C for 3 minutes. The sample is exposed with a dose of $1100 \mu\text{C}/\text{cm}^2$ and then developed in TMAH for 45 seconds.

Several sets of grating are used to measure the gap in different locations of the substrate. With a certain grating arrangement we can have control of the gap and the angle between both surfaces. For parallel lithography is important that both surfaces are as parallel as possible. To accommodate for all of the gratings we need to fabricate large windows as shown in Figure 2.18. There has been a maximum of 8 sets of grating but a minimum of 3 is necessary to obtain the angle between both surfaces. Gaps at different locations are measured sequentially since only one gap can be read at a time. The details of this fabrication are described in section 2.4. Originally to have good conductivity for the e-beam lithography and also transparency of the substrate for light propagation we used a layer of ITO. Using the layer of ITO was inconvenient because it required an additional annealing step that was done at a temperature of 550 °C. It was also a very rough layer and had poor adhesion with HSQ resulting in a low yield of good gratings. Eventually a Cr layer of 3 nm was coated. This layer is transparent because its thickness is less than the skin depth of the Cr. The actual thickness of this layer is uncertain because the control of coating 3 nm during an e-beam evaporation process is difficult. It is also not certain how conformal this thin layer is. Very thin coatings are believed to initially take the form of localized islands before they become conformal layers because of grain formation. Nevertheless the coating of this layer provides the adhesion necessary to obtain an almost 100% yield in the grating structures, the conductivity necessary to perform e-beam lithography without localized charging and the transparency necessary to allow for the propagation of the ISPI laser beam.

The shape of the fringes is decoded by comparing them with simulation results base on diffraction optics. In the simulation, a set of fringes is calculated based on adding up the effect of different 1st order diffraction. This calculation represents a relationship between the gap and the shape of the fringes. Both the simulated and the experimentally measured fringes are subjected to a frequency and phase calculation algorithm. Frequency and phase calculation results for the numerical model and for actual experiments are shown in Figure 2.19 (Wen et al., 2013). It is important to note that the frequency theoretically should increase linearly as the gap increase but it increases experimentally with an oscillatory behavior. We believe that this oscillation is

an effect of a fabry-Perot interference on the brightness of the fringes. This change in brightness might affect the reading of the position of the fringe peaks. Still with this oscillatory behavior the system can be calibrated to obtain gap measurements. The calibration of the fine ISPI measurement is made by comparing the phase reading to the feedback reading from the piezo stage. We take note of what is the piezo height distance that it takes to obtain 1 phase shift. Once calibrated it can be used to obtain the distance above contact between the two surfaces.

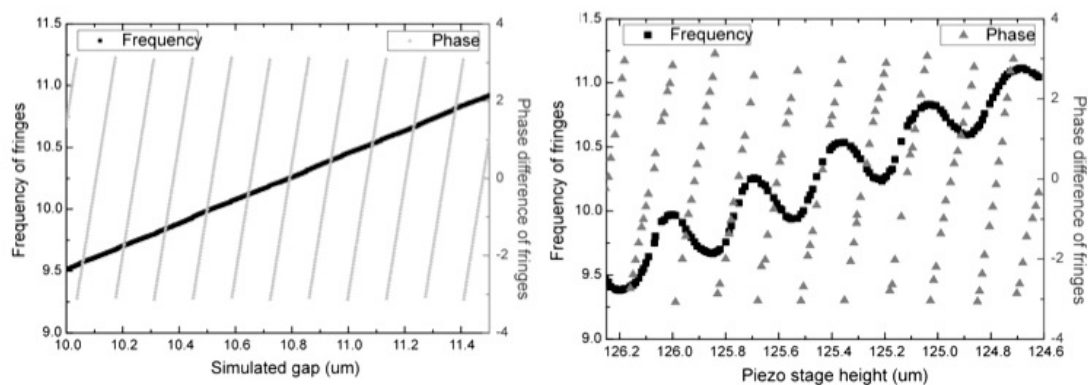


Figure 2.19: Left graph shows the simulated frequency and phase measurements as a function of the gap. Right graph shows the actual measurements as a function of a range in the piezo stage height; Reprinted with permission from [Wen et al., 2013] © [2013], American Vacuum Society.

2.4 Parallel Nanolithography Using a Large Array of Bowtie Apertures

Parallel nanolithography can be achieved by shining the same beam to an array of bowtie apertures. All of the apertures will produce their own confine near field spot at their exits. It has been proven that each spot is capable of producing lithographic lines of widths as small as 50 nm (Uppuluri et al., 2010). We were interested in performing parallel lithography implementing ISPI gap control to obtain more lines. Like described in section 2.2.1 we milled an array of 32 X 32 bowtie apertures on top of a chrome-coated island. This array was made with a current of 1 pA in an effort to make aperture ridge gaps smaller and produce smaller lines during the lithography. As described in section 2.2.1 our array was milled using a code with vectorial commands to define the pattern geometry and beam deflection commands that would control the position of the

milled apertures. The presence of the island minimizes the amount of particles that will get in between the mask and substrate surfaces. The procedure to fabricate the mask with the ISPI gratings is described in Table 2-4. The substrate used to fabricate the mask is made of quartz and has a surface that is polished to an optically flat standard. A substrate is considered optically flat when the variation in height of the entire surface is approximately $1/20$ of optical wavelengths. This substrate was cleaned with a piranha mixture consisting of a 1:1 volume ratio of sulfuric acid and hydrogen peroxide solution. After cleaning, the substrate was prebaked dry for 1 hour at 1100°C . To create the island we first patterned a square (step 1 of Table 2-4) using optical lithography on a AZ1518 photo resist layer. For this lithography process we first coated a thin layer of the adhesion promoter hexamethyldisilzane (HMDS) for 45 seconds at 4500 RPM. The adhesion promoter was coated to minimize lateral etch in one of the following steps. After coating the promoter we coated the layer of AZ1518 for 45 seconds at 2500 RPM. A soft bake was done at 100°C for 5 minutes.

Table 2-4: Steps of mask fabrication process.

#	NAME	DESCRIPTION	SCHEMATIC
1	Patterning island mask	After cleaning prebaking and coating adhesion promoter, coat PR AZ1518 at 2500 RPM for 45 seconds, soft bake at 100°C for 5 minutes. Expose for 17 seconds at 10 W/cm^2 . Develop in AZ developer for 9 seconds and then hard bake at 120 for 5 minutes.	<p>AZ 1518 patterned island mask</p> <p>Quartz Substrate</p>
2	Island Etch and thin conductive layer coating	BOE etch for 114 minutes to obtain a $10\text{ }\mu\text{m}$ height island. Strip the photo resist with solvent and piranha cleaning and then coat a thin layer of 3 nm of Cr.	<p>$10\text{ }\mu\text{m}$ height island</p> <p>3 nm Cr</p> <p>Quartz Substrate</p>

Table 2-4: Continued.

#	NAME	DESCRIPTION	SCHEMATIC
3	Windows patterning	S1805 coated at 4500 RPM for 45 seconds, baked for 3 mins at 90°C, and exposed for 5 sec at 10m W/cm ² . Developed with AZ developer to water mix at 1:2 for 20 seconds. A drop is applied to the island to make sure that all the resist is developed away. A line is applied on the edges. Rinse with DI water.	
4	Cr mask coating	Coat 70 nm of e-beam evaporated Cr. Lift-off with acetone for 10 minutes and ultrasonic agitation for 10 seconds.	
5	ISPI phase grating	Coat of Fox 15 HSQ at 2000 RPM reaching that speed in 3 seconds. Exposed with a dose of 1100 $\mu\text{C}/\text{cm}^2$. Developed in TMAH for 45 seconds.	
6	Milling of the bowtie apertures	Focused Ion beam milling. Marks are made using large 2 nA or 5 nA current and apertures are made with small 1 pA or 10 pA.	

The island mask square pattern was developed after submerging the sample in a 1:3 solution of AZ developer and water for 9 seconds. The mask was hardened with a post bake done at 120°C. After the island square mask was made, the substrate was etched 10 μm deep in a BOE solution. The quartz etch rate of this solution of 0.088 $\mu\text{m}/\text{min}$. The whole etch time is approximately 114 minutes. We used a magnetic stirrer to help obtaining a uniform etch. We interrupted the etching every 15 minutes to change the

direction of the flow with respect to the substrate to promote uniformity. The substrate was checked under a microscope every 30 minutes to ensure that the lateral-etch rate was not too high. After etching we striped the remaining photo resist with a simple acetone cleaning for minutes. To address quality control, we measure the island height and checked the top of the island to make sure there were no undesired particles stuck to it. After having a clear island substrate we proceeded to coat a 3 nm layer of Cr for the reasons discussed in section 2.3. Even when is not expected to produce a continuous layer, this Cr layer helps promoting adhesion between the HSQ layer and the quartz substrate and also offers good substrate conductivity for the e-beam lithography process. The adhesion promoting capability of Cr will be discussed with further detail in section 3.1.3. The next main step was to produce windows for the ISPI grating pattern. This involves the patterning of two large rectangles of 10mm by 1 mm separated by 5 mm with the island in the middle of them. To start we must coat a photo resist layer around the entire substrate.

When coating a substrate there will always be a thicker layer at the edges of the substrate. Base on the same principle we can expect the small island patterned in the center of the substrate to have a thicker layer. These areas with thicker layer will require higher exposure doses or longer developing times to be completely developed away. For this reason we opted to use a thinner photoresist. S1805 photo resist was coated for 45 seconds at 4500 RPM and soft baked for 3 minutes at 90°C. We developed the windows using AZ developer and water solution at a volume ratio of 1:3 for 20 seconds. To develop the thicker areas mentioned before we applied a drop of developer on top of the island and a line of developer on the edges of the substrate. It is important to not have undeveloped photo resist regions on the edge of the island because a good electrical grounding connection will be needed during the FIB milling of the apertures. A layer of 70 nm of Cr was coated using e-beam evaporation followed by a lift-off made by soaking the sample in acetone for 5 minutes and agitating with ultrasonic vibration for 5 seconds. This lift-off revealed the pattern of the windows where the ISPI grating would be fabricated. HSQ resist was coated for 45 seconds at 3000 RPM with a ramp time of 3 seconds. This coating recipe yielded approximately a 633 nm thick layer of HSQ. The

resist was soft baked at 120°C for 3 minutes. The gratings were patterned as specified in section 2.3. Developing of the HSQ was done in Tetramethylammonium hydroxide for 45 seconds. At this point the mask was ready for FIB milling as described in section 2.2.1.

To use the finished mask for parallel lithography we mounted it in a piezo electric stage like it is shown in Figure 2.20. This piezo stage can be rotated with respect to x and y-axis which allows controlling the angle between the mask and the substrate. We coated another optically flat substrate with S1805 at 4500 RPM for 45 seconds. On this substrate is where we intend to perform the near field parallel lithography. This substrate was positioned on top of a different piezo stage used for gap control (Z direction) and scanning (X and Y direction). Figure 2.20 shows the diagram of the lithography station. Besides the ISPI laser and the exposure UV laser (355 nm DSSP) there is a He-Ne laser that shines the substrate and mask from below the setup. The He-Ne laser is use for coarse alignment between the photoresist coated and mask substrates. The coarse alignment laser reflects from the photo resist and aperture mask surfaces. The reflection from both surfaces is joined and sent to a camera creating an interference image from which we can see the angle between the surfaces. The amount of fringes in the image is proportional to the angle between them. During coarse alignment we intend to obtain an image without fringes. The inset in Figure 2.20 shows an example of images that were taken using the coarse alignment laser and corresponding numerical simulations that relate the amount of fringes and the angle between substrate. This coarse alignment was the 1st step in our parallel lithography process. After coarse alignment we measured the height at the different location of the ISPI marks and made sure that the height difference between them was around 6 nm. A height difference of 6 nm corresponds to an angle 0.03 mRad.

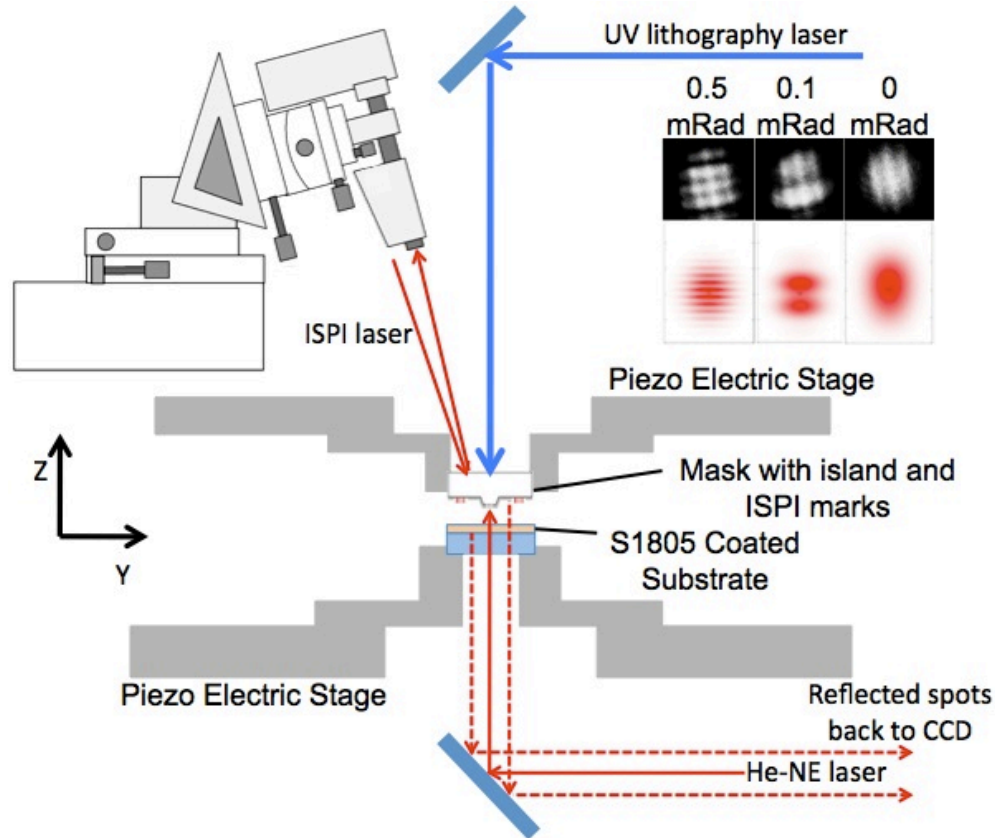


Figure 2.20: Diagram of the bowtie aperture lithography station; Reprinted with permission from [Wen et al., 2013] © [2013], American Vacuum Society. Inset shows simulated and photographed interference patterns that gives us the measurement of coarse alignment to obtain parallel surfaces (Uppuluri et al., 2010).

After performing fine alignment we brought the 2 surfaces into contact. Coarse ISPI helped us to identify when there was a large distance between the mask and the photo resist substrate. Figure 2.21 shows a graph of the gap measurement taken with the ISPI grating VS the stage motion. As expected as the piezo height increases the gap between the surfaces decreases at a constant rate until a certain point. At this point even when the piezo feedback is showing that the height of the stage is increasing, the ISPI grating aren't showing as much gap change. We can be certain that this happens because both surfaces have come into contact. When we study the graph with more detail, we are able to identify when does this contact occurs with nanometer resolution.

With a good adjustment of power of the processing lithography beam and gap control we are able to obtain lines as small as $\sim 22 \pm 5$ nm (Wen et al., 2014). This is 1/15

of the 355 nm wavelength. Figure 2.21 shows an array of 5X5 patterns that contain the letters “bnc” as well as a zoom in afm image of one of them. The inset at the lower left shows a line scan of the section shown in the lower right inset. It shows a full width at half maximum of 22 nm, which seems to be consistent around the array.

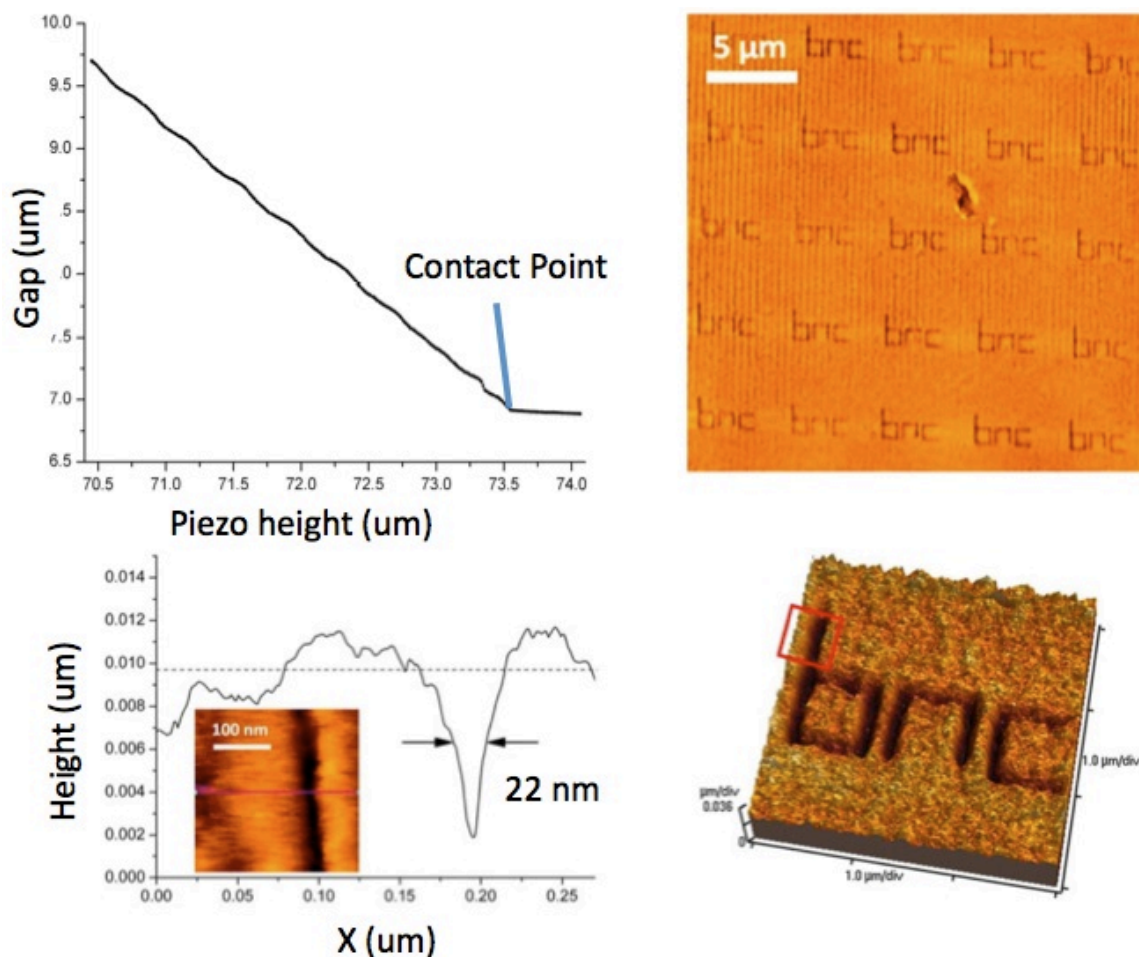


Figure 2.21: Using ISPI for gap control and results of nano-scale aperture lithography. Top left shows the ISPI gap measurement VS the motion of the piezo stage. Top right shows a scan of 5 X 5 bowties. Bottom right shows a zoom in at one “bnc” pattern, which is then zoomed in at the red square, which is shown with a line profile at the left bottom graph (Wen et al., 2014) With permission from Springer.

2.5 Summary

We have shown that bowtie apertures are capable of creating sub diffraction limit spots that can be used in applications such as parallel lithography and HAMR. The current method that our group uses to fabricate these apertures (FIB) allows us to obtain very small aperture but it creates a curvature in the edges around the aperture due to the limit of the ion beam resolution. Simulations have been made showing that this curvature increases the effective gap and limits the confinement wanted. Different fabrication techniques have been attempted in order to eliminate this edge curvature.

Etching a sacrificial layer could help us eliminate the part of the milling that contains the unwanted curvature leaving a straighter edge. The problem with using sacrificial layers is that their etch rate is affected by gallium ion implantation and they become difficult to remove leaving behind unwanted material around the aperture. Milling an aperture in a membrane and reversing the membrane allows us to obtain apertures that have sharper features and potentially better confinement. We attempted to transfer thin films on top of substrates to perform parallel lithography using these sharper inverted bowtie apertures. The process was one with many steps and we could never obtain a clean process that could allow us to achieve good results. We have also attempted to create better apertures by using e-beam lithography. We tried different schemes based on etching or lift-off with different types of resist layers. Using e-beam lithography was not effective because we were not able to control the shape and dimension of the gaps for these small patterns.

We did however optimized aperture masks to create smaller lithography lines. We implemented the use of ISPI gratings to obtain a better gap control between the mask and a substrate to fine tune (with nanometer resolution) the position of the photoresist with respect to the nearfield around the aperture. By controlling the gap in several locations of the mask we were able to make both surfaces as parallel as possible. This allowed us to position large arrays of bowties to certain consistent and determined gaps. Using ISPI we were able to perform parallel lithography using an array of 32 X 32 apertures to pattern lines with ~22 nm widths.

CHAPTER 3. ZONE PLATES FOR FABRICATION OF SILICON NANOWIRES

Zone Plates (ZP) can provide an excellent source of concentrated light for heating purposes. A confined heated spot could be used as a fabrication tool for applications such as the synthesis of silicon nanowires. When we increase the temperature of silane gas to a decomposition temperature of its hydrogen bonds we can obtain a solid form of silicon. When doping molecules are present in the gas mixture we can also obtain a solid form of doped silicon. This thesis chapter discusses how we take advantage of Fresnel diffraction ZP to increase the temperature and fabricate silicon nanowires.

3.1 Definition of Zone Plate

A ZP is a collection of concentric rings that is capable of focusing light by means of diffraction. The concentric rings of a basic ZP allow the pass of light in certain areas called zones. The small periodicity of these rings acts similar to a grating and is capable of achieving large diffractive angles when the size of the grating is very small. Because of their large diffractive angle, they are capable of focusing light into dimensions very close to the diffraction limit. Constructive interference of the diffracted rays coming from different zones makes possible the concentration of light at the focal point. The zones in the ZP can be considered as amplitude gratings or phase gratings. In amplitude gratings, zones are either transparent or dark and hence they modulate the amplitude of the transmitted light. In a phase grating, the zones rather than blocking the light, provide for a medium of a finite index of refraction that creates a shift in the phase of the waves relative to zone regions with different indexes of refraction. If designed and fabricated properly, a phase grating can input almost twice the amount of light energy into the same spot when compared to an amplitude grating. One of the main advantages of zone plates over lenses based on refraction or reflection is that they can be fabricated much easier in

a nanotechnology fabrication environment. Applications of ZP structures can include any application that requires the use of focused light to heat or expose lithographically a material.

3.2 Experimental Setup for Nanowire Fabrication

Our group has previously used ZP for fabricating and optimizing silicon nanowires (Nam et al. 2013). Some of these nanowires have been doped and used as field effect transistor sensors with high sensitivity to pH. By controlling certain parameters in the experimental setup we can change the roughness of the surface, increase the surface area, and as a consequence increase their pH sensitivity.

In this section we describe the laser setup and sample substrate used for the synthesis of nanowires using ZP. We particularly concentrate the light into a scanned substrate that is capable of absorbing the light and producing an intense small spot of heat. It is always considered that the spot size of the ZP focused light will be proportional to the wavelength. Hence it is convenient to use the smallest possible wavelength to fabricate a smaller nanowire. The available wavelength is of 800 nm but it would be desirable to convert this wavelength into its half by using special optics. For this purpose, light is focused through a lens onto a barium borate crystal. When the crystal receives light intense enough, it induces a 2nd harmonic generation, which doubles the frequency. The beam comes out with a certain polarization determined by the orientation of the crystal.

Several laser parameters were studied in order to optimize the heating process. Previously tested lasers were continuous wave laser, nanosecond/microseconds pulsed laser, and femtosecond laser. It was observed that continuous laser could deliver the power necessary to obtain high enough temperatures but the continuous heat generation would allow for a spread of a high temperature profile that would subsequently increase the size of the deposited nanowire. Something similar would happen to the nanosecond lasers. The advantage of the femtosecond laser is that it would allow for a high temperature enough to obtain nanowire growth, but in between pulses it would allow for

enough time to dissipate the heat. The combination of obtaining localized high temperature followed by heat dissipation time, allowed for the confinement of synthesized silicon volume. High temperatures would not be achieved if heat dissipation would occur too rapidly. This is why the substrate material properties are very important variables in the nanowire growth problem.

Several different substrates were tried by our group in order to obtain the smallest possible nanowires. The different substrates were made of different combinations of layer arrangements using silicon and silicon dioxide. The material properties of thermal diffusivity and light absorption were very important in our design. High light-absorption is desired to concentrate the heat in a small location as close to the surface as possible. Silicon is our absorptive material of choice, while SiO₂ will be used as the isolation material to help with heat confinement. The dependence on absorption to the wavelength of the incident light is a very important factor to take into consideration. At 780 nm wavelength, silicon has a penetration depth of 5.2 μm while at 390 nm it has a depth of 26 nm (Bauerle, 1996). Another important reason for doubling the frequency of the incident light is to maintain the maximum amount of absorption close to the surface of the substrate. We noted after trying several different combinations of materials that the narrowest lines occurred in 1 mm quartz substrates with a layer of 200 nm of polysilicon under a layer of 200 of silicon dioxide. In order to fabricate this arrangement we deposited 350 nm of low pressure chemical vapor deposition (LPCVD) silicon with an amorphous crystal structure. This coated quartz would be subjected to a temperature of 1100°C for 130 minutes to grow an oxide layer of 200 nm. This process would also anneal the rest 150 nm of amorphous silicon into 200 nm of polysilicon. Figure 3.1 shows the substrate layer arrangement that was considered the most optimal.

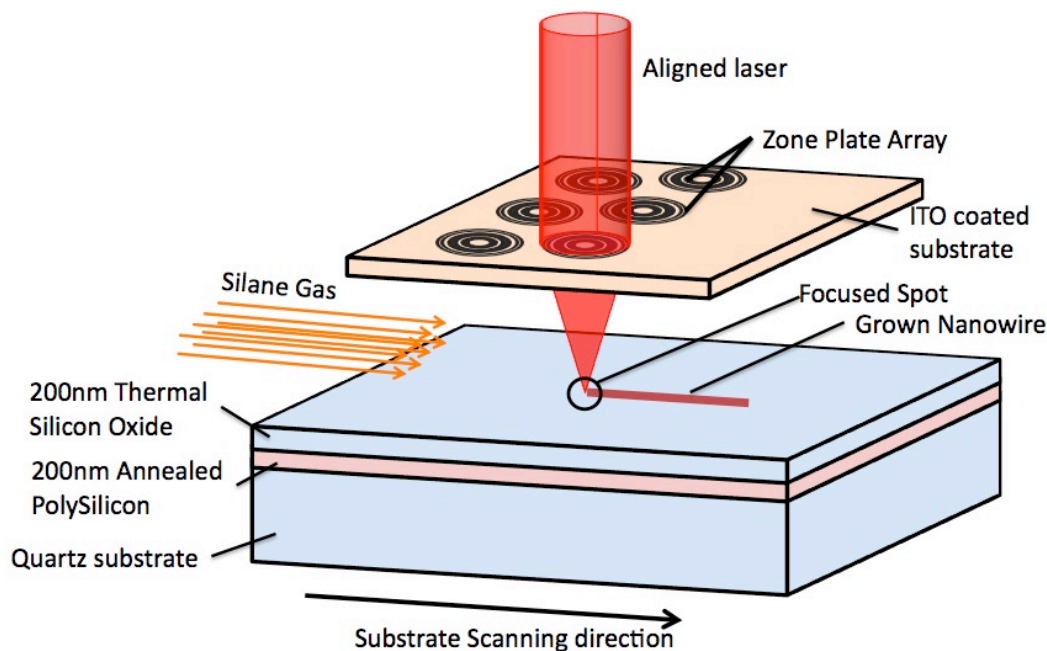


Figure 3.1: Setup up for ZP assisted silicon nanowire growth.

Figure 3.1 also shows a schematic for the nanowire growth. Silane gas is input from one side of the chamber into a region where there are zone plates focusing light into the substrate. The focal point of the zone plate must coincide as well as possible with the absorbing layer of silicon to concentrate heat at the gas and solid boundary. The hydrogen bonds of the silane break in the regions where the temperature of the gas reaches a decomposition threshold. This decomposition yields silicon solidification in the heated areas. If the substrate is scanned, we obtain a nanowire in the direction of the scanning as shown in Figure 3.1. When a dopant gas is flown at the same time as the silane, we obtain a doped form of the silicon. Diborane B_2H_6 is introduced to provide boron doping or p-type doping while phosphine PH_3 is introduced to provide phosphorous doping or n-type doping. To have higher intensity at the substrate surface, light is focused into a size close to the $300\ \mu m$ diameter of the ZP and shined on top of the ZP. To obtain an efficient focusing, the diffractive design of the ZP must be taken into consideration.

3.3 Designing a Zone Plate

There are certain parameters that contribute to the efficiency of a ZP. The most important ones are the width and position of the zones. The width of a zone will determine the grating period and thus the diffraction angle, while the radius of the zone will determine for a given periodicity where the maximum field spots along the axis of the lens are. A basic amplitude ZP should have the radius of the zones such that the exit of these is at a distance that creates constructive interference in the focal point. For this to happen we make sure that the radius of the zones are fixed with the relationships shown in Figure 3.2. By looking at the geometrical relationship of the optical paths and considering that the focus f is much larger than the wavelength we arrive at the relationship $r_n = \sqrt{n\lambda f}$. Where n is the number of the zone, λ the wavelength of the light source, and f is the focal length of the lens.

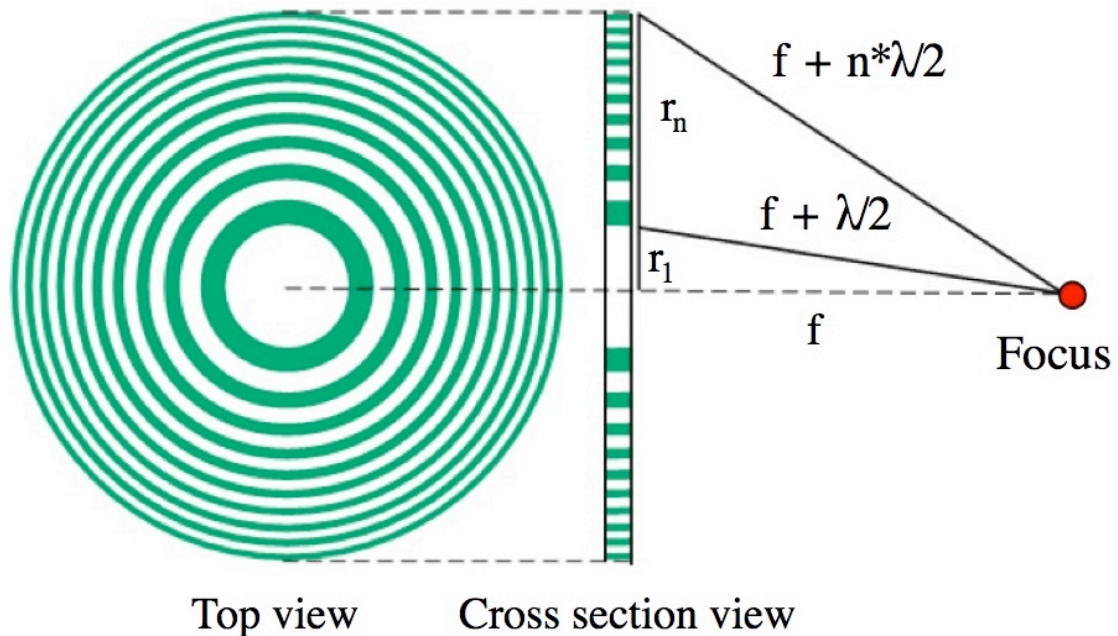


Figure 3.2: Optical path of zones inside a ZP.

A ZP is called an amplitude ZP when it contains opaque zones. Such a ZP has a maximum efficiency of approximately 10%. If these opaque zones are replaced by phase shifting material with an index of refraction, we obtain a level 2 or binary ZP. Level 2 indicates that there are 2 different phases coming out of the exit plane of the ZP. Having

a region with no thickness and a region with a certain thickness of the phase-shifting material creates the 2 different phases. The phase shift can be between 0 to π depending on the thickness of this material. The maximum efficiency of such a ZP is approximately 40%. Higher levels could be obtained if the opaque zones are replaced with a material that has more than 1 thickness. We would need a fabrication method that would yield different thickness in certain specified areas. Level 3 or higher ZPs could obtain higher theoretical efficiencies all the way up to 100% but fabricating them would constitute a very difficult problem. Our group did not consider fabricating level 3 or higher ZP and thus will not be discussed here.

To design a phase ZP we need to compare the optical paths of two mediums with same thickness and different index of refraction. For a given index of refraction and incident wavelength we need to obtain a thickness given by the Equation (3.1) that will yield a phase change of half the wavelength between the two mediums (air and phase retarding medium). In a level 2 ZP, this thickness yields the highest efficiency. When the index of refraction is exactly 1.5, which is very close to glass, the optimal thickness is exactly the wavelength itself.

$$t = \frac{\lambda}{2(n_2 - n_1)} \quad (3.1)$$

Hydrogen silsesquioxane (HSQ) is an excellent transparent photo resist that will allow us to pattern the thin zones in the outer regions of the ZP. After developing and hard baking, HSQ is very similar to silicon dioxide that has an index of refraction of approximately 1.5. Our ZPs had a thickness of 400 nm because they were designed for 400 nm wavelength incident light and are made with HSQ.

3.4 Fabricating a Zone Plate

Fabrication of a ZP includes a small number of steps that needs to be fined tuned in order to make them more efficient. The 1st step is to increase the conductivity of the substrate so we are able to perform e-beam lithography on top of a transparent quartz

substrate. Originally we tried coating indium tin oxide (ITO) on top of quartz substrate. The coated ITO layer needs to be baked at 550 °C for 2 hours in order to convert it from an opaque into a transparent layer. This whole process results in an ITO layer with a very high roughness. Ultimately we opted to buy commercially available ITO coated quartz substrates from Prazisions Glas & Optik (a German glass optics manufacturing company). The substrate is a piece of quartz of 12.6 mm X 12.6 mm X 1 mm. These were used because they had smoother surfaces than the ones fabricated in our facilities. We used an ITO film that was specified to have a sheet resistance of 20 ± 5 Ohm/sq. Assuming a resistivity of 7.5×10^{-4} Ohms-cm (Farhan et al. 2013), we can estimate that the thickness of the ITO layer is approximately 375 nm.

The 2nd step is made to increase the adhesion between the HSQ resist and the ITO layer. The fabrication yield of ZP structures is highly dependent on this adhesion. This lack of adhesion is evident when developing the sample after e-beam exposure. Without aid of any kind, only about 25% of the structures would still be standing even when using a gentle flow of water to rinse the developer. Wi et al. from the Seoul national University have reported the used of a thin amorphous silicon layer to improve the adhesion between HSQ and a multilayer of cobalt and palladium (Wi et al. 2006). We added a thin adhesion layer of 3 nm of amorphous silicon to our ITO coated substrate using e-beam evaporation. We experienced that the adhesion improved drastically even when it is believed that for a nominal layer of 3 nm there might not be a conformal layer. It was important to make sure that the silicon thin layer was as thin as possible so there is minimal absorption of laser light into it. Because of this Si layer, the yield improved to 100% except for instances in which there was contamination. By performing cleaning of the substrate with ultrasonic agitation after the adhesion layer was coated, we obtained a fabricated region with almost no contamination. We are not sure which adhesion mechanism came into play in this high yield and why the adhesion improved.

The 3rd step is to coat and bake the HSQ layer. The thickness of the ZP structure is determined by the thickness of the HSQ coating in the center of the substrate. This can depend on a lot of variables including the size of the substrate, the coating acceleration

and speed, the type of HSQ, and the post baking process. The size of the substrate is fixed to the design of the nanowire growth silicon substrate holder. The type of HSQ used for the fabrication is FOX-15 manufactured by Dow Corning. This particular type of resist is dissolved into Methyl Isobutyl Ketone (MIBK) with a certain dilution ratio that when coated will yield a thickness within the desired range. The manufacturer does not disclose the specific dilution ratio but a range. It states that the solvent is between 70 to 90 %w/w MIBK. After several coating iterations we found that coating with a speed of 3000 RPM, accelerated from rest in 3 seconds, spun for 45 s, and post baked at 180°C for 3 minutes yields the required thickness of 400 nm.

The 4th step is to expose, develop, and bake the sample. The designed ZP for our process has a diameter of 300 μm and a number of 548 zones which means that there are approximately 274 rings exposed. The smallest dimension for the exposure is the width of the outer rings (~ 200 nm). The entire ZP was fabricated using a dose of 900 $\mu\text{C}/\text{cm}^2$. On earlier test, this dose seemed to be adequate to achieve the dimensions of most of the zone except for the outer zones. The inner rings have a higher effective dose because of the proximity effect caused by exposing the surrounding areas. The outer zones seemed to be under exposed and hence they would be over developed. It would be difficult for the inner rings to obtain the necessary dose to achieve the proper width by merely adjusting the dose. In order to fix this we created an additional outer 10 μm wide ring (Figure 3.3(a)). This width is large and close enough to increase the effective dose on the region of the outer rings of the zone plates. This outer ring starts at a radius that is 2.5 μm away from the outer radius of the last ring exposed as shown in Figure 3.3(d). The dose used for the exposure of this outer ring is also 900 $\mu\text{C}/\text{cm}^2$. After this modification, all of the rings were successfully fabricated with the designed width. Figure 3.3(c) shows an example in which there was overdose resulting in under development. The under developed region will appear to have a darker shade than the well developed. We developed the patterns by submerging the substrate in tetramethylammonium hydroxide (TMAH) for 45 seconds. After development, the sample was post baked at 550° for 2 hours. Results of the critical dimension region are shown in Figure 3.3 (b).

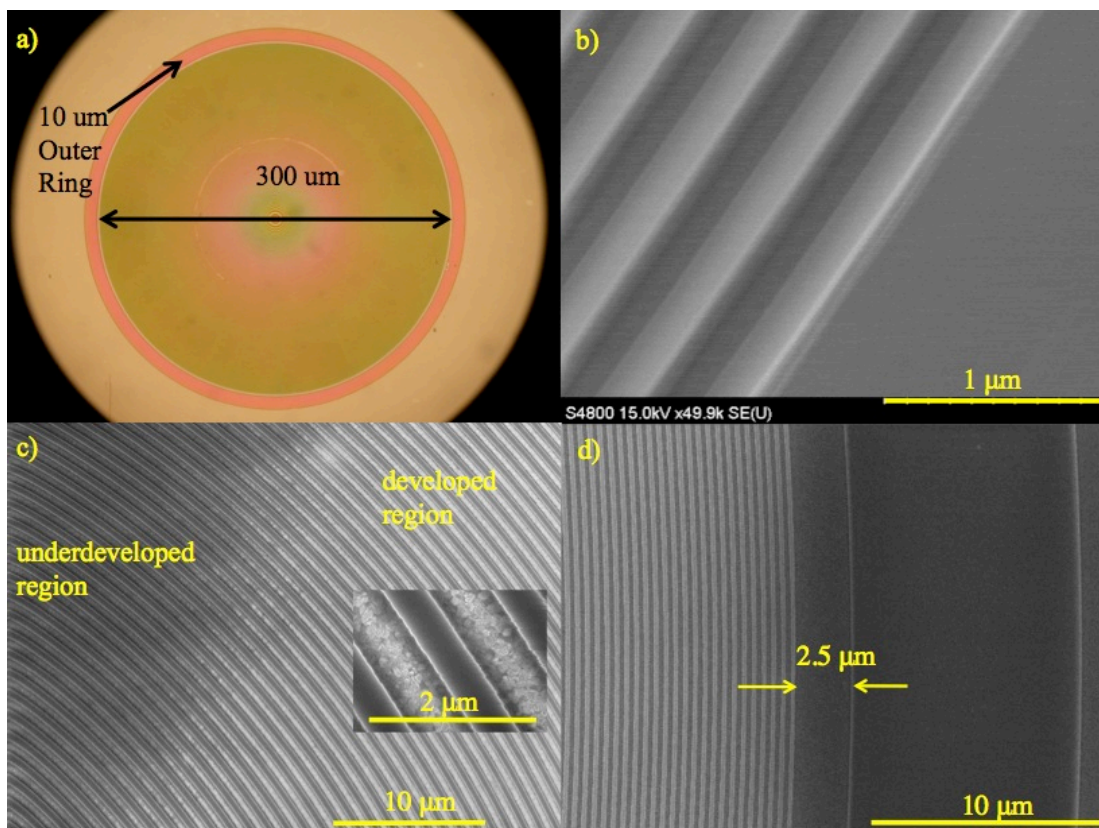


Figure 3.3: Images of fabricated ZPs. a) Microscope view of the entire ZP showing the outer rings used to compensate for proximity effect correction. b) Scanning electron microscope tilted image of the outer zones of the ZP. c) Image of an overdosed zoneplate that resulted in partial underdevelopment. d) Zoom in of the outer ring used to even out the proximity effects.

3.5 Thermal Decomposition of Silane

A brief description of the thermal decomposition of silane follows in order to complement the numerical studies. A 1st order homogeneous reaction was studied to obtain decompositions between temperatures ranging from 380°C to 490°C for a significant pressure range (Hogness, 1936). Our group made a rough estimation of this decomposition extrapolating temperatures based on the laser power required to achieve ablation of the oxide layer. This ablation was considered to be an indication of melting which occurs for oxide at a temperature of 1610°C. The minimum power for ablation of oxide in a setup was of 30mW. In the same setup the decomposition of silane occurred at a power ranging from 5mW to 12 mW. Assuming a linear relationship between power

and temperature we can roughly estimate that the decomposition is achieved when the substrate surface achieves a temperature ranging from 291 K to 660 K.

3.6 Thermal Simulation of Heated Substrate Using ZP for Nanowire Growth

We built a finite element model in Ansys to analyze the temperature of a spot in the substrate when it is shined with a small focused laser. The entire model was constructed inside a larger reservoir of 1mm³. This volume is large enough to simulate an infinite reservoir for which the temperatures far from a heat generation source will not change from the initial values. The materials selected for our model were the ones that yielded the best experimental results, as discussed in a previous section of this chapter. The material stack was a substrate of SiO₂ with a layer of 200 nm of silicon on top and a 200 nm SiO₂ at the top of the model. Symmetry allows us to cut the number of elements by half. These models simulate the scan of a heat generation spot by reassigning the heat generation terms to new nodes on every single time step. The axis delimited by scan would be used as the symmetry axis. Constraining the heat transfer in the direction normal to the symmetric surface to 0 is used to ensure symmetry. To model the heat generation input, we calculated the intensity distribution of a Gaussian beam on the XY surface of the model and then exponentially attenuate it based on the absorptiveness of the material. A peak Intensity I_0 is defined based on the laser parameters and then its value is input in the Equation (3.2).

$$q = \alpha I_0 e^{-\alpha z} e^{-\frac{2(x-x_0)^2 - 2(y-y_0)^2}{w_0^2}} \quad (3.2)$$

In this equation, z is the depth coordinate, w_0 is the beam spot size created by the ZP, x and y are the lateral coordinates, x_0 and y_0 are the center coordinates of the beam, and α is the absorption coefficient based on the material. The center coordinates of the beam are updated for each time step to simulate the scanning of the beam. We have assumed for several cases that the top oxide layer actually is capable of absorbing some of the light. We have defined both layers of SiO₂ and Si to absorb with different absorption coefficients. By performing an energy balance we can see that the output

intensity of the top oxide layer becomes the input intensity for the silicon layer. The input intensity was calculated based on an average power measurement of the laser source of 5 mW. This power was the experimental lowest power that would obtain nanowire growth. The intensity corresponds to one of a pulsed laser compressed to 50 femtoseconds. For the laser used, when the spot size w_0 was of 230 μm , the intensity is estimated to be $3.8 \times 10^{10} \text{ W/m}^2$.

The simulations were run with different values of absorptivity α . Silicon absorptivity was the highest which was $1.213 \times 10^7 \text{ m}^{-1}$. This material property was kept constant throughout the entire set of simulations. For silicon dioxide we started with a given literature value of $2.594 \times 10^3 \text{ m}^{-1}$ but this value did not make us obtain the high temperature we expected at the top surface of the substrate. Taking into consideration the potential nonlinearity of the dielectric constant under intense fields, we tried increasing the α_{oxide} value to obtain the expected temperature. Figure 3.4 shows the temperature results corresponding to several chosen α_{oxide} presented in each row. All plot contours are normalized to the maximum temperature of each model. Each column in the figure corresponds to a certain time within a single pulse. The 1st column shows the results at 50 fs, which is the time in which the heat generation condition is active. Right after the 50 fs the heat generation terms are equal to zero to allow for heat dissipation to take place. 2nd and 3rd column shows how much of the heat have dissipated after 200 ps and 13 ns respectively.

We are interested in studying the temperature of the substrate at the area in contact with the flowing silane. Figure 3.5 shows the time history of the maximum temperature at the top of the substrate using the same absorption values shown in Figure 3.4. Even when there might be a maximum temperature at the top of the absorbing silicon layer, it is at the top of the substrate that the silane decomposition takes place.

The processing laser has a pulse repetition rate of 80MHz. This frequency corresponds to a time of 13 ns between pulses. Every 13 ns we activated the heating for another time step that lasted 50 fs. The entire time of the model consist of 5 pulses, time at which the maximum temperatures are close to reaching equilibrium. Within 5 pulses

there was already a tendency for the values to reach a plateau. When we used an α_{oxide} value of $2.594 \times 10^6 \text{ m}^{-1}$ is when we obtained the temperatures closer to the value we expected.

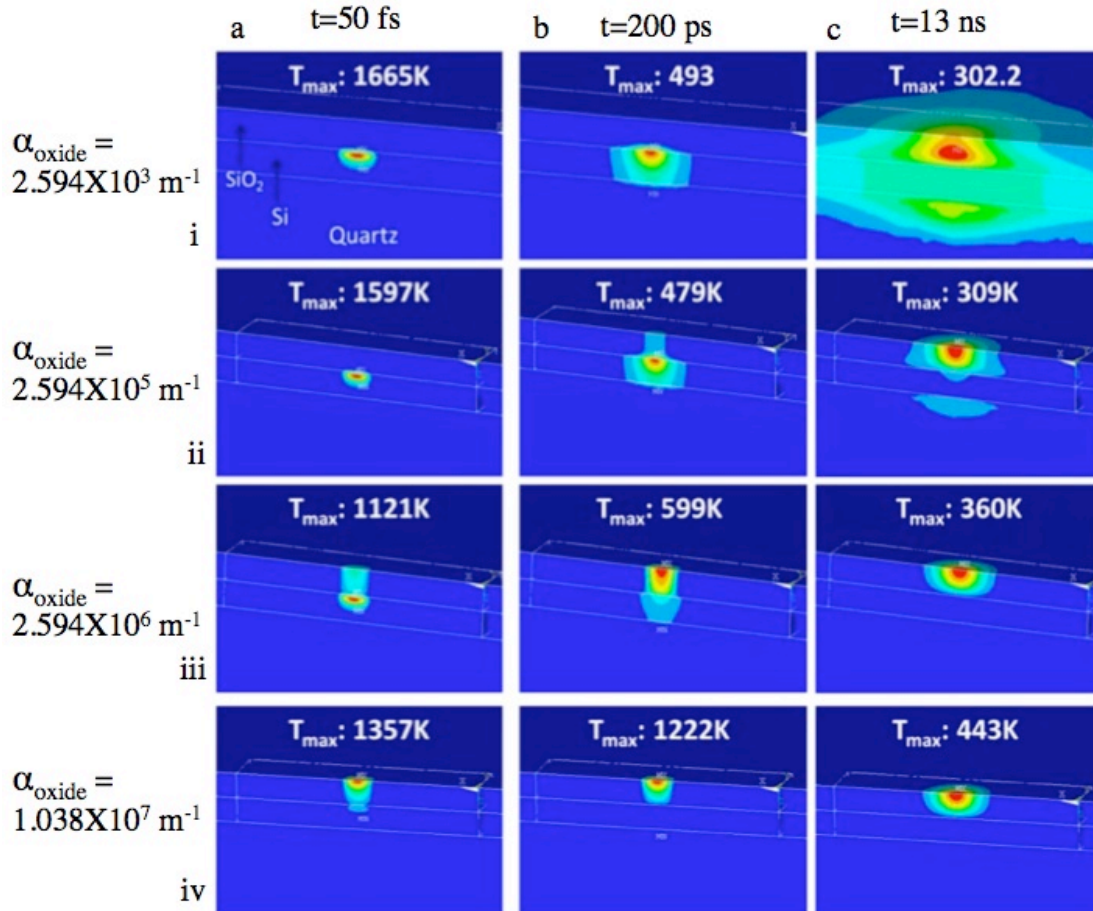


Figure 3.4: Heat transfer simulation of nanowire growth substrate under the influence of ZP generated focused hot spots. Columns show different times: a) $t = 50 \text{ fs}$, b) $t = 200 \text{ ps}$, and c) $t = 13 \text{ ns}$. Rows show results for different absorption coefficients: i) $\alpha_{\text{oxide}} = 2.594 \times 10^3 \text{ m}^{-1}$, ii) $\alpha_{\text{oxide}} = 2.594 \times 10^5 \text{ m}^{-1}$, iii) $\alpha_{\text{oxide}} = 2.594 \times 10^6 \text{ m}^{-1}$, iv) $\alpha_{\text{oxide}} = 1.038 \times 10^7 \text{ m}^{-1}$.

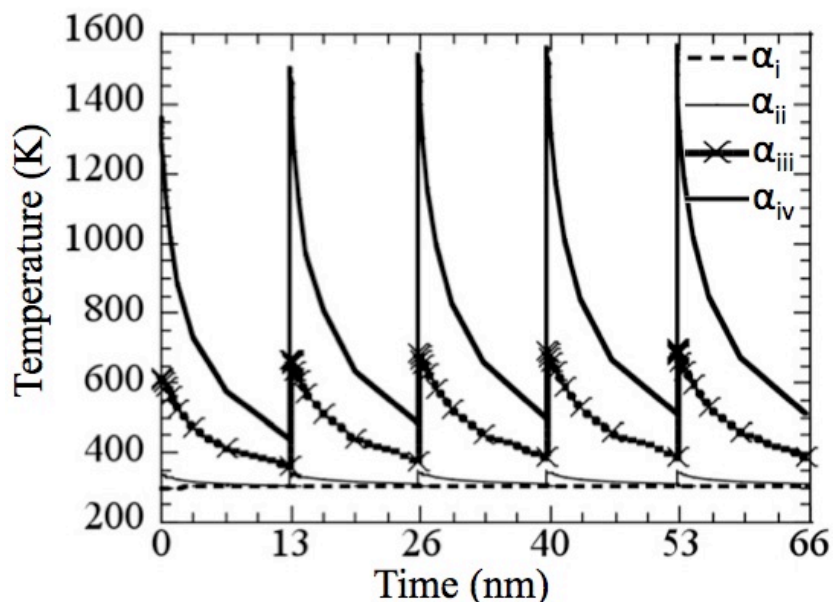


Figure 3.5: Time history of the maximum temperature node at the surface of the substrate.

3.7 Fabrication of Nanowires Using ZPs

A brief summary of the experimental results obtained in the growth of silicon nanowire is presented here. Nanowire fabrications were carried out by James Mitchell (Mitchell et al., 2014). The decomposition of silane after reaching a temperature threshold yields nanowires of roughly the same size as the heated spot. If the gas chamber is also filled with diborane or phosphine the nanowires will be doped. The doping concentration depends on the concentration of the gas mixture. After performing a lot of experiment it was seen that the most important parameters that affected the shape of the wire were: the quality of the fabrication of the ZP, the scanning speed, the delivered laser power, and the laser polarization. Lower scan speeds would yield continuous wires while faster speeds could create non-continuous ones. It was established experimentally that a scan speed of $0.5 \mu\text{m/s}$ was the most optimal one and hence it was used for all subsequent experiments. It was observed that although changing the scan speed would influence in the continuity of the wire it did not influence significantly on the width of the nanowire. A very interesting observation was that the direction of the polarization of the incident light would greatly influence the continuity of

the nanowires. The polarization could be controlled strategically in our favor to yield nanowires much smaller than the diffraction limit (Mitchell et al., 2014). It is believed that the superposition between the incident light and the surface scattered radiation would yield interference patterns in the formation of the nanowires. The shapes of the interference patterns are polarization dependent. Figure 3.6 shows how the polarization of the incident beam influences the direction of the ripples. The polarization is shown as the arrows in the lower right corner of each inset. The top row shows 3 wires constructed using a horizontal polarization. The bottom 3 insets show diagonal, vertical, and circular polarization. We can see that horizontal polarization yields continuous wires.

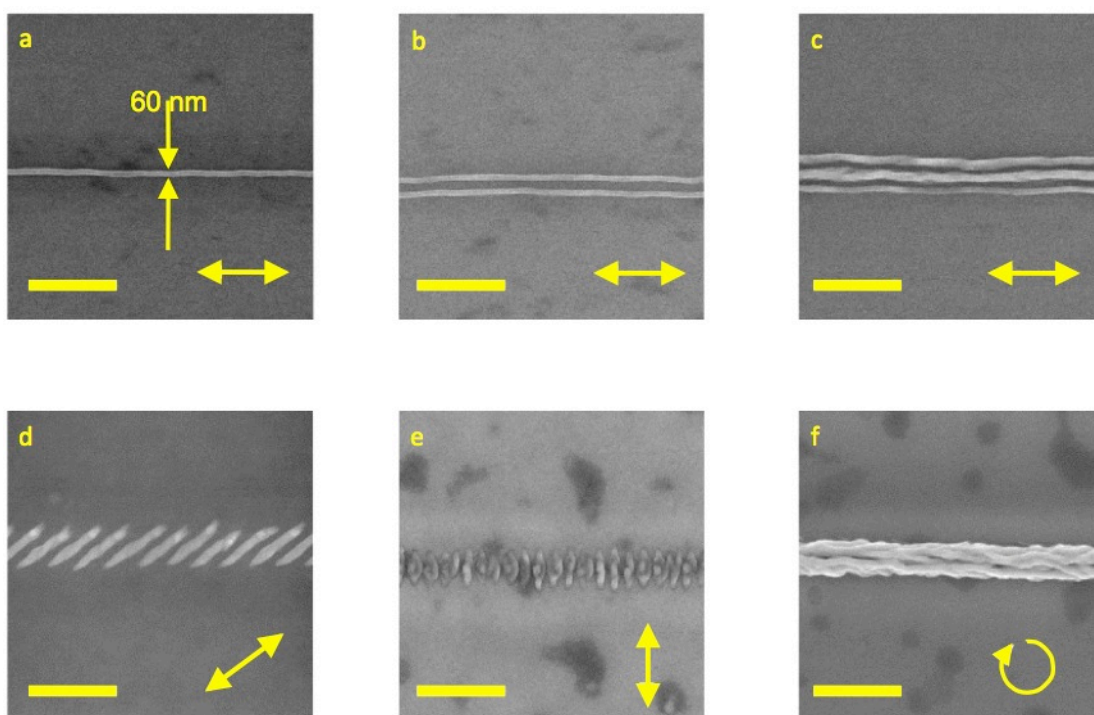


Figure 3.6: Effect of power a) 11 mW, b) 13 mW and c) 20mW; and polarization on the shape of the nanowires formation: d) diagonal polarization, e) vertical polarization, f) circular polarization. Scale bars on the lower left corner of each inset show a distance of 1 μm (Mitchell et al., 2014).

We studied how the power affected the shape of the wires made by using horizontal polarization. By changing the delivered power we were able to control the width and amount of wires. The top row shows from left to right a delivered total power of 11 mW (1 nanowire), 13 mW (2 nanowire), and 20 mW (3 nanowires) respectively.

We also show that 60 nm wires could be fabricated taking advantage of this ripple formation.

3.8 Summary

In this chapter we discussed the use of ZPs to make silicon nanowires. A description of ZPs was presented together with how we used them to create nanowires in an experimental setup. Parameters like the location of the zones, materials and thickness of the structure is critical to the efficiency of the ZP. We presented a fabrication procedure of our design that would ensure maximum efficiency for a level 2 phase ZP and a high yield of ZP structures. Thermal simulations of a surface shined by a small spot, allow us to understand the heat transfer mechanism dependency on the absorption coefficients and thermal properties of the material stack. Finally we present experimental results that show the dependency on nanowire fabrication on speed, polarization, and delivered power. Using all this knowledge the CVD process have been tuned to obtain silicon nanowires as small as 60 nm wide.

CHAPTER 4. THERMAL CALCULATIONS FOR NEAR FIELD FOCUSING

Several applications of bowtie apertures include the generation of a small hot spot at the exit of the aperture due to the presence of an incident laser. In this thesis chapter we analyze the heat transfer generation and dissipation of a bowtie aperture inside a stack of materials that is receiving an input of laser light. Because of light-material interaction there will be a conversion of electric field energy into thermal energy. This conversion of energy can be seen as an absorption that can be related to the imaginary part of the index of refraction of the material interacting with the light. A temperature gradient profile shows us the absorbed energy is diffused into the medium as molecular kinetic energy. This analysis presented here starts with a calculation of the electromagnetic near field surrounding a bowtie aperture.

4.1 Electromagnetic Model

We need an electromagnetic model to understand how light interacts with apertures and how is converted into dissipated energy. All electromagnetic models used in this report are made with the software High Frequency Structural Simulator (HFSS). The software is based on the Finite Element Method (FEM) for solving partial differential equations. In this method a volume is discretized into a mesh composed of tetrahedral elements. The geometry of this mesh is optimized during several iterations of the solution. The size of elements is modified on each iteration accordingly to how fast the electric field changes with respect to space. Zones with higher gradients of electric field will contain smaller elements. During the solution, the differential equations are turned into frequency dependent equations instead of time dependent. This makes the solution a steady state kind. The electromagnetic calculations were done by Nan Zhou (Zhou et al., 2015).

Calculations are made for two major cases that could be considered to have different applications. The 1st case consists of a laser source shining on an aperture with no other components around. For this case we are interested in applications in which the confined spot at the exit of the aperture is on top of dielectric-like surfaces. An example of this kind of surface would be a layer of photoresist used in lithography.

The 2nd case consists of a source shining on an aperture used for Heated Assisted Magnetic Recording (HAMR). A brief description of the HAMR technology is presented in Section 2.1. The case for which we considered HAMR included the effect of coupled light into a stack of material. We will refer to this stack of materials as the recording medium. We assume that the presence of the recording medium has much more impact in the field distribution on the bowtie than the presence of a photoresist, which would be the 1st case. We need to differentiate between these two models because the electromagnetic simulations have shown that the presence of the recording medium yield significantly different electric field results.

Table 4-1: Optical properties used in the electromagnetic model.

Material	Thickness (nm)	n	k
Au	50	0.154	4.908
CrRu	15	3.15	5.68
MgO	5	1.76	0
FePt	8	3.30	4.3
Diamond Like Carbon	1	1.53	0
Air	2	1	0
Diamond Like Carbon	1	1.53	0
Ag/Au	t	0.036/0.154	5.566/4.908
SiO ₂	∞	1.453	0

The model of the recording medium of the 2nd case consists of a stack of layers with different index of refractions (Zhou et al., 2011). [Table 4-1](#) shows the thickness and real and imaginary parts of the refraction index $\tilde{n}=n+ki$ for all the materials of the stacked layers. Figure 4.1(a) shows the stack of materials together with the metal layer where the bowtie is positioned. Figure 4.1(b) shows the dimensions of the bowties. The

dimensions are outlined as a , b , d , and r , where a and b are the sides of the bowtie, d is the gap and r is the radius created by the focused ion beam milling process. The wavelength of the input light of the electromagnetic model was fixed to 800 nm and the incoming field was modeled as a Gaussian beam with a waist of radius of 0.3 microns. The peak incident field was fixed at 1 V/m for all models.

We studied the transmission efficiency as a figure of merit to choose which one is the most effective EM model. Transmission efficiency is defined as the ratio of the power at the exit of the aperture divided by the spatial maximum power at the input of the aperture. We obtained solutions iterating on different dimension of the bowtie and chose the most optimal results. For an incident wavelength of 800 nm, the dimensions that yielded the highest transmission efficiency were $a = b = 400$ nm and $t = 90$ nm. The variable t represents the thickness of the aperture layer. Solutions were calculated using different gaps sizes. The gap size shown as the variable d in Figure 4.1 (b) was analyzed for 5 nm and 20 nm. In the EM models, stronger coupling was seen for the 5 nm gap but 20 nm was used in the thermal models because it corresponds to a more manufacturable size.

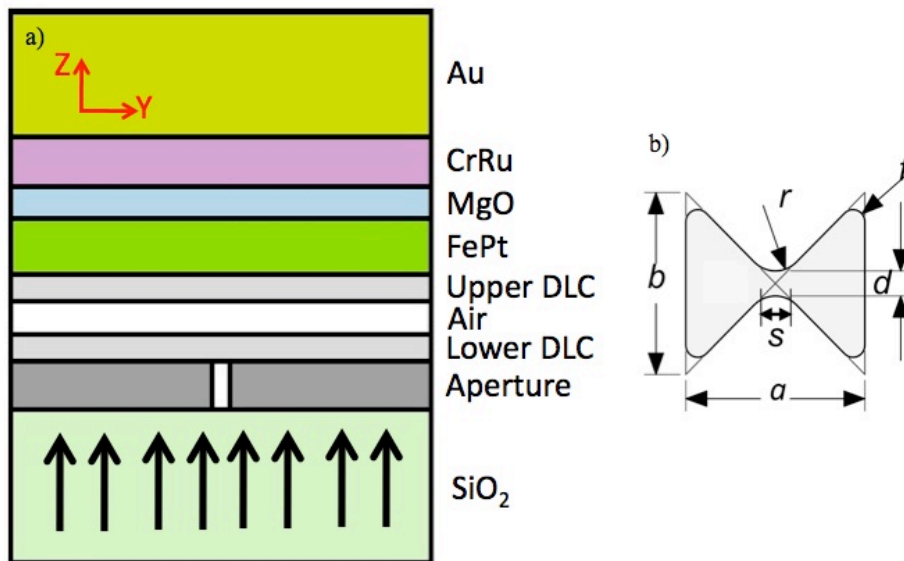


Figure 4.1: a) Stack of materials used for the electromagnetic simulation. Light is incident from the quartz layer. b) Outline of the dimensions of the bowtie. (Zhou et al., 2011).

After choosing a set of dimensions that maximized the coupling efficiency, we needed to analyze how much temperature increase would occur based on the heat absorption. We want for the recording FePT layer to increase its temperature as much as possible without heating too much the aperture layer. Since the aperture layer is the first layer to absorb some of the incoming light, we expect that there will be localized high temperatures at the aperture. We also expect a high temperature rise in the recording medium due to the effect of good insulation surrounding the layer and an approximate power efficiency of 1 of the aperture.

4.2 Thermal Models

4.2.1 Construction of Thermal Model

Each case mentioned is divided into two different models that simulate the effect of heat absorption and conduction dissipation. One model is the aperture and the other model is the material stack of the recording medium. All simulations are made using the same aperture and recording medium models but having different thermal loads. The Z axis is the same as the direction of the incident light and is also the coordinate to delimit the boundaries for the stack of materials. The model with the aperture lies inside the $Z < 0$ region and the stack of materials for the recording medium lies inside the $Z > 0$. The coordinate $Z = 0$ lies exactly at the exit of the aperture. Both models are basically independent heat transfer problems that have inputs from the same electromagnetic model. In order to make this analysis, we must make the assumption that there is not considerable conduction, convection, or radiation within the DLC / Air / DLC layer.

The thermal simulation package consists in a series of codes for preprocessing and solving the model. All codes are written in APDL language, which is an Ansys proprietary language. The code is made in a parametric manner, meaning that if dimensions change, one must just adjust the dimensions in the code and then rerun the code over a clear new environment. Ansys generates the most appropriate mesh using element size commands as guide but care must be taken to ensure that there are no errors during the meshing procedure.

The entire model is build into a large thermal reservoir. With this we ensure that the conditions will eventually reach steady state without over heating the active area. This is a good assumption considering that the heat generation profile is very small compared the aperture. An image of both large thermal reservoirs is shown in Figure 4.2. When zooming into the large model we are able to see either the bowtie structure or the stack of materials. Most of the volume of both thermal reservoirs is modeled as silicon dioxide.

The grid size varies across the model. In order to create the large reservoir for such a small model we need to adjust the mesh size according to the region of detail. Different volumes were created surrounding the bowtie aperture's volume in order to define different material properties and element sizes for them. We have the smallest defined volumes and elements right at the gap of the bowtie and at the recording medium zone in which we apply the heat generation terms. We surround the volumes of the bowtie and heated zone with volumes that contain elements that sequentially increase in size. The elements around the gap of the bowtie and around the heated spot in the recording medium are 6 nm in the X, Y, and Z direction and their size grows to 230 nm in the X and Y direction but kept at 6 nm in the Z direction as they reach the next volume. On the next volumes the average sizes in all X, Y, and Z directions are of 1 μm , 4 μm , and ultimately 50 μm on the outer reservoir. After having these dimensions specified by the user, Ansys tries to create an optimum match between volumes with different element size definition.

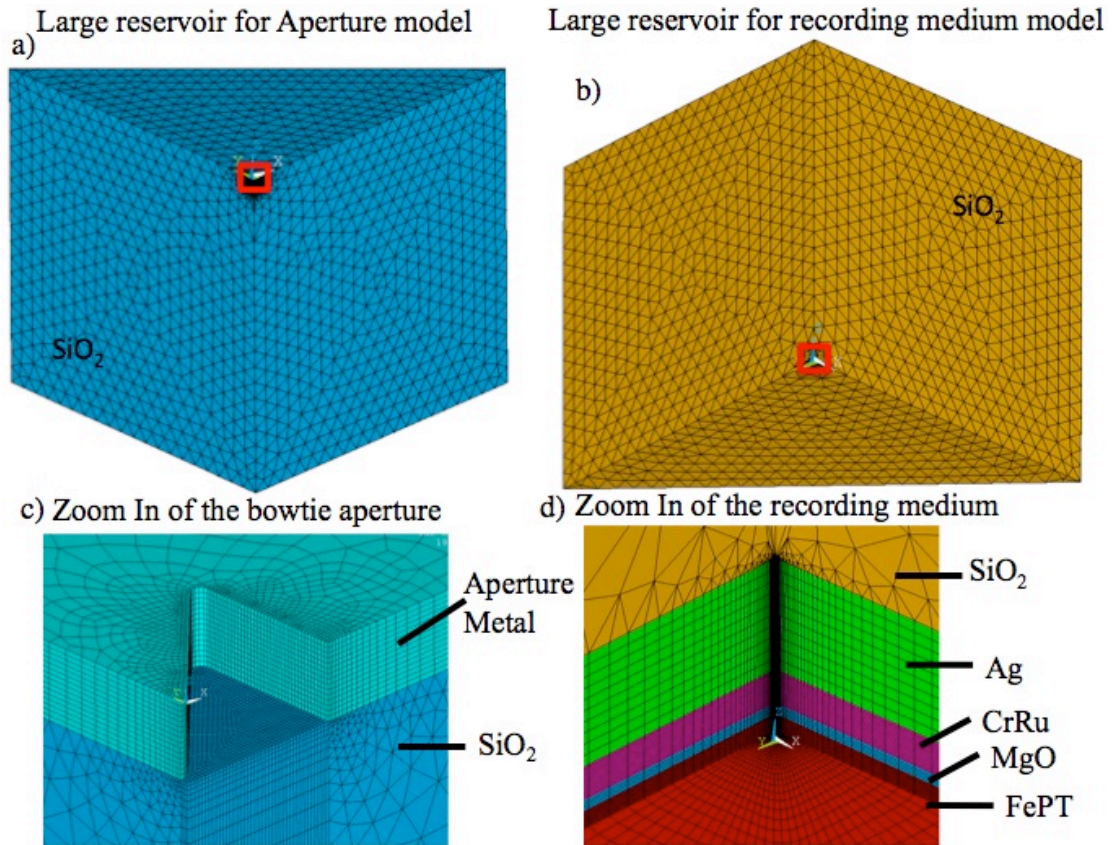


Figure 4.2: View of the large reservoirs for a) aperture model and b) recording medium model in which zoom in of the thermal models for the c) bowtie aperture and for the d) recording medium are shown.

Table 4-2: Thermal properties for materials used in thermal models.

Material	Density (kg/m^3)	Specific Heat (J/kg-K)	Conductivity (W/mK)
Au	18300	129	318
Ag	10490	230	400
SiO_2	2200	1000	2.0
FePt	14660	340	35
MgO	3560	955	45
CrRu	10632	313	109

Material properties for the thermal model are assumed constant with respect to temperature. The material properties necessary for a heat transfer simulation are density,

specific heat and thermal conductivity. Table 4-2 shows these properties for all different materials inside the model.

In order to minimize the necessary amount of elements and nodes we take advantage of the symmetry of the problem and model only one quarter of the aperture and recording medium. Planes of symmetry are the XZ and YZ and they pass through the center of the aperture. The model becomes automatically symmetric when we impose the condition of no heat transfer perpendicular through the XZ and YZ walls. Figure 4.3 shows the model and the symmetry walls. The entire model is subjected to an initial ambient temperature condition of 300 K.

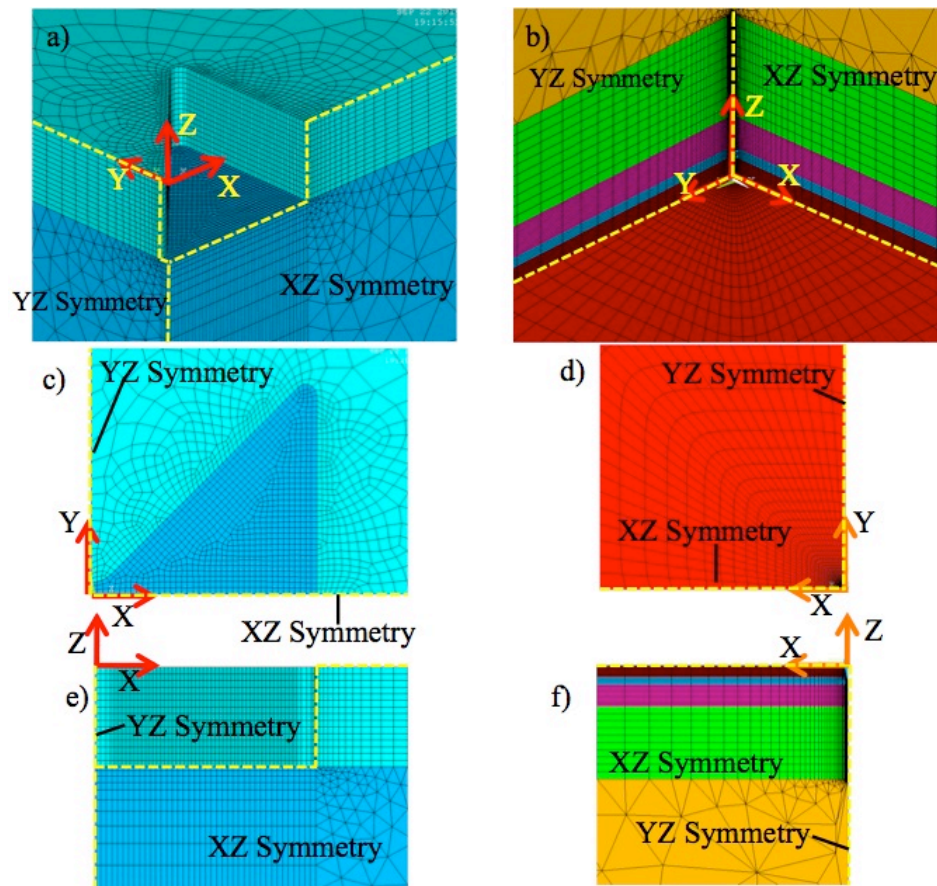


Figure 4.3: Models of bowtie aperture [a) isometric view, c) top view, e) front view] and recording medium [b) isometric view, d) top view, f) front view] showing walls of symmetry used to diminish the number of elements and nodes in the calculations.

After defining the geometry of the thermal model we need to introduce the heat generation data. Volumetric loss density is a term used in HSFF with units of W/m^3 that corresponds to an amount of power absorbed (or lost) in the material. HFSS can use arbitrary spatial coordinates and use them to interpolate values for volumetric loss density at specific locations. As mentioned before, the EM model is normalized to have a spatial peak electric field of 1 V/m. For a peak electric field of 1V/m the peak intensity is $I_0=0.5(E_0)^2/\eta_q=9.136*10^{-4} \text{ W}/\text{m}^2$, where $\eta_q=\eta_0/n$ is the impedance of the wave in the quartz medium. The value of η_0 is the impedance of free space and $n=1.453$ is the index of refraction of the quartz. For a Gaussian beam we can calculate the total power as $P_{\text{tot}}=I_0\pi r^2/2$. Using a radius of $0.3 \mu\text{m}$, the total power is of $1.2916*10^{-16}$ Watts. This is a very small value compared to a practical value used for HAMR. To relate the normalized electric field obtained in the electromagnetic simulations to a real increase in temperature in our thermal models we need to apply a scale factor to the volumetric loss density on all interpolated nodes. We need to make the assumption that the electromagnetic profile does not change with respect to the incident maximum power, or that the material optical properties do not change too much with respect with the temperatures. We have scaled the values to simulate a laser with a power of 50 mW. This adjustment means multiplying the mentioned heat generation values of the interpolated node's by $6.255*10^{14}$.

In order to obtain the heat generation data from the electromagnetic model we must select a group of nodes in the thermal model and extract their coordinates. The selected nodes were the nodes within the coordinates $0 \mu\text{m} \leq X \leq 1.4 \mu\text{m}$, $0 \mu\text{m} \leq Y \leq 1.4 \mu\text{m}$, and $-270 \text{ nm} \leq Z \leq 0 \text{ nm}$. The nodes outside of this selected region have negligible values of heat generation. These coordinates are imported into the HFSS software and used for an interpolation of the heat generation data. Then the data is scaled and coded into heat generation commands for Ansys. Figure 4.4 shows the profile for the heat generation shown for both aperture and recording medium models.

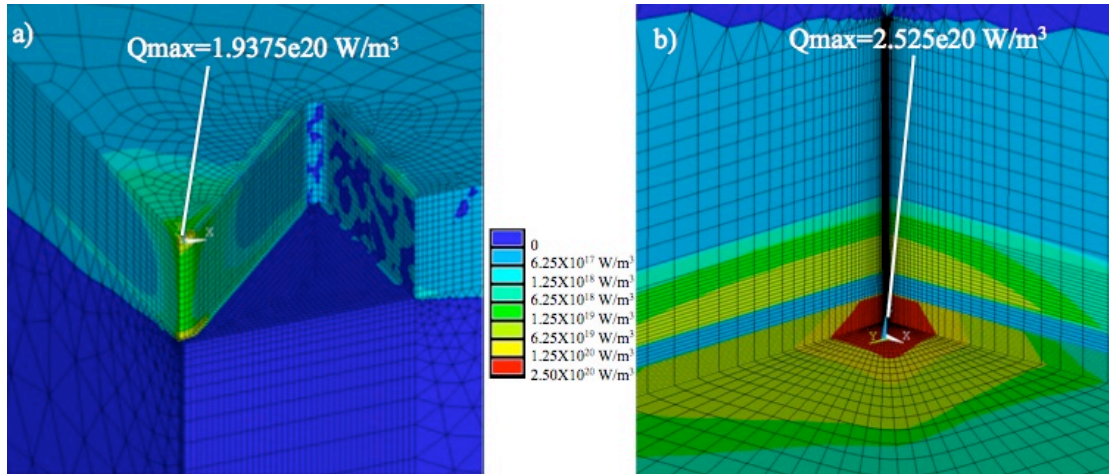


Figure 4.4: Heat generation profile presented in W/m^3 on a logarithmic scale for a) the bowtie aperture and b) the recording medium.

4.2.2 Results and Analysis

We are interested in comparing the increase in temperature of a bowtie aperture for gold and silver. For each material we are also interested in comparing the effect of having a recording medium vs. not having the medium. Figure 4.5 shows the silver aperture maximum temperatures ranging from 0 to 1 ns. We can immediately see that the coupling of the energy on the recording medium augments the field intensity profile in the aperture. Figure 4.6 shows the same result for a gold aperture. When comparing gold and silver we can see that gold absorbs less heat. The coupling that arises when the medium is present seems to increase the amount of energy that is absorbed and converted into heat inside the aperture.

We want to investigate the relationship of the thermal profile of the aperture VS the one for the recording medium for both aperture materials. This will help us identify if gold or silver is better suited for HAMR application. Figure 4.7 shows the temperature time history result on the node of maximum temperature in the recording medium. We have defined a figure of merit called the thermal efficiency as $\eta = \Delta T_{\text{RM}} / \Delta T_{\text{ap}}$, which can be described by the ratio of the maximum temperatures changes in the recording medium (ΔT_{RM}) and the aperture model (ΔT_{ap}). This efficiency helps us determine the thermal performance of using a gold aperture vs. a silver aperture. The thermal efficiency for a

silver aperture was calculated to be $\eta_{Ag}=58.4$ and for a gold one it was $\eta_{Au}=7.29$. While a silver aperture does not increase its temperature as much it also couples more energy into the recording medium making it the most suitable material of our design.

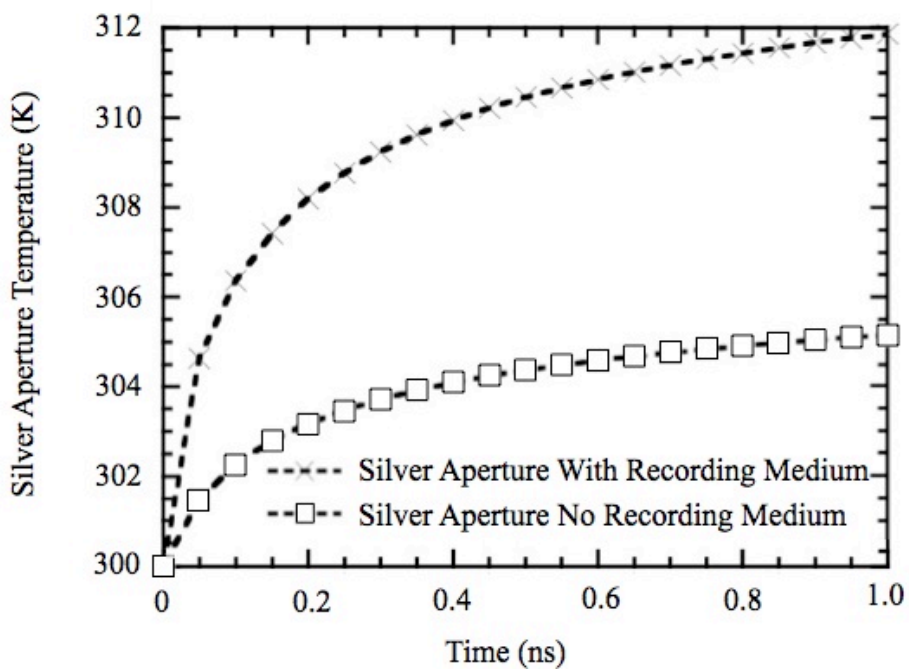


Figure 4.5: Temperature vs. time solutions for a silver aperture with and without the influence of the of the HAMR recording medium.

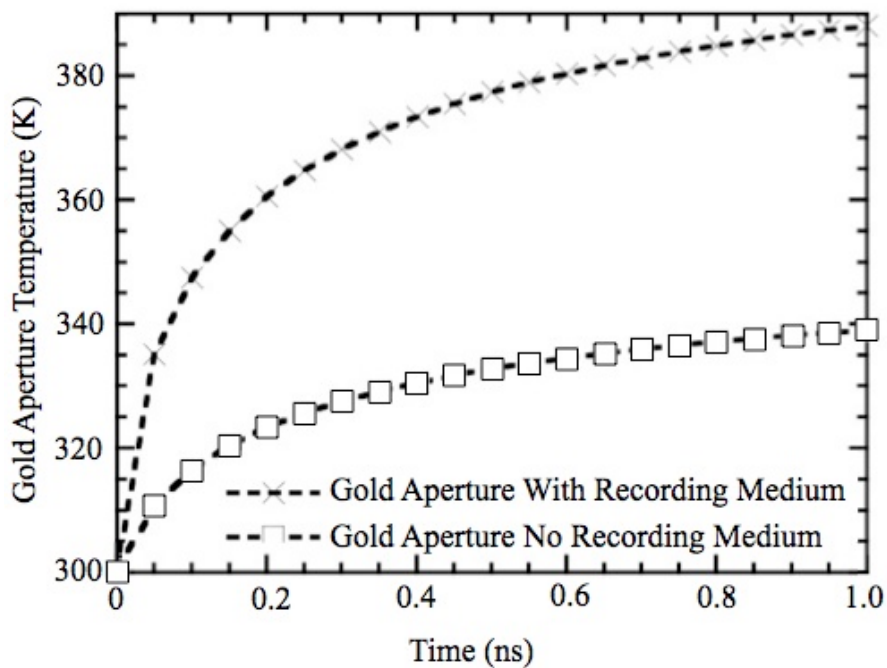


Figure 4.6: Temperature vs. time solutions for a gold aperture with and without the influence of the of the HAMR recording medium.

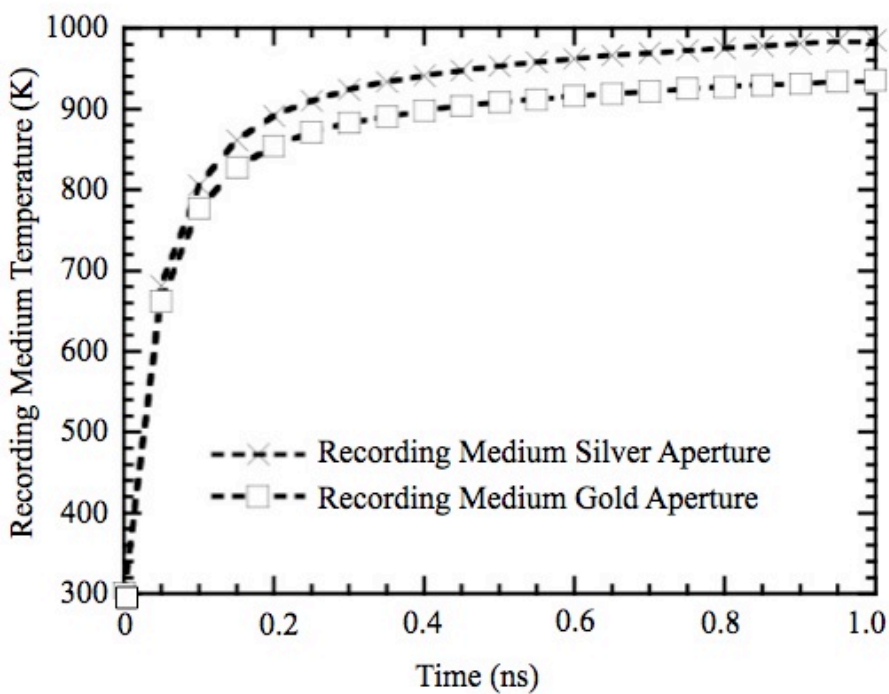


Figure 4.7: Temperature vs. time solutions for a recording medium maximum temperature using silver and gold apertures.

In order to validate our results we have made further calculations that can support the temperature profiles obtained. The thermal dissipation length is a characteristic distance that can give us a qualitative idea about how much the results are within an expected range of values. A thermal dissipation length μ_t can be described by equation $\mu_t = 2\sqrt{\alpha t}$ (Marín, 2010). The value of μ_t is approximately defined as the radius of a heat outspreaded sphere inside a material of thermal diffusivity α after a time t has elapsed. It can be seen as the length in which the change in temperature is $1/e$ fraction of the maximum temperature change on the model. We compared the dissipation lengths inside the mediums in which heat was applied and also we would measure how far away the hot spot have dissipated in the model. We can see that after a certain time, the energy still lies within a volume for which the enclosing temperature is still the initial temperature of 300 K. Figure 4.8 shows some profiles of heat dissipation for which a length has been measured and calculated. The black line presented in insets b) and d) shows approximately the isothermal line in which the temperature is $1/e$ fraction of the maximum temperature change. The measured length should be similar to the thermal dissipation length. For a medium made of gold after a heating lasting 50 ps, the thermal dissipation length is 164 nm. For the recording medium after a heating lasting the same amount of time, the thermal dissipation length is 37 nm. Since the thermal dissipation length describes the radius of a much simpler single nodal heat profile inside a homogeneous medium, we can't exactly expect to obtain the exact same length. However this test is good enough to check that our results are within a proper order of magnitude. A more rigorous check of the models would be to make a direct calculation of the energy conservation inside the model.

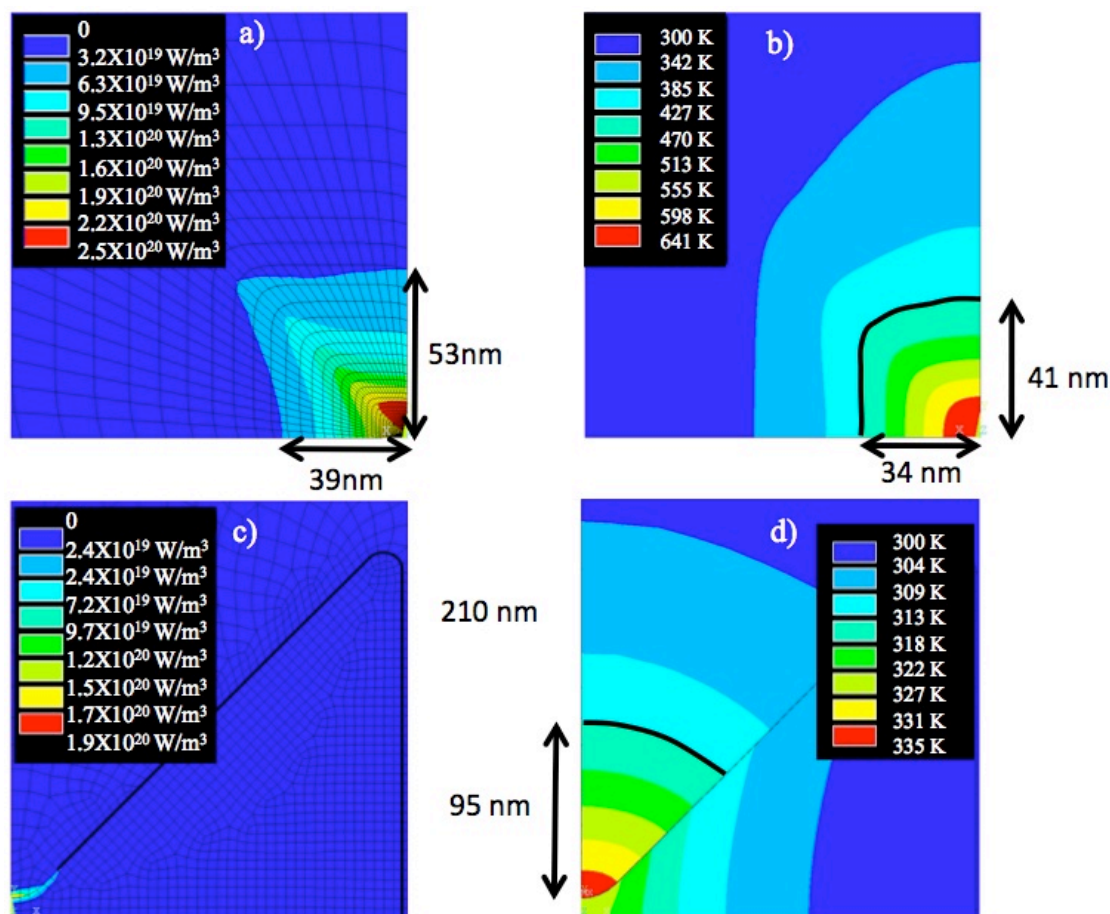


Figure 4.8: a) Heat generation profile in a recording medium using a gold aperture and b) its resulting temperature after 50 ps. c) Heat generation profile in a gold aperture and d) its resulting temperature after 50 ps.

We can check energy conservation by comparing the integration of a volumetric heat generation to the increase in thermal energy over a given volume. In order to integrate the applied heat generation we write a code that multiplies the volume of each element by the average of the volumetric heat generation input of the element. Since the value is assigned to nodes rather than elements we calculate the nodal average volumetric heat generation input for each element. For our tetrahedral 8 nodes elements we simply average this value for the 8 nodes. We also calculate the increase in thermal energy of the volume. We read the solution for a certain time step and find the average temperature of each element. The increase in temperature from the initial 300 K value of each element is used to calculate the rise in the internal energy of the element. Table 4-3

shows the comparisons of the input heat generation summation and the rise in thermal energy for all models. We can see that values are in agreement with energy conservation.

Table 4-3: Energy conservation calculations for verification of the thermal models.

Model	Heat generation summation (pJ)	Summation of thermal energy increase (pJ)
Gold aperture with recording medium.	0.528	0.581
Silver aperture with recording medium.	9.51×10^{-2}	8.58×10^{-2}
Gold aperture no recording medium.	0.2907	0.343
Silver aperture no recording medium.	5.25×10^{-2}	4.98×10^{-2}
Recording medium using gold aperture.	1.62	1.65
Recording medium using silver aperture.	1.96	2.00

4.3 Summary

In this chapter we have presented thermal models describing the temperature rise in an aperture used for confined heating applications. We have presented models for a bowtie aperture meant for lithography and for HAMR and we have compared the use of gold and silver for these applications. An electromagnetic model can give us results of how much heat is absorbed in a medium and a thermal model can tell us how this absorbed heat will result in a temperature rise. For the application of HAMR, a figure of merit compares the efficiency of potential materials by comparing the unwanted rise in temperature in the bowtie aperture to the wanted temperature rise in the recording medium. Based on this figure of merit we determine that an aperture made of silver is more efficient than an aperture made of gold. Finally a verification of the results can be made by comparing thermal diffusion length in the models and by performing an energy conservation analysis.

CHAPTER 5. SUB-DIFFRACTION LIGHT FOCUSING USING A CROSS SECTIONAL RIDGE WAVEGUIDE NANOSCALE APERTURE

In the past, most of the ridge apertures were made using sequential fabrication methods such as focused ion beam (FIB) milling. These methods are relative simple because they require no more than two steps, for example, metal deposition and ion beam milling for FIB. One of the disadvantages of using FIB for fabrication is the proximity effect that produces rounded features and reduces the localization of light. Schemes to overcome this problem include milling in such a way that the input side of light is the one with the FIB milled rounded feature and the exit side has a minimum rounded shape for light focusing (Chen et al., 2015, Leen et al., 2010).

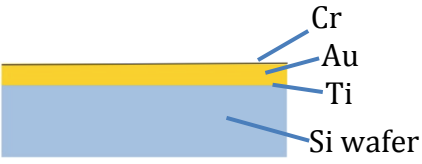
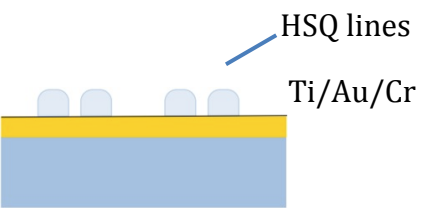
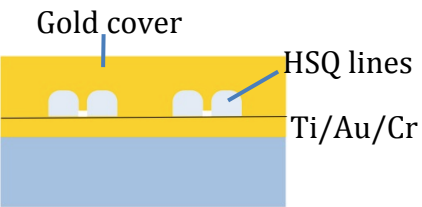
This thesis chapter presents a method for fabricating ridge apertures using planar layer-by-layer lithography process. The apertures are constructed in the cross section of a dielectric layer surrounded by metal layers from top and bottom. This method can potentially overcome the proximity effect in the FIB process, and also be suitable for mass production of aperture arrays. Numerical computations are used for the design of these apertures. The fabricated apertures are characterized using scattering near field optical microscopy (s-NSOM).

5.1 Layer-by-Layer Fabrication of Ridge Apertures

Table 5-1 shows the procedure to fabricate the ridge aperture in a layer-by-layer manner. A cleaned silicon substrate is coated with layers of titanium, gold, and chrome. A 5 nm titanium layer serves as an adhesion layer between the 150 nm of gold and the silicon substrate, while a 3 nm chrome layer serves as an adhesion layer between the gold layer and a photo resist layer of hydrogen silsesquioxane (HSQ). The 3 layers deposited shown on step 1 of the Table 5-1 can be coated in one single vacuum pump down a the

Kurt J. Lesker® e-beam evaporation chamber. We spin-coated HSQ XR-1541 4 % e-beam resist at 4000 RPM for 45 seconds and soft baked the substrate at 120°C for 3 minutes. We exposed the substrate using electron beam at a current of 0.3 nA with a dose of 2000 $\mu\text{C}/\text{cm}^2$. The exposure pattern of lines is shown in the second step of Table 5-1. The exposed HSQ is further developed in tetramethylammonium hydroxide for 45 seconds. This process is intended to generate pairs of lines of HSQ with thickness of about 85 nm and a width of 220 nm, which can vary according to the design. The spacing between the lines in each pair is about 25 nm. After developing the HSQ layer, we coated a 5 nm layer of titanium and a 200 nm layer of gold in a chamber capable of rotating the substrate. These last 2 layers were also coated using the same e-beam evaporation system mentioned before. The substrate rotation was used to get as much gold into the gap between the two lines of HSQ as possible. The final structure is illustrated in Figure 5.1. It forms a previously studied c-aperture (Leen et al., 2010). The recipe mentioned above lets us fabricate apertures with a particular set of dimensions that will be analyzed using numerical methods and tested using s-NSOM and shown in sections 5.2 and 5.3. The gap for this recipe is determined to be about 40 nm using scanning electron microscopy (SEM) imaging. The dimension of the gap is determined by the amount of gold deposited into the gap between the two HSQ lines and becomes smaller when two lines are positioned further. For similar doses there was a consistency in the gap of the ridge with respect to the separation of the lines. A potential reason for this gap consistency is the small under developed area created by the over exposure of the proximity effect. At this step of the fabrication the lines are enclosed by gold and the apertures need to be sliced in such that their cross section is exposed.

Table 5-1: Process flow for the layer-by-layer fabrication of ridge apertures.

#	NAME	DESCRIPTION	SCHEMATIC
1	Coat of Ti – Au – Cr layer.	E-beam evaporation deposition of 5 nm of Ti followed by 150 nm of Au followed by 3 nm of Cr.	
2	Aperture lines	Coating of XR-1541 4% at 4000 RPM for 45 seconds. Soft baked at 120°C for 3 minutes. Exposed with a dose of 2000 $\mu\text{C}/\text{cm}^2$. Developed in TMAH for 45 seconds.	
3	Aperture cover	E-beam evaporation deposition of 5 nm of Ti followed by 200 nm of Au.	

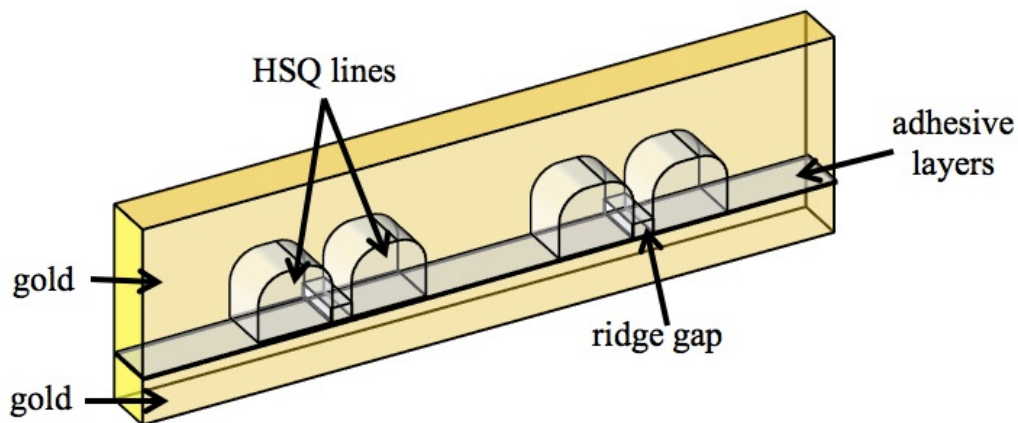


Figure 5.1: Schematic of the final ridge aperture.

Table 5-2: Process flow for the characterization of the layer-by-layer ridge aperture.



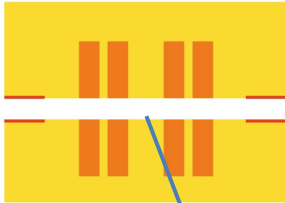

#	NAME	DESCRIPTION	SCHEMATIC
1	Top view of step 3 from Table 5-1	The image to the right shows the top view after having finished the step 3 from Table 5-1	<p>Aperture lines covered with Au</p> 
2	Laser cut	Use a focused laser to make cuts in the substrates without making cuts to the HSQ lines. The cuts should be made by opening a shutter at the proper places within the same scan direction and should be perpendicular to the HSQ lines.	 <p>Laser cut</p> <p>Laser cut</p>
3	Crystal guided mechanical cut.	Use a thin sharp blade to make a force in the laser cuts of step 2. A crystal guided cut should follow the laser cut lines and slice the HSQ lines exposing their cross section.	 <p>Crystal guided mechanical cut</p>
4	Platinum deposition	Electron beam assisted deposition of platinum is made. Then FIB assisted platinum is deposited with a current of 0.3 nA. The depth of the deposition should be higher than 5 μm .	 <p>FIB Pt deposition</p>

Table 5-2: Continued.

#	NAME	DESCRIPTION	SCHEMATIC
5	FIB cuts	Perform a large cut, which will serve as the entrance side of the aperture and a small cut close to the edge of the substrate that will serve as the exit side of the aperture.	<p>FIB large cut</p> <p>30 μm</p> <p>FIB edge small cut</p>
6	s-NSOM	The sample is taken into an s-NSOM for characterization where light is incident from the side with the large FIB cut and the electric field measurements of the aperture is from the side with the small FIB cut.	<p>Pt deposition</p> <p>FIB large cut</p> <p>s-NSOM light</p> <p>FIB small cut</p> <p>Si substrate</p>

Great efforts have been made in order to access the structure for NSOM measurement, as illustrated in Table 5-2 and described below. First a laser cut was made using an amplified femtosecond laser cutting system as shown in the schematic for step 2 in Table 5-2. The cut is made along the silicon crystal lattice direction. The electron beam exposed lines are intentionally made perpendicular to the crystal lattice orientation. The laser does not directly cut the exposed lines to avoid damage to the fabricated aperture. The substrate is then broken apart by mechanical force as shown in the schematic for step 3 in Table 5-2. In order to access the aperture using an NSOM tip, a cross section wall is made using FIB milling. Similar to a conventional cross-section FIB milling a Pt deposition is required. This process starts with an electron-beam assisted platinum deposition of 200 nm, which is made in order to protect the sample from the ion beam used in the localization of the platinum wall. A 5 μm or taller wall is fabricated close to the edge of the crystal-guided cut using a tool for FIB assisted platinum

deposition (step 4 schematic of Table 5-2). The height of the wall is chosen as 5 μm or more to avoid background light during the s-NSOM measurements as well as to protect the apertures during the FIB milling. It is possible that the height of the wall does not match the height specified by the deposition command. The actual fabricated height might depend on what beam current is used and it needs to be measured after deposition. After the wall has been deposited and its height confirmed, the sample is ready for milling. Step 5 of Table 5-2 shows the FIB milling used to reveal the aperture cross section. There are 2 main cut regions on both the entrance and exit side of the wall. A relatively large (about 30 μm away from the wall) FIB milling allows light to reach the aperture. A smaller cut is made close to the edge mechanical cut of the substrate. This smaller cut reveals the exit side of the aperture. The exit side needs to be relatively close to the edge (around 1 μm) because the s-NSOM tip needs to have access to the aperture. The direction of the s-NSOM light as well as both cuts described above are shown in a side view of the aperture on the schematic of step 6 of Table 5-2.

Figure 5.2 shows SEM images of intermediate steps including the exposure and development of the HSQ lines shown in Figure 5.2(a) and the edge of the substrate after the laser cut shown in Figure 5.2(b). Figure 5.2(c) shows a tilted view of the deposited wall for several groups of lithography lines. The figure also shows large cuts that are used to allow the s-NSOM light to reach the apertures. Figure 5.2(d) shows a front view of 2 apertures after the entire sample preparation process for the s-NSOM measurement is finished. Figure 5.2(e) shows a tilted rotated view of the entrance side of an aperture wall that has been thinned down.

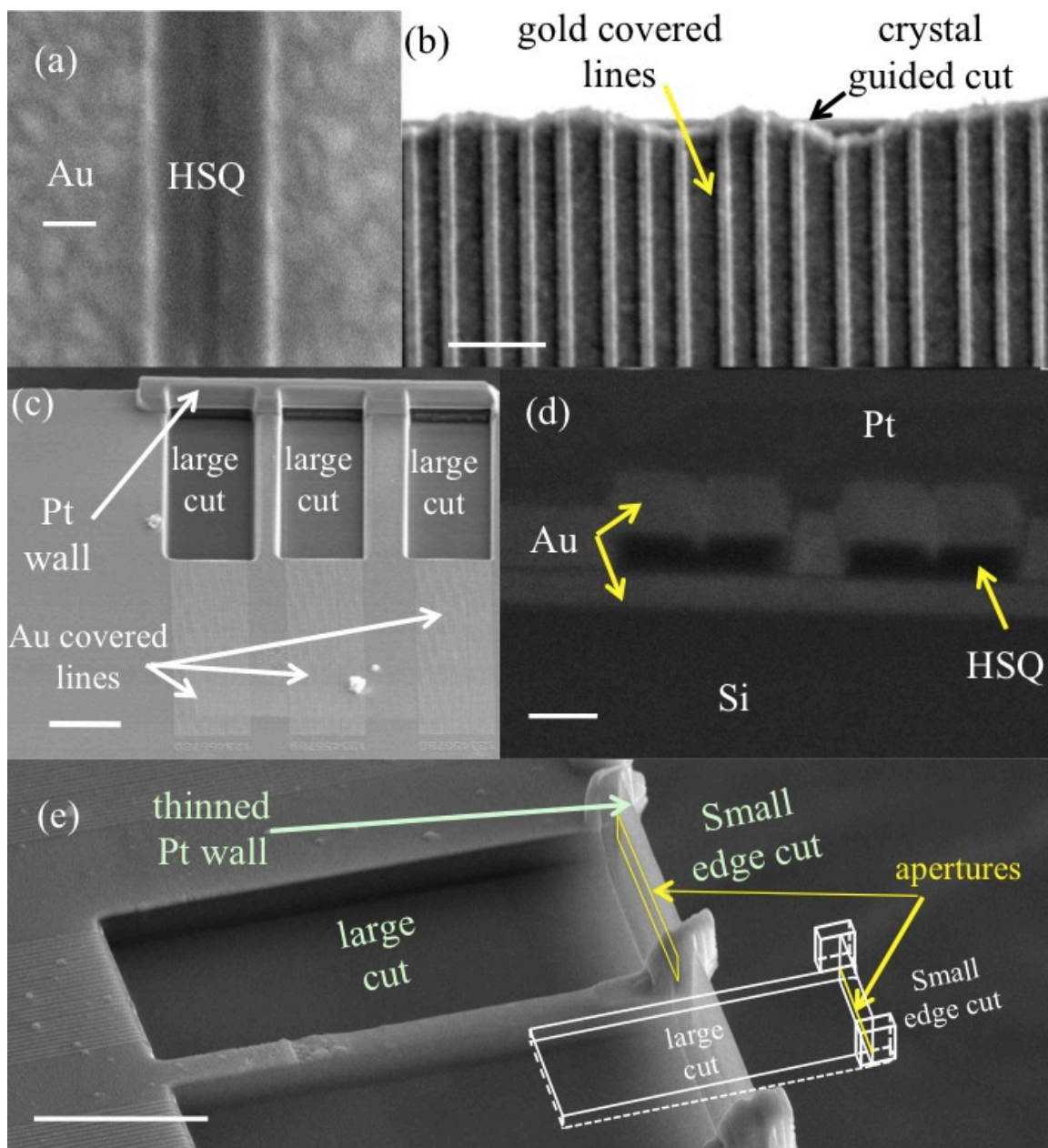


Figure 5.2: SEM images of the ridge aperture structure during intermediate steps. (a) Exposed and developed HSQ lines (scale bar is 200 nm). (b) Aperture lines on edge of the substrate after crystal guided cut (scale bar is 1 μm). (c) Image of the large cuts made behind the Pt walls (Inset scale bar is 10 μm). (d) Zoomed cross-section picture of 2 apertures (Inset scale bar is 200 nm). (e) Tilted and rotated image of a thinned down Pt wall (Inset scale bar is 10 μm).

5.2 Electromagnetic Simulation

Electromagnetic simulations were made using ANSYS high frequency structural simulator (HFSS), which is a commercial FEM solver. Tetrahedral elements divide the aperture by using nodes for which all the Maxwell equations are satisfied. Results of the same FEM solver have been validated (Şendur et al., 2004) for problems related to metallic spheres in a dielectric medium (Mie, 1908). The geometry of the model is shown in Figure 5.3 (a). It consists of two lines made of HSQ with width of 220 nm and height of 85 nm. A ridge with width of 25 nm separates them. The length of the ridge is of 50 nm, which leaves a gap of 35 nm filled with HSQ. 2 fillets with radius of 20 nm were modeled at the two sides of the ridge leading towards the gap. These shapes and dimensions were taken from the SEM images of the final produced aperture. The electromagnetic modeling was carried out by Anurup Datta.

The modeling software automatically generates the mesh. The size of the mesh is adaptively changed after each solution iteration. The element size becomes finer where the field magnitude has a higher gradient. Ultimately at the final solution the elements sizes range from 2 nm close to the tip of the ridge to 100 nm at other places. To save time, we take advantage of the symmetry of the aperture by modeling half of the aperture and forcing a perfect magnetic conductor boundary condition at the symmetry plane. At all other surfaces of the model that are facing towards the exterior of the model, we impose boundary conditions for absorption, which means that there will not be any field reflection back into the model. An incident radiation with wavelength of 633 nm is applied corresponding to a Gaussian beam with a radius of 500 nm and with the polarization shown in Figure 5.3(a). The optical properties of gold were taken from a paper written by Johnson and Christy (1972).

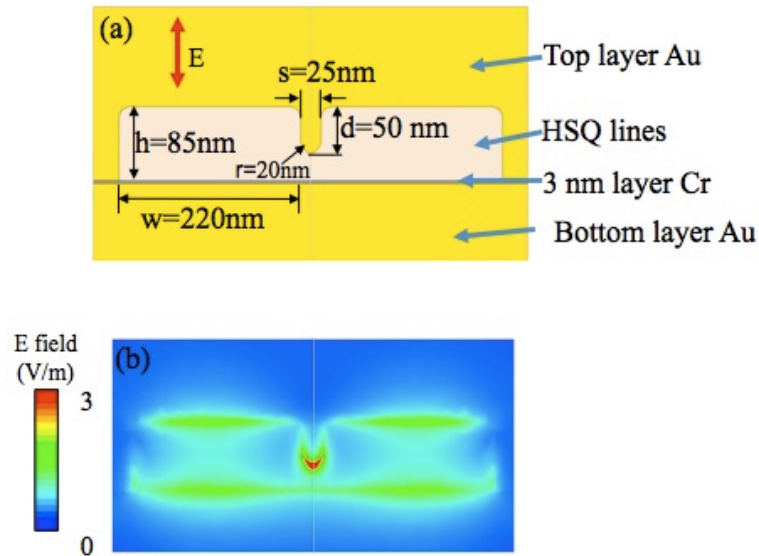


Figure 5.3: (a) Electromagnetic simulation model for the cross sectional ridge waveguide apertures. (b) Electric field distribution for the model depicted in (a).

Figure 5.3(b) shows the electric field distribution corresponding to the dimensions shown in Figure 5.3(a) at a distance of 5 nm away from the exit plane of the aperture. The tip of the penetrated portion of the top layer of gold acts as a lightning rod and helps the confinement of electric field giving rise to an intense hot spot. When compared with the incident light, the electric field is enhanced by several times at the tip with the help of the effect of the localized surface plasmons.

It is known that for ridge apertures, the dimensions of the aperture relative to the wavelength play an important role in determining the performance of the apertures and their ability to concentrate light into a hotspot (Jin, 2004). After a series of simulations, it has been noted that the two most significant parameters that affect the focusing of the ridge apertures presented in this chapter are the penetration depth and the width of the line, which are the dimensions d and w respectively in Figure 5.3(a). Figures 5.4 and 5.5 present electric field distributions for variations of the parameters d and w .

Figure 5.4 show the electric field distribution at a plane 5 nm from the exit plane when the penetration depth, d is varied as 35 nm , 55 nm , and 75 nm (Figure 5.4 (a), (b), and (c) respectively). For these simulations, except the penetration depth d , all the other dimensions are kept constant as in Figure 5.3(a). We find that there is an optimum

penetration depth where the field concentration at the tip is maximum. For a particular wavelength, the change in the penetration depth causes a change in the resonance condition for the surface charge accumulation at the tip and it maximizes at a particular length, which in our case is 55 nm.

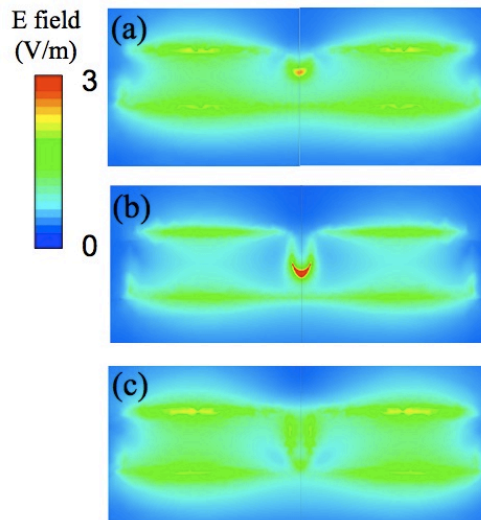


Figure 5.4: Electric field distribution of an aperture with 3 different penetration depths. (a) $d = 35$ nm, (b) $d = 55$ nm, (c) $d = 75$ nm. Other dimensions are fixed to the values presented in Figure 5.3(a).

Next, we study the effect of the change in the aperture size by altering the HSQ line widths. In Figure 5.5, the line width, w is 120 nm, 220 nm, and 440 nm (Figure 5.5 (a), (b), and (c) respectively) and all the other dimensions are fixed as in Figure 5.3(a). From the results of the electric field, we find that changing the aperture width changes the charge accumulation due to surface plasmon at the edge of the gold-HSQ interface. In Figure 5.5(a), when the line width is 120 nm, the field concentration at the tip is higher. At the same time there is a high field concentration at the interface between the bottom gold layer and HSQ lines. This high field concentration will prevent us from obtaining an isolated hot spot. When the line width is increased to 220 nm as in Figure 5.5(b), the field concentration at the interface spreads out and becomes weaker and an isolated hot spot is obtained. Increasing the line width even more as shown in Figure 5.5(c) would make the apertures wider and allow propagating modes of the ridge waveguide. From

these simulations and considerations of fabrication processes, we focus on the demonstration of apertures with $w = 220$ nm and $d = 45$ nm.

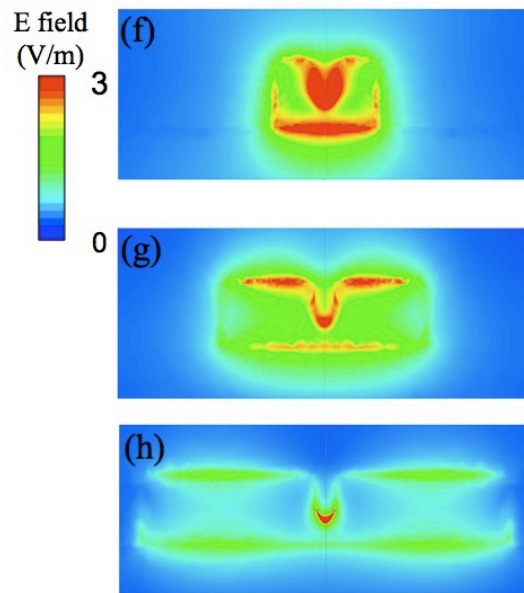


Figure 5.5: Electric field distribution of an aperture with 3 different widths (a) $w = 120$ nm, (b) $w = 220$ nm, (c) $w = 440$ nm. Other dimensions are fixed to the values presented in Figure 5.3(a).

5.3 NSOM Characterization

The fabricated apertures were positioned in the s-NSOM system where far field images were taken through an objective lens. Figure 5.6(a) shows a far field image of the exit of the apertures while there is incident light on them. Figure 5.6(b) shows an illustration of the top view of the far field measurement including the necessary FIB cuts to thin down the wall to allow the incident light. In order to help locate the apertures during characterization we made some marks. Marks were milled below the apertures row and deposited above the aperture row as shown in Figure 5.6(c). The milling of the mark was made with an FIB. The deposition of the above marks was FIB assisted platinum deposition. Deposition marks were made instead of milling to avoid creating through-windows in the wall that would allow light to interfere with the measurements.

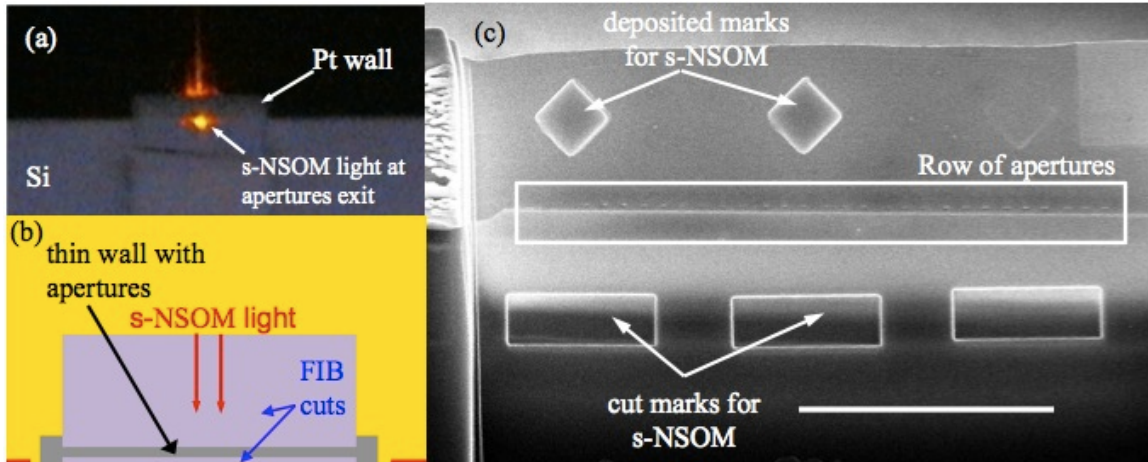


Figure 5.6: Far-field image of apertures. a) Front view of a far field image. b) Top view of the schematic. (c) Marks made to locate easier the apertures during s-NSOM imaging.

A home built s-NSOM based on a commercial AFM system was used to characterize the optical near field of the fabricated apertures. The s-NSOM was operated in transmission mode where a beam of light of wavelength 633 nm was focused on the sample with the help of an objective lens. At the same time, an AFM tip was engaged with the sample in the tapping mode and the sample was raster scanned. The scattered light from the AFM tip was then collected by a separate objective lens and was directed to a photodetector. The scattered light signal was demodulated with a lock-in amplifier at the tip oscillating frequency and its higher harmonics. This demodulated signal was used to extract the near field information, which had reduced background noise. Zhou (2014) developed detailed description of this experimental setup. The NSOM measurements were carried out with the help of Anurup Datta.

The design of the aperture can yield different results depending of their dimensions. Some will not be capable of yielding localized spots in the tip of the ridges. Figure 5.7 shows different apertures that created light spots that seem to have the same size as the apertures. Interestingly the spots appear to be on top of the gold layers instead of being inside the gaps. The image shows SEM, AFM, s-NSOM 2nd harmonics, and s-NSOM 3rd harmonics images for these apertures.

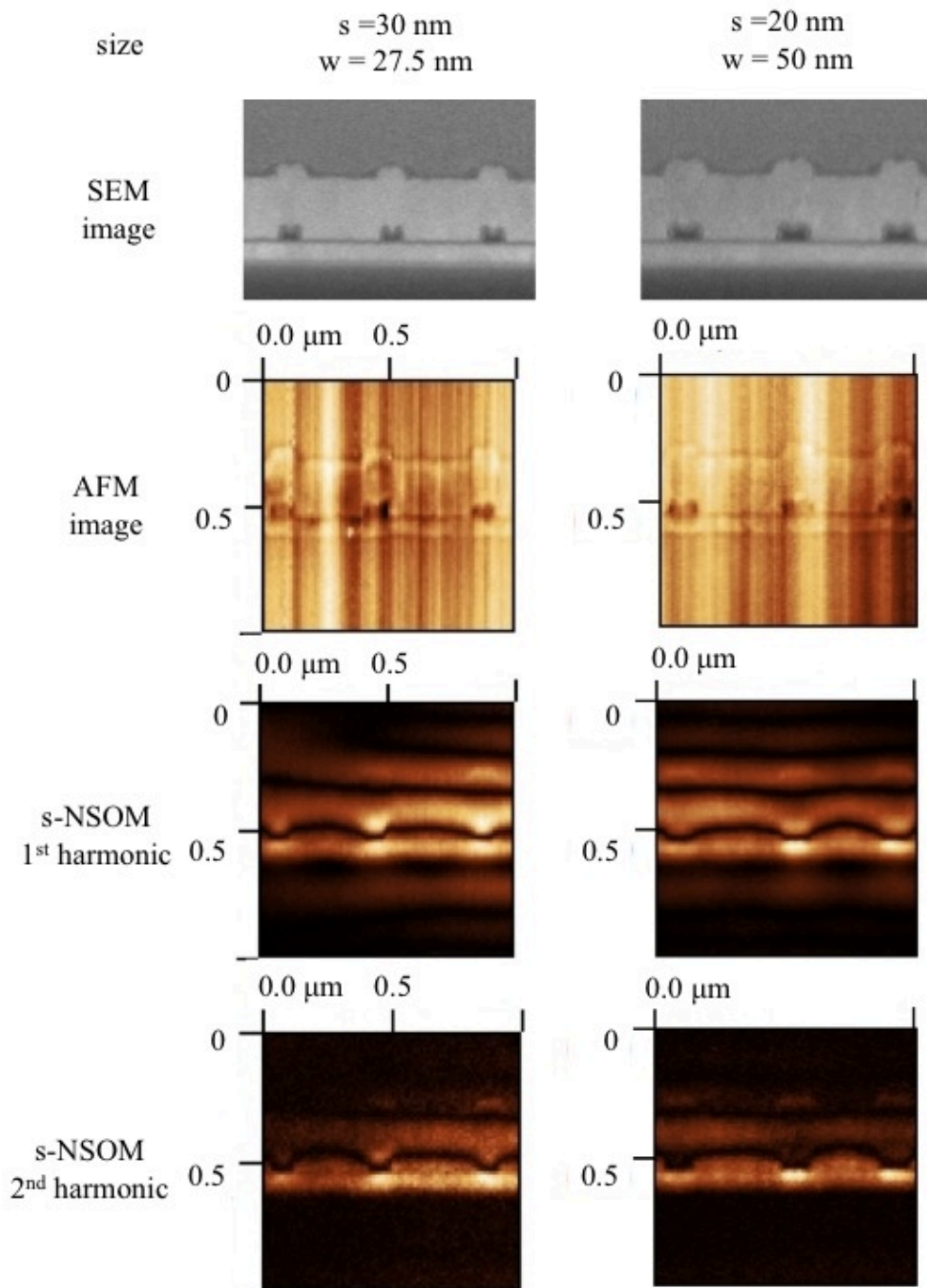


Figure 5.7: Experimental characterization of the apertures without localized spots. The 1st column corresponds to apertures with sizes $s = 30 \text{ nm}$ and $w = 27.5 \text{ nm}$. The 2nd column corresponds to apertures sizes $s = 20 \text{ nm}$ and $w = 50 \text{ nm}$. The rows are different images. From top to bottom SEM, AFM, s-NSOM 2nd harmonic, and s-NSOM 3rd harmonic.

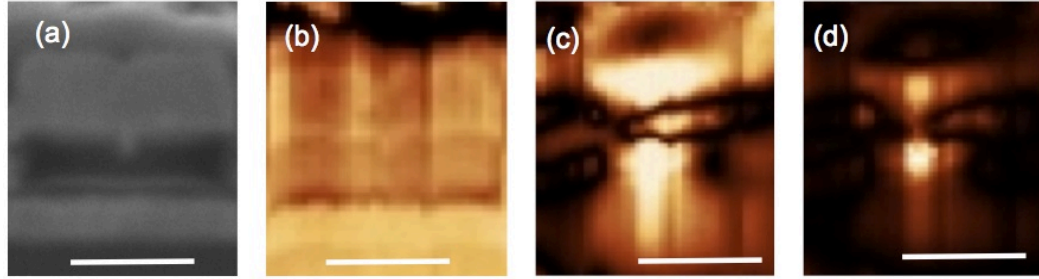


Figure 5.8: Experimental characterization of the apertures with localized spot. (a) SEM image of the aperture, (b) AFM topography of the aperture, (c) s-NSOM signal collected at the 2nd harmonic of the tip oscillation frequency from the aperture of (a) and (d) s-NSOM signal collected at the 3rd harmonic of the tip oscillation frequency from the aperture of (a). The scale bars in these figures are 250 nm long.

Figure 5.8 shows the s-NSOM results as well as the SEM image and the AFM topography for an aperture that successfully confines light in a spot at the gap below the ridge. Figure 5.8(a) shows the SEM image of an aperture fabricated according to dimension discussed in the previous section. Figure 5.8(b) shows the corresponding AFM topography image. It can be seen from the AFM topography image that the exposed surface of the cross section, unlike normal ridge apertures fabricated by methods such as FIB milling, is fairly planar. Figure 5.8(c) shows the s-NSOM signal collected at the 2nd harmonic of the tip oscillation frequency and Figure 5.8(d) shows s-NSOM signal collected at the 3rd harmonic of the tip oscillation frequency. Both Figure 5.8(c) and 5.8(d) show the enhancement of the field intensity at the tip of the gold protrusion. However, it is seen that the high intensity spot from the third harmonic measurement is closer to what is predicted by the simulation shown in Figure 5.3(b), whereas the image obtained from the second harmonic contains unwanted background fringes. Therefore, 3rd harmonic signals provide a better background suppression and reduction of the peripheral fringes and helps in better visualization of the near field spot as seen in Figure 5.8(d). With these images we can demonstrate that our aperture is capable of focusing light into sub-diffraction limit spot sizes.

5.4 Summary

We demonstrated a concept of using a layer-by-layer fabrication process to produce ridge apertures in the cross section of layered thin films. Numerical calculations of the electric field distribution were used to evaluate the apertures. The s-NSOM measurements showed the localization of the exit field. Further development and refinement of the fabrication and characterization methods will allow fabrication of apertures in large quantities for many applications.

CHAPTER 6. CONCLUSIONS AND RECOMMENDATIONS

6.1 Conclusions

Devices for sub-diffraction limit confinement have the potential of performing fabrication of small patterns for many applications. The devices we discussed in this thesis were zone plates and ridge apertures. Zone plates were successfully proven to be capable of heating small surfaces on which we fabricated nanowires with widths much smaller than the diffraction limit. Ridge apertures were successfully proven as great tools for optical nanolithography in an array of patterns. They were also being proven to have a great potential for heated assisted magnetic recording, which is believed to be part of the technology for next generation hard drives. Different fabrication methods were studied to improve the yield of all these devices and to decrease the dimension of the generated optical spots. A lot of the successful procedures presented in this thesis led us to the conclusion that electromagnetic field can be confined to dimensions much smaller than the diffraction limit. This work also led us to believe that we can further increase the resolution of the nanofabrication methods with some additional work. The next section presents a few ideas that can help us make better devices.

6.2 Recommendations

Most of the recommendations presented in this section are meant to improve the resolution of the lines made in our lithography setup. Our group has been working extensively using ridge apertures for lithography. Starting from the work of contact lithography using C apertures (Wang et al., 2006) and bowtie apertures (Wang et al., 2006) to scanning lithography using apertures milled in AFM probes (Murphy-Dubay, 2008) to a series of parallel lithography; our group has been trying to find ways to produce advance nanofabrication. There was a moment in which the research focus

shifted from single aperture lithography to the use of an array of apertures by the creation of a parallel lithography system (Uppuluri et al., 2010). Following that work we developed a system for high precision dynamic control of gap between mask and substrate that would improve the resolution of our scanning aperture lithography (Wen et al., 2015). We considered improving this system by sharpening the aperture edges or using 2-photon absorption to help confine light even further. To aid with the sharpening of the aperture edges we present ideas to keep improving the methods of inverted apertures on thin membranes and sacrificial layers.

6.2.1 Improving Thin Membrane Transfer

Section 2.2.4 discusses a scheme made for the transfer of an inverted thin membrane to the top of an island. This island lies inside a substrate that is used for parallel lithography using bowtie apertures that are milled at the top of the island. We were not able to make a thin membrane transfer clean enough to obtain a mask suitable for parallel scanning nanolithography. Our goal is to find a combination of requisites of the fabrication steps that will make the device useful.

One requisite is that the process should ensure permanent attachment of the thin membrane. The substrate will need to be cleaned in between lithography experiments to minimize contamination. We will clean the substrates by submerging them in strong solvents such as acetone and isopropyl alcohol. The thin membrane can be well attached by stitching it as shown in Table 2-3 or by finding an adhesive strong enough to withstand solvent cleaning. Another requisite is that the ISPI grating (described in detail in section 2.3) must survive the presence of any chemical that will be used to aid in the attachment of the membrane. The last requisite to mention here is that contamination and flatness variation of the top of the island should be kept at a minimum. In the process presented, the top of the island is kept covered with an etching mask until the development of the ISPI grating. This helps avoiding the deposition of unwanted material at the top of the island. The presence of the adhesive can create thick layers around the island during coating or during the approach of the membrane. If a thick layer

were formed during approaching we would need to clean it and repeat the approach with a new thin membrane wafer.

After seeing all of these requisites we notice that the selection of the adhesion layer is key to the success of the transfer. The method presented in section 2.2.4 was the closest to success that we obtain but there might be other combination of process that could work better. There were previous test made using a thin layer of HSQ as an adhesive. The thin membrane would be approached and the HSQ would be hardened by electron beam exposure. One problem with this process is that the interface between the thin membrane and the island needed to be accessible to an e-beam. Another problem is that the thickness of the HSQ might need to be chosen carefully. If the layer is too thin there might not be a good enough adhesion but if it is too thick there could be contamination or a loss in flatness at the top of the island. In order to have access to the HSQ adhesion interface we can drill a hole in the glass substrate that holds the thin wafer membrane. If a soft gel adhesive is used as shown in step 3 of Table 2-2, we need to make a hole in it as well. We might need to use some form of alignment scheme to make sure that both holes are aligned with the center of the membrane. Figure 6.1 shows a schematic of a variation of the membrane transfer process previously shown in Table 2-1, 2-2, and 2-3 in which we use HSQ as an adhesion. The holes in the glass slide and in the soft gel are shown in the figure. To harden the HSQ it would be necessary to remove the mask aligner glass by dissolving the acetone in the points shown in the figure and bring the rest of the assembly into a chamber with an electron beam. Once the HSQ is hardened we should release the bottom glass slide in order to release the substrate with the island.

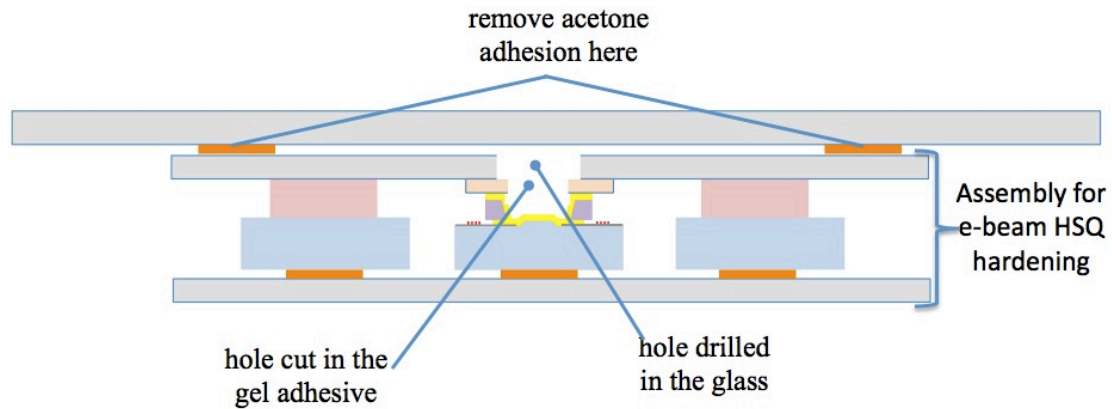


Figure 6.1: Schematic showing a variation for thin-membrane transfer process using HSQ as an adhesion layer.

A process using an HSQ adhesion layer was tried in the past but was unsuccessful due to alignment and contamination problems. Some of our problems were fixed after choosing a super glue because it was a thinner adhesive material. With this thinner layer we avoided contamination. We solve the problem of misalignment using adhesive gel to permit for surfaces to self align during approach of substrates. Using a combination of thinner HSQ with the self-alignment adhesive gel, could give us a permanent adhesion and we would not need to use the stitching method presented in Table 2-3. This process as shown in Figure 6.1 is could be tried in the future.

6.2.2 Thin Membrane Island

One possible alternative to use reverse membrane milling would be to find a way to not have to transfer the membrane. Instead we could find a way of building an island around the membrane. As shown in Figure 6.2(b), a thin wafer membrane could be etched in order to create an island that will raise the membrane above the rest of the substrate. We could insert a hardening substance inside the window as shown in Figure 6.2. The hardening substance would make the membrane more likely to survive a scanning parallel lithography. This hardening substance could be a cured layer of optical adhesive, HSQ, SU-8 (negative optical photo resist), or some soft polymer. This layer should have some transparency to 355 nm UV light in order to perform the lithography process. If we use this arrangement to perform 2 photon absorption lithography the layer should have transparency to 800 nm. PELCO® substrates sold by TED Pella offers thin

membrane wafers with windows of 100 μm . These substrates could serve to fabricate an island with dimensions close to the ones used in our latest parallel lithography publications (Wen et al, 2014; Wen et al., 2015). A picture of the mentioned thin wafer membrane is shown in Figure 6.2 (a). To etch this mask we need to design a method to protect the fragile thin membrane from a relatively deep etch. It seems that it would be necessary to insert the hardening substance before the etching procedure. It also seem like a very strong etching mask is necessary. In order to integrate the use of this arrangement with our lithography design we could adapt a mask substrate with ISPI by drilling a hole as shown in Figure 6.2 (c) in the middle of the substrate. A focused femto second laser could be used to make this milling. A proper milling would include the use of a consistent dose and set of laser cutting CNC commands that would yield always the same cut depth. To compensate for the potential variations of the thin membrane wafer thickness we can design ISPI gratings that will give gap measurements for a broader range than usual. Maybe we can fabricate several grating designs that are optimal for different gap ranges.

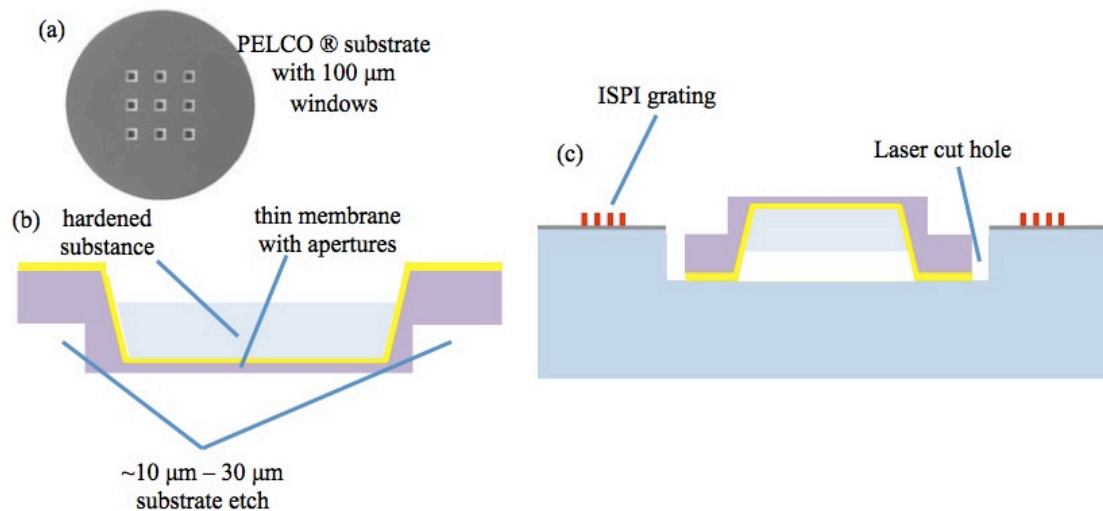


Figure 6.2: Fabricating an island on a thin membrane wafer. (a) Thin membrane wafer of 100 μm windows (Source from Ted Pella website) (b) Creating an island around a thin membrane window. (c) Adapting a thin membrane island to a substrate with ISPI lithography marks.

Our final goal is to scan a thin membrane that is milled from the reverse direction in order to prove that we can perform scanning parallel lithography and produce lines

smaller than the ones presented in the past. The lines would be smaller due to a sharper bowtie design that would improve the confinement of the EM field.

6.2.3 Improving the Sacrificial Layer Method

In order to improve the system we also considered the use of sacrificial layers on aperture metal layers. The use of sacrificial layers to obtain sharper apertures was mentioned in section 2.2.2. The conclusion of this section indicated that there were regions near the aperture that were resistant to the sacrificial layer etching. This was seen for all layer combinations that we tried. It was established that a potential cause for this to happen was the presence of gallium ion implantation and its effect on the etching rate of the material. We now suggest that if our previously mentioned potential cause is correct, we can try to find a way to selectively etch the ion implantation. It was mentioned in literature that the addition of hydrogen peroxide into a potassium hydroxide could help selectively etch areas of silicon that has been implanted with gallium ions (Han et al., 2015). If we use silicon as a sacrificial layer coated on top of any given metal we could use a KOH solution to etch the sacrificial layer and then add H_2O_2 to selectively etch the sacrificial layer that has been affected by the ion implantation. Perhaps there might be other combinations of chemicals that can create similar effects to gallium ion implantation in sacrificial layers made of other materials.

6.2.4 Two-photon Absorption Lithography

Two-photon absorption (TPA) lithography could provide for a method to further decrease the size of the exposed and developed region. In regular absorption lithography, the photoresist absorbs all of the light that is incident on it. In the lithography experiments that we have presented in chapter 2, we use photoresist S1805 which is formulated to be optimized to g-line (436 nm) exposure. This photoresist has very minimal absorption in wavelengths above 500 nm. This means that laser light of 800 nm should not expose the photoresist easily. This is not necessarily true if the light is very intense. Under intense light there will be the simultaneous absorption of 2 photons for the photoresist molecules. On the regions where the field is more intense, there will be

more molecules that will undergo TPA. When there is TPA, there is an equivalent absorption of a higher energy photon with half the wavelength, which for our particular photoresist lies inside the spectrum region that will change its developer solubility. The advantage of this process is that the area of exposure will depend not only on the time but will also be relatively sensitive to the intensity of the field.

Using the bowtie electromagnetic field confinement, we could obtain further control of the dimension of the lithography spot created and try to make it smaller. A different design of the bowtie should be made in order to obtain the necessary propagation mode for an incident laser of 800 nm. Focusing of the beam might be done to obtain the necessary field but care should be taken that the field is not intense enough as to damage the metal close to the gap of the aperture. The same fabrication procedure to create the parallel bowtie lithography mask can be used in order to obtain parallel TPA lithography.

TPA can also be used to investigate the field distribution for the apertures. The comparison of TPA and one-photon absorption lithography can give more information of the near fields.

LIST OF REFERENCES

LIST OF REFERENCES

- Bäuerle, D. (1996). *Laser Processing and Chemistry* (2nd ed., pp. 334–337). Berlin: Springer-Verlag.
- Bethe, H. A. (1944). Theory of diffraction by small holes. *Physical Review*, 66(7-8), 163.
- Bharadwaj, P., Deutsch, B., and Novotny, L. (2009). Optical Antennas, *Adv. Opt. Photon.* 1(3), p. 438-483.
- Challener, W. A., Gage, E., and Itagi, A. (2006). Optical transducers for near field recording. *Jpn. J. Appl. Phys.* 45(8), pp. 6632–6642
- Challener, W. A., Peng, C., Itagi, A. V., Karns, D., Peng, W., Peng, Y., Yang, X., Zhu, X., Gokemeijer, N. J., Hsia, Y.-T., Ju, G., Rottmayer, R. E., Seigler, M. A., and Gage, E. C. (2009). Heat-assisted magnetic recording by a near-field transducer with efficient optical energy transfer. *Nature Photonics*, 3, 220–224.
- Chao, D., Patel, A., Barwicz, T., Smith, H. I., & Menon, R. (2005). Immersion zone-plate-array lithography. *Journal of Vacuum Science & Technology B: Microelectronics and Nanometer Structures*, 23(6), 2657.
- Chen, Y., Chen, J., Xu, X., and Chu, J. (2015). Fabrication of bowtie aperture antennas for producing sub-20 nm optical spots. *Opt. Express*, 23(7), 9093–9099.
- Duan, H., Hu, H., Kumar, K., Shen, Z., and Yang, J. K. W. (2011). Direct and Reliable Patterning of Plasmonic Nanostructures with Sub-10-nm Gaps. *ACS Nano*, 5(9), 7593–7600.
- Farhan, M. S. , Zalnezhad, E., Bushroa, A. R., and Sarhan, A. A. D. (2013). Electrical and optical properties of indium-tin oxide (ITO) films by ion-assisted deposition (IAD) at room temperature. *Int. J. Precis. Eng. Manuf.*, 14(8), 1465–1469.
- Fulton, T. A., and Dolan, G. J. (1983). New approach to electron beam lithography. *Applied Physics Letters*, 42(8), 752.
- Galus, M. D., Moon, E., Smith, H. I., and Menon, R. (2006). Replication of diffractive-optical arrays via photocurable nanoimprint lithography. *Journal of Vacuum Science & Technology B: Microelectronics and Nanometer Structures*, 24(6), 2960.

- Ghaemi, H., Thio, T., Grupp, D., Ebbesen, T. W., and Lezec, H. (1998). Surface plasmons enhance optical transmission through subwavelength holes. *Physical Review B*, 58(11), 6779.
- Han, Z., Vehkamäki, M., Mattinen, M., Salmi, E., Mizohata, K., Leskelä, M., and Ritala, M. (2015). Selective etching of focused gallium ion beam implanted regions from silicon as a nanofabrication method. *Nanotechnology*, 26(26), 1–10.
- Hayashi, S. and Okamoto, T. (2012). Plasmonics: visit the past to know the future. *J. Phys. D: Appl. Phys.*, 45(43), 433001.
- Hogness, T. R. , Wilson, T. L., and Johnson, W. C. (1936). The thermal decomposition of silane. *Journal of the American Chemical Society*, 58(1), 108–112.
- Jin, E. X., and Xu, X. (2004). Finite-difference time-domain studies on optical transmission through planar nano-apertures in a metal film. *Japanese Journal of Applied Physics*, 43(1), 407–417.
- Jin, E. X., and Xu, X. (2006). Plasmonic effects in near-field optical transmission enhancement through a single bowtie-shaped aperture. *Applied Physics B*, 84(1-2), 3–9.
- Johnson, P. B., and Christy, R.-W. (1972). Optical constants of the noble metals. *Physical review*, B 6(12), 4370-4379.
- Kim, M.-K., Sim, H., Yoon, S. J., Gong, S.-H., Ahn, C. W., Cho, Y.-H., and Lee, Y.-H. (2015). Squeezing Photons into a Point-Like Space. *Nano Letters*, 15(60), 4102–4107.
- Kim, Y., Kim, S., Jung, H., Lee, E., and Hahn, J. (2009). Plasmonic nano lithography with a high scan speed contact probe. *Optics Express*, 17(22), 19476–19485.
- Kinzel, E. C. (2010). Ridge Aperture Optical Antennas, 1–217.
- Kryder, M. H., Gage, E. C., McDaniel, T. W., Challener, W. A., Rottmayer, R. E., Ju, G., Hsia, Y.-T., and Erden, M. F. (2008). Heat Assisted Magnetic Recording. *Proceedings of the IEEE*, 96(11), 1810–1835.
- Leen, J. B., Hansen, P., Cheng, Y.-T., Gibby, A., and Hesselink, L. (2010). Near-field optical data storage using C-apertures. *Applied Physics Letters*, 97(7), 073111.
- Leen, J. B., Hansen, P., Cheng, Y., and Hesselink, L. (2008). Improved focused ion beam fabrication of near-field apertures using a silicon nitride membrane. *Optics Letters*, 33(23), 2827–2829.
- Leviatan, Y. (1986). Study of near-zone fields of a small aperture. *Journal of Applied Physics*, 60(5), 1577.

- Lezec, H. J. , and Thio, T. (2004). Diffracted evanescent wave model for enhanced and suppressed optical transmission through subwavelength hole arrays. *Optics Express*, 12(16), 3629–3651.
- Maier, S. A., *Plasmonics: Fundamentals and Applications* (Springer, 2007).
- Marín, E. (2010). Characteristic dimensions for heat transfer. *Lat. Am. J. Phys. Educ.*, 4(1), 56–60.
- Mason, D. R., Menabde, S. G., Yu, S., and Park, N. (2014). Plasmonic Excitations of 1D Metal-Dielectric Interfaces in 2D Systems: 1D Surface Plasmon Polaritons. *Sci. Rep.*, 4, 4536.
- Matsumoto, T., Nakamura, K., Nishida, T., Hieda, H., Kikitsu, A., Naito, K., and Koda, T. (2008). Thermally assisted magnetic recording on a bit-patterned medium by using a near-field optical head with a beaked metallic plate. *Appl. Phys. Lett.*, 93, 031108.
- Mie, G. (1908). Beiträge zur Optik trüber Medien, speziell kolloidaler Metallösungen. *Ann. Phys.*, 25(3), 377-445.
- Mitchell, J. I., Zhou, N., Nam, W., Traverso, L. M., and Xu, X. (2014). Sub-diffraction Laser Synthesis of Silicon Nanowires. *Scientific Rep.*, Vol 4, 3908-1-4.
- Moon, E. E., Everett, P. N., Meinhold, M. W., Mondol, M. K., and Smith, H. I. (1999). Novel mask-wafer gap measurement scheme with nanometer-level detectivity. *Journal of Vacuum Science & Technology B: Microelectronics and Nanometer Structures*, 17(6), 2698–2702.
- Murphy-DuBay, N., Wang, L., and Xu, X. (2008). Nanolithography using high transmission nanoscale ridge aperture probe. *Appl. Phys. A*, 93, 881 -884.
- Nam, W., Mitchell, J. I., Tansarawiput, C., Qi, M., and Xu, X. (2013). Laser direct writing of silicon filed effect transistor sensors. *Appl. Phys. Lett.*, 102(9), 093504.
- Pan, L., Park, Y.-S., Xiong, Y., Ulin-Avila, E., Zeng, L., Sun, C., Bogy, D. B., and Zhang, X. (2010). Flying plasmonic lens at near field for high speed nanolithography. In *SPIE Advanced Lithography*, 7637, 763713–763713–6.
- Schonbrun, E., Rinzler, C., and Crozier, K. B. (2008). Microfabricated water immersion zone plate optical tweezer. *Applied Physics Letters*, 92(7), 071112.
- Schonbrun, E., Ye, W. N., and Crozier, K. B. (2009). Scanning microscopy using a short-focal-length Fresnel zone plate. *Optics Letters*, 34(14), 2228–2230.
- Şendur, K., Challener, W., and Peng, C. (2004). Ridge waveguide as a near field aperture for high density data storage. *Journal of Applied Physics*, 96, 2743.
- Sharrock, M. P. (1990). Time-dependent magnetic phenomena and particle-size effects in recording media. *IEEE Trans. Magn.*, 26(1), 193–197.

- Shi, X., and Hesselink, L. (2002). Mechanisms for enhancing power throughput from planar nano-apertures for near field optical data storage. *Japanese Journal of Applied Physics*, 41, 1632–1635.
- Smith, H. I., Menon, R., Patel, A., Chao, D., Walsh, M., and Barbastathis, G. (2006). Zone-plate-array lithography: A low-cost complement or competitor to scanning-electron-beam lithography. *Microelectronic Engineering*, 83(4-9), 956–961.
- Srituravanich, W., Pan, L., Wang, Y., Sun, C., Bogy, D., & Zhang, X. (2008). Flying plasmonic lens in the near field for high-speed nanolithography. *Nature Nanotech*, 3(12), 733–737.
- Stipe, B. C., Strand, T. C., Poon, C. C., Balamane, H., Boone, T. D., Katine, J. A., Li, J.-L., Rawat, V., Nemoto, H., Hirotsune, A., Hellwig, O., Ruiz, R., Dobisz, E., Kercher, D. S., Robertson, N., Albrecht, T. R., and Terris, B. D. (2010). Magnetic recording at 1.5 Pb m^{-2} using an integrated plasmonic antenna. *Nature Photonics*, 4, 484–488.
- Tanaka, K., Ohkubo, T., Oumi, M., Mitsuoka, Y., Nakajima, K., Hosaka, H., and Itao, K. (2001). Numerical simulation on read-out characteristics of the planar aperture-mounted head with a minute scatterer. *Japanese Journal of Applied Physics*, 40(3S), 1542.
- Tanaka, K., and Tanaka, M. (2003). Simulation of an aperture in the thick metallic screen that gives high intensity and small spot size using surface plasmon polariton. *Journal of Microscopy*, 210(3), 294–300.
- TED PELLA 100 μm membrane: Website image Retrieved from http://www.tedpella.com/grids_html/silicon-nitride.htm#_21500_10
- Uppuluri, S.M.V., Kinzel, E.C., Li, Y., and Xu, X. (2010). Parallel optical nanolithography using nanoscale bowtie aperture array. *Optics Express*, 18(7), 7369-7375.
- Wang, L., Jin, E.X., Uppuluri, S.M., and Xu, X. (2006). Contact optical nanolithography using nanoscale C-shaped apertures. *Opt. Exp.*, 14, 9902-9908.
- Wang, L., Uppuluri, S., Jin, E., and Xu, X. (2006). Nanolithography using high transmission nanoscale bowtie apertures. *Nano Lett.*, 6(3), 361–364.
- Wang, Y., Du, Z., Park, Y., Chen, C., Zhang, X., and Pan, L. (2015). Quasi-3D plasmonic coupling scheme for near-field optical lithography and imaging. *Optics letters*, 40(16), 3918-3921.
- Wen, X., Datta, A., Traverso, L. M., Pan, L., Moon, E. E., and Xu, X. (2015). High throughput optical lithography by scanning a massive array of bowtie aperture antennas at near-field. *Sci. Rep.*, 5, 16192.

- Wen, X., Traverso, L. M., Srisungsitthisunti, P., Xu, X., and Moon, E. E. (2013). High precision dynamic alignment and gap control for optical near-field nanolithography. *J. Vac. Sci. Technol. B.*, 31(4), 041601.
- Wen, X., Traverso, L. M., Srisungsitthisunti, P., Xu, X., and Moon, E. E. (2014). Optical nanolithography with $\lambda/15$ resolution using bowtie aperture array. *Appl. Phys. A*, DOI: 10.1007/s00339-014-8265-y.
- Wi, J.-S., Lee, T.-Y., Jin, K.-B., Hong, D. H., Shin, K. H., and Kim, K.-B. (2006). Electron-beam lithography of Co/Pd multilayer with hydrogen silsesquioxane and amorphous Si intermediate layer. *J. Vac. Sci. Technol.*, 24(6), 2616–2620.
- Xie, Z., Yu, W., Wang, T., Zhang, H., Fu, Y., Liu, H., Li, F., Lu, Z., and Sun, Q. (2011). Plasmonic Nanolithography: A Review. *Plasmonics*, 6(3), 565–580.
- Yatsui, T., Kouroggi, M., and Ohtsu, M. (1998). Increasing throughput of a near-field optical fiber probe over 1000 times by the use of a triple-tapered structure. *Applied Physics Letters*, 73(15), 2090.
- Zhang, J. and Zhang, L. (2012). Nanostructures for surface plasmons. *Adv. Opt. Photon.*, 4(2), 157-321.
- Zhou, N., Kinzel, E. C., and Xu, X. (2011). Nanoscale ridge aperture as near-field transducer for heat-assisted magnetic recording. *Applied Optics*, 50(31), G42–G46.
- Zhou, N., Li, Y., Traverso, L., and Xu, X. (2016). Optical and Thermal Behaviors of Plasmonic Bowtie Aperture and Its NSOM Characterization for Heat-Assisted Magnetic Recording. *IEEE Trans. Magn.*, 52(2), 1100105.
- Zhou, N., Li, Y., and Xu, X. (2014). Resolving near-field from high order signals of scattering near-field scanning optical microscopy. *Opt. Express*, 22(15), 18715–18723.
- Zhou, N., Traverso, L. M., and Xu, X. (2015). Power delivery and self-heating in nanoscale near field transducer for heat-assisted magnetic recording. *Nanotechnology*, 26, 134001.
- Zhou, N., Xu, X., Hammack, A. T., Stipe, B. C., Gao, K., Scholz, W., and Gage, E. C. (2014). Plasmonic near-field transducer for heat-assisted magnetic recording. *Nanophotonics*, 3(3), 141–155.

VITA

VITA

Luis Miguel Traverso was born in Mayagüez, Puerto Rico, in 1983. He received his B. S. degree in Mechanical Engineering at the University of Puerto Rico in Mayagüez in May of 2007. After his B. S. graduation, he joined a small branch of the company Florida Turbine Technologies in Cabo Rojo, Puerto Rico, as a Structural Analyst. In August of 2009 he joined the research group of Professor Xianfan Xu as a direct Ph.D. student at Purdue University in West Lafayette, Indiana. While at Purdue, he did most of his work at the Birck Nanotechnology Center. His area of research is related to the fabrication of components to focus light in nano-scale sizes for heating and lithography processing. He is expecting to receive his Ph.D. degree in December 2016.